# Seismic and ultrasonic surface wave differential imaging for monitoring anthropogenic structures and the surrounding subsurface

Ao Wang

DOCTORAT ECOLOGIE
BRETAGNE GEOSCIENCES
LOIRE AGRONOMIE ALIMENTATION

UNIVERSITÉ DE NANTES

# THESE DE DOCTORAT DE

L'UNIVERSITE DE NANTES

ECOLE DOCTORALE N° 600
*Ecole doctorale Ecologie, Géosciences, Agronomie et Alimentation*
Spécialité : Sciences de la Terre et de l'environnement

Par
**Ao Wang**

# Imagerie différentielle en ondes de surface sismiques et ultrasonores pour le monitoring de structures anthropiques et du proche sous-sol environnant

**Thèse présentée et soutenue à Bouguenais, le 26/11/2020**
**Unité de recherche : Laboratoire GeoEND, Département GERS,**
**Université Gustave Eiffel, Campus Nantes**

**Rapporteurs avant soutenance** :

Ayse Kaslilar Senior Lecturer, Uppsala University, Sweden
Hervé Chauris Professeur, Mines ParisTech – Université PSL, France

**Composition du Jury :**

| | | |
|---|---|---|
| Président : | Eric Beucler | Professeur, Université de Nantes, France |
| Examinateurs : | Ludovic Bodet | Maître de Conférences - HDR, Sorbonne Université, France |
| Dir. de thèse : | Donatienne Leparoux | Directrice de Recherche, Université Gustave Eiffel, France |
| Co-dir. de thèse : | Odile Abraham | Ingénieure Divisionnaires des Travaux Publics de l'Etat, HDR, Université Gustave Eiffel, France |

# Contents

# List of Figures

# List of Tables

# Chapter 1

# Introduction

## 1.1 Context

The first meters and tens of meters of the underground constitute the interface between the atmosphere and the deep geological environment. Moreover this zone includes many human activities, whether for agriculture or because it is the seat of the foundations of anthropogenic constructions. Yet the subsurface is subject to meteorological modifications through the brutal climatic events that are becoming more and more numerous in the context of climate change.

The alternation of droughts and drastic rain fall extents makes rapid modifications of the water table level as well as the water content profile in the not saturated zone. The last, also called Vadose Zone or Critical Zone is thus very sensitive to climate change. It is a transfer zone between the atmosphere and the water table that lets pass soluble particles to the deepest media, thus a critical area to monitor.

Moreover, the rapid changes of water content in the shallower media can cause inner erosion or progressive variation of the media properties. This implies a key issue for the field stability, for the civil engineering structures sustainability, and for people's safety, i.e. a key issue for risk assessment. Thus the mechanical variations should be detected and monitored before they accumulate and create irreparable damages.

***Seismic methods.*** In order to overcome this need, geophysics approaches and more particularly seismic methods can be a priori relevant because surface recordings are linked to mechanical properties of underground without using destructive probes. Different usual seismic methods are based on different parts of the signal (reflected or refracted body waves, surface waves, etc.). For example, Wallace (1970); Haeni (1986) used compressional-wave to determine the water table in the aquifer, through the tomography of first-arrival travel time. More recent techniques like Full Waveform Inversion (FWI) tackle the entire recorded signal, i.e. uses the information contained in both amplitude and phase. By an inversion process, it is possible to recover seismic parameters of the medium, such as densities, P-wave and S-wave velocities (Tarantola, 1984; Virieux and Operto, 2009). But FWI is quite time-consuming and expensive to implement, and uses local inversion approaches which needs an accurate information for the initial model.

In near-surface applications, surface waves are widely used for its high energy and long propagation distance (Socco and Strobbia, 2004; Foti et al., 2014). The dispersion relation of surface waves are used to extract the medium's parameters as function of depth, especially the S-wave profile. Compared to FWI, the surface wave inversion (SWI) is less time-consuming (because the forward problem is it-self less time-consuming), and both local and global inversion algorithms are possible.

Surface wave methods can be considered as active methods by using controlled sources like sledge hammer and a series of receivers in line, or as passive methods by using continuous seismic signal that occurs in the surrounding media (ambient noise). In the later case, the sources and the receivers are usually arranged on a 2D surface instead of a line.

## 1.2 Time-lapse monitoring

Time-lapse monitoring aims to monitor the temporal variations of the media, through a series of measurements at different times. The concept "time-lapse" has been largely applied in the reservoir management and the long term monitoring of underground environment in the oil and gaz industry. For example, Arts et al. (2002, 2003) estimated the mass of the injected $CO_2$ in an underground reservoir, by comparing the data measured after $CO_2$ injection in 1994, 1999 and 2001. Riahi et al. (2013) performed a time-lapse analysis above an underground gas storage facility, using the phase velocity and the back azimuth (the angle of the wave front arriving at the array) of Rayleigh and Love waves, which were processed using a three-component beamforming algorithm. Cotton et al. (2018) developed a 4D modified prestack time migration method to detect the velocity changes, obtained from daily acquisitions. This method is applied on synthetic data and real onshore data sets, in order to monitor the heavy oil reservoir in the context of steam injection.

Recently, in near-surface applications, the time-lapse monitoring has also gained the reasearchers' attention. Planès et al. (2016) applied passive seismic interferometry technique to monitor the temporal changes, e.g. the internal erosion, in earthen dams and levees. 20% reduction of the surface wave velocity has been estimated in a laboratory scale experiment and 30% reduction of surface wave velocity has been observed on a field embankment. The same technique has been applied to monitor the tidal response of a sea levee by Planès et al. (2017). Surface wave has been recorded at four different frequencies (related to four depths) in order to estimate the relative variations of its group velocity along a $180\,m$ section. The group velocity variation estimated, which is equal to 5%, might be related to a concentrated water seepage or an internal erosion. Joubert et al. (2018) monitor a sea dike (the dike body and its substratum) during a tidal cycle using a passive surface wave methods. The empirical Green's functions, which are obtained by cross-correlation or deconvolution were used to extract the phase delay and the spectral amplitude ratio, which gave information on the temporal variations of the surface wave velocity and attenuation. The authors pointed out that the variations could be due to the water infiltration in the body of the dike.

### 1.2.1 Main issues in time-lapse monitoring

Since time-lapse monitoring aims to estimate temporal variations in the media, the differences of seismic data measured at different times should be caused only by the changes of the properties of the medium. In order to get close to this ideal case, several aspects are critical in the methodological process. We can cite the source repeatability, the receivers coupling, the measurement uncertainty. The challenge concerning these critical points are summarized bellow:

***Sources issue.*** Passive methodology can provide continuous recordings at no cost, compared to active sources. But passive sources, such as ambient noise, cannot be controlled. The unpredictable variations in such sources can lead to variations in data, thus bias the assessment of the medium. On the contrary, active sources are easier to control. But measurements are more heavy to carry out and thus the time sampling is usually sparser. Long time intervals between two measurements makes it impossible to detect a sudden temporal variations. Different strategies are applied to overcome the source repeatability. In case of FWI methods, the source signature is systematically inverted. For surface waves methods, the active source signature is not mandatory when extracting phase or group velocities from relative recordings between several receivers. In the study of Ikeda et al. (2017), a controlled active continuous source is used to overcome this issue.

***Receivers issue.*** Multiple receivers are needed in most of seismic methods. In order to minimize the effects of their possible variations in positions, coupling and tilt between two measurement sets (O'Neill, 2004), acquisition equipment can be buried permanently during the construction of the structures (see Ikeda et al. (2017) for an example monitoring of the subsurface media above a $CO_2$ storage site with surface wave phase velocity). The sustainability of receivers should be taken care before the burial. When permanent receivers are not accessible, they can be replaced by temporary receivers while the positions of the receivers are marked permanently to be correctly spotted from one time to another (Pasquet et al., 2015b; Bergamo et al., 2016).

***Measurement uncertainty.*** The uncertainty due to measurement errors should be treated carefully in the measurement data, as it impacts the estimation of the variations in the medium. Generally, surface wave measurements are under the Gaussian assumption (Tarantola, 2005; Menke, 2018), i.e. the probability density of the measurement error is a Gaussian distribution. O'Neill (2004) pointed out that at low frequencies a Lorentzian distribution is more appropiate than a Gaussian distribution and proposed to use a realistic dispersion error for the data uncertainty. In more recent studies dedicated to monitoring needs, Dangeard et al. (2018) proposes a processing workflow to estimate the picking errors during the manual picking of P-wave first-arrival time and the surface wave phase velocity dispersion curve extraction.

***Inversion and parameter sensitivity.*** So far, in most of studies involving surface waves monitoring, the variations are estimated qualitatively on the information extracted from the measured data, such as the surface wave velocity and attenuation, the time delay, etc. If the quantitative estimation on the model parameter variations is needed, for example, temporal variations of the S-wave or P-wave velocities, or the model parameter variations in depth, an inversion process is essential. Moreover, the inversion input data should be chosen after a sensitivity study of the inversion input data with respect to the

model parameter that we are of interest. For example, classical inversion input data in surface wave inversions are the phase or group velocities, which are most sensitive to S-wave variations in the medium. Actually, if the parameter sensitivity is too low compared to their temporal variations, the monitoring process cannot be efficient.

This last point is crucial and is the focus of this PhD thesis (we do not consider the previous critical points which should be tackled in other studies).

## 1.3 Time-lapse inversion

Time-lapse inversion aims to estimate the changes of the model parameters, by inverting the data measured at different times. The subtraction of the inverted model parameters gives the temporal variations of the medium. Combining the temporal variations of the model parameters with the environmental changes over the measurement time, one can draw the reasons for the changes in the subsurface or in civil engineering structures.

***Time-lapse surface wave inversion.*** Bergamo et al. (2016) estimate the climate effects followed with surface waves in a clay-filled railway embankment. The surface wave dispersion data are measured and then inverted to reconstruct the time-lapse model of S-wave velocity. A velocity variation of 10% has been estimated quantitatively for the Rayleigh wave and the inverted S-wave, which is related to the seasonal distribution of precipitation and the soil water content. Ikeda et al. (2017) invert the surface wave phase velocity to monitor the environmental influences on shallow body wave velocities above the Aquistore $CO_2$ storage site. Higher phase velocities are observed during winter because the S-wave velocity increases with higher degree of frozen saturated rock. Pasquet et al. (2015b) propose to analyze the $V_p/V_s$ ratio to characterize the subsurface medium, with the P-wave velocity model recovered by first-arrival travel time tomography and the S-wave velocity inverted from surface wave dispersion data (which shows a higher lateral resolution than the S-wave velocity extracted from S-wave first-arrival travel time tomography). This method is then used to track the water table level in the shallow aquifer with the $V_p/V_s$ ratio and the Poisson's ratio in an experimental basin in France (Pasquet et al., 2015a), and characterize the physical properties of quick clays in a three-layer (peat, quick clay and bedrock) experimental site in Norway (Pasquet et al., 2014).

***Double difference full waveform inversion.*** The time-lapse inversions described above involve two (or several) independent inversions of the measured data and compare the inversion results to estimate the medium's variations. Parallel to these studies using surface waves, a strategy to overcome the uncertainty issue is possible through a differential inversion. The principle of Double Difference for FWI (DDFWI) methods uses the inversion result of one measured data to "guide" the other inversion through the definition of the initial model. Watanabe et al. (2004) propose to use the substraction of the time-lapse crosswell seismic data in the waveform inversion to assess the reservoir changes during gas production. This method is then developed for the same purpose by Denli and Huang (2009) in the time domain. The principle can be summarized as follows: instead of applying two independent inversions on the measured baseline and repeatline and extract the model parameter variations from the

subtraction of the inversion results, the DDFWI (1) uses the inversion result of the measured baseline to assess a synthetic baseline by solving the direct problem; (2) adds the subtracting result between the measured baseline and repeatline to the synthetic baseline for building a synthetic repeatline; (3) inverts this synthetic repeatline using the inversion result of the measured baseline as the initial model; (4) subtracts the inversion results of the measured baseline and that of the repeatline to recover the model parameter variations. The main advantage of this method is that the coherent noise between the measured baseline and repeatline can be removed by the subtraction. Thus the differences in the two data-sets are only due to the model parameter variations.

The DDFWI has been widely used for the purpose of monitoring reservoir properties. Zhang and Huang (2013) improve the quantitative time-lapse seismic monitoring of elastic properties within reservoirs, by using the approximate location of a reservoir boundary as a priori information in the DDFWI. Yang et al. (2013) apply the DDFWI method on time-lapse data-sets collected by ocean-bottom-cable (OBC) seismic survey (MacLeod et al., 1999; Sears et al., 2010) in the Valhall field in the North Sea. Zhang et al. (2016) apply the DDFWI on seismic data-sets acquired with reflection acquisition geometries, using a series of synthetic time-lapse data-sets. The feasibility and the robustness of the DDFWI have been studies by other authors. Asnaashari et al. (2012) show that the DDFWI method has a robustness limit when the two measured data-sets have uncorrelated noise, since the time-lapse changes are blinded by the noise. Yang et al. (2015) investigate the feasibility of the DDFWI under the condition of various types of non-repeatability in synthetic data-sets (random noise, acquisition geometry mismatch, source wavelet discrepancy, etc.). Although these tests are limited to acoustic assumption and thus P-wave inversion which does not simulate realistic earth data, the results show that the DDFWI gives a reliable estimate of the reservoir changes.

Despite the advantage of the DDFWI, it is difficult to apply this method directly in the surface wave inversion, especially using global inversion techniques. The first reason is that, the inversion input data in DDFWI is the waveform, which contains the information of the amplitude and the phase of the propagating waves, whereas, the surface wave inversion uses commonly dispersion data (phase or group velocity curve). Another reason is that global inversion techniques do not need an initial model. Therefore using the inversion result of the measured baseline cannot be used as the initial model of the measured repeatline inversion.

Nevertheless, the main idea of the DDFWI can still be applied in the surface wave methods: in this thesis work, the data difference is used to obtain directly the model parameter variation. The question is: (1) what kind of difference of (2) which input data extracted from surface waves is relevant for the inversion?

## 1.4 Objective

In the scientific context of monitoring using surface wave methods, the sensitivity of the inverse problem for assessing weak variations of the medium remains an open key issue. In this work, we tackle this topic by studying the effects of several innovative strategies based on different and new ways to consider the input data as well as different propositions to assess the residual between

calculated and measured data in the inversion process.

For this purpose, three studies are carried out. The first one is based on the sensitivity study of the dispersion data and proposes to introduce a new input data to the inversion process: the derivative of the phase velocity versus the frequency. This study, based on sensitivity analysis, numerical tests and experimental laboratory tests, has been published in the Geophysical Journal International (GJI) (Wang et al., 2020b).

The second and third propositions in this thesis work are based on "differential inversion" for the surface wave methods, i.e. inverting the data difference instead of two measured data-sets. Two approaches are considered: (1) calculating the difference by using several procedures to find the most relevant for surface wave dispersion data; (2) linearizing the surface wave equation and making use of the sensitivity kernel to invert the model parameter difference from the simple difference of the surface wave dispersion curves. The work has been conducted on numerical data as well as measurements carried out in small scale experiments in the laboratory. All approaches will be presented in Chapters 2, 3, 4, 5 according to the following structure.

## 1.5 Outline of the thesis

The manuscript of the thesis is organized in five chapters. The first chapter is the introduction of the thesis, which gives the general context and the challenges of the monitoring of slight changes with surface waves.

Chapter 2 presents the state of the arts. First, surface waves are introduced theoretically, using the wave propagation theory. The properties of Rayleigh wave in homogeneous and vertically heterogeneous elastic media are described, as well as the semi-analytical methods to calculate the Rayleigh wave phase velocity. Then, the usual processing of the surface wave to extract the surface wave phase velocities from measured seismic data is introduced. Finally, the local and the global inversions methods are presented. The uncertainty issues are commented in this section with more details on the surface wave measurements and inversion. The experimental tool, the measurement bench called MUSC (Measurement at Ultrasonic SCale) used for carrying out measurements under controlled conditions is also presented.

In Chapter 3, we propose to consider the frequency derivative of Rayleigh wave phase velocity as a new input data in the inverse problem. We first show that this dispersion data is a combination of the phase and group velocities. Its behavior is analyzed qualitatively and compared with the Rayleigh wave phase and group velocities, using the theoretical dispersion curves of a series of two-layer media with small variations. Then the quantitative analysis of the phase velocity derivative and the phase and group velocities are performed by calculating sensitivity curves. Inversion tests are provided to quantify the feasibility of using the phase velocity derivative, thanks to theoretical dispersion curves and experimental data recorded in the laboratory using two-layer epoxy-resin models. As mentioned above, this part corresponds to a published paper in GJI (Wang et al., 2020b).

The Differential Time-lapse Surface Wave Inversion (DTLSWI) is then firstly proposed in Chapter 4. For this approach, data difference is used as input data in the surface wave inversion. Two data differences are tested: the phase velocity

difference and the phase velocity dispersion diagram distance. The former is the $L2$ norm distance between two measured phase velocity dispersion curves, and the latter is based on a statistical distance considering the area of interest of the dispersion diagram as a histogram of phase velocity distribution. These two DTLDWI are tested numerically, using the synthetic dispersion diagrams, and experimentally, using the ultrasonic measured data of the two-layer epoxy-resin models and the two-layer mortar-concrete slabs.

Another differential inversion is proposed in Chapter 5. A linear assumption is applied on Rayleigh wave phase velocity, which makes it possible to relate the model parameter variations with the phase velocity variations by using the sensitivity kernel of Rayleigh wave phase velocity. The limits of the linear approximation are discussed by inversion tests on a series of two-layer models, where the theoretical phase velocities are calculated for each model. This approach is also applied to laboratory measured data recorded on the two-layer epoxy-resin models.

Chapter 4 and 5 are written as two independent scientific papers for submission in few weeks. Other publications at national and international conferences are also available:

- Wang, A., Le Feuvre, M., Abraham, O., & Leparoux, D. (2018, April). Toward a time-lapse inversion of surface waves for the monitoring of soils and structures. In 14ème Congrès Français d'Acoustique, 2018. (Le Havre, France.)

- Wang, A., Le Feuvre, M., Leparoux, D., & Abraham, O. (2018, September). Impact of Small Shear Wave Velocity Variations on Surface Wave Phase Velocity Inversion. In 24th European Meeting of Environmental and Engineering Geophysics (Vol. 2018, No. 1, pp. 1-5). European Association of Geoscientists & Engineers. (Porto, Portugal)

- Wang, A., Le Feuvre, M., Abraham, O., & Leparoux, D. (2018, November). Effet des petites variations d'un milieu bicouche sur une nouvelle observable d'inversion. In 11ème colloque GEOFCAN (approche GEOphysique et structurale de l'organisation spatiale et du Fonctionnement des Couvertures pédologiques Anthropisées et Naturelles), 2018. (Antony, France)

- Wang, A., Abraham, O., Leparoux, D., & Le Feuvre, M. (2019, July). Ultrasonic surface wave in concrete: Sensitivity Analysis of Phase velocity Derivative. In 46th Review of Progress in Quantitative Nondestructive Evaluation, 2019. (Portland, USA)

- Wang, A., Leparoux, D., Abraham, O., & Le Feuvre, M. (2019, September). Evaluation of Dispersion Diagrams Distances Based on Usual Histogram Analysis for the Surface Wave Difference Inversion. In 1st Conference on Geophysics for Infrastructure Planning Monitoring and BIM (Vol. 2019, No. 1, pp. 1-5). European Association of Geoscientists & Engineers. (The Hague, Netherlands)

- Wang, A., Leparoux, D., Abraham, O., & Le Feuvre, M. (2020, December). Differential Inversion of Surface Wave Methods: Proposition of Diagram Distance as Inversion Data. In 26th European Meeting of Environ-

mental and Engineering Geophysics. European Association of Geoscientists & Engineers, 2020. (Amsterdam, Netherlands)

Author's contributions to these studies are:

- designing of laboratory models
- performing measurements in the MUSC laboratory with the technicians and engineers team
- analysis and data processing by developing processing tools in Seismic Unix and Python language
- writing the global inversion codes in Python language based on the original code of M. Le Feuvre

# Chapter 2

# State of the Art

This chapter describes the physical theory and characteristics of surface waves, the surface wave methods, inversion algorithms, and the reduced scale measurement approach providing experimental laboratory data involved in the following chapters.

First, the principle of surface waves is presented, starting with the wave propagation theory in homogeneous, elastic, infinite, isotropic and linear medium, followed by the Rayleigh wave propagation in homogeneous and layered media. Then the MASW (Multichannel Analysis of Surface Waves) $f - v$ method is introduced to explain how to extract surface wave phase velocities from measured seismic data. Surface wave inversion approaches are introduced in the next section and separated in two sections dealing respectively with local and global inversions. It is followed by the uncertainty issue for the surface wave measurements and inversion. Finally, the MUSC (Measurement at Ultrasonic SCale) laboratory is presented, where a laser interferometer is used for the measurement at reduced scale.

## 2.1 Introduction of Surface Waves

Mechanical waves propagating in consolidated medium can be generally gathered into two types: body waves and surface waves. Body waves contain P-wave and S-wave which are distinguished by the relation between the direction of propagation and the particle motion (polarization): they are respectively compressional and transversal waves. Surface waves (SW) are elastic waves generated in presence of a boundary and propagate parallel to it. Compared to body waves, SW transport high energy since they are less affected by the geometrical attenuation, which makes long-length device measurement possible. Surface waves are thus widely used in different domain according to the spatial scale involved: Non-Destructive Evaluation (NDE) to characterize material's defects (e.g. Qixian and Bungey (1996); Métais et al. (2016)); characterization of geo-material's properties for geophysical or geotechnical uses (e.g.Xia et al. (1999); Nazarian et al. (1983)); sesimological approaches to study the earth's crust and upper mantle (e.g.Mitchell (1995); Shapiro et al. (2005)). According to the boundary conditions, different kinds of SW are identified.

***Rayleigh Waves.*** Rayleigh waves occur in presence of a free surface. Among the three directions of particle motion, Rayleigh waves are generated by a vertical force in presence of a free surface (P-SV polarization in 2D media) and involve an elliptical motion in the vertical plane. In a homogeneous medium, Rayleigh waves propagate along the free surface and have a penetrating depth around or less than one wavelength. According to sensitivity studies (Aki and Richards, 2002; Takeuchi et al., 1972), Rayleigh wave velocity depends mainly on S-wave velocity $V_s$ and less on P-wave velocity $V_p$ and mass density $\rho$. Thus, Rayleigh waves can provide information as a profile of $V_s$, as a function of depth.

***Love Waves.*** This is an other kind of surface waves in the presence of a free surface. Love waves involve particle's transverse motion generated by a source polarized in the SH direction in 2D media. Love waves do not exist in homogeneous medium but occur in layered media, such as, a soft superficial layer on top of a stiffer half-space, since energy is trapped in the low-velocity layer. Love waves velocity depends only on how S-wave velocity ($V_s$) and mass density ($\rho$) vary with depth. Thus, this kind of surface waves usually arrives a little bit earlier than Rayleigh Waves.

***Scholte Waves.*** Scholte waves are the surface waves propagating at the boundary between a solid and a liquid layer. Under this boundary condition, two types of interface waves are propagated: Scholte waves and P-guided waves. The properties of Scholte waves are mainly depending on the S-wave velocity of the sub-bottom sediments and the P-guided waves depend mostly on the P-wave velocity of the solid and of the water layer (Foti et al., 2014). Thus this kind of SW is used for the underwater applications.

### 2.1.1 Wave Propagation in Homogeneous Elastic Medium

In a homogeneous, elastic, infinite, isotropic and linear medium, the dynamic equilibrium principle without body forces on a volume element $dv$ can be written

$$div(\boldsymbol{\sigma}) = \rho\ddot{\mathbf{u}} \tag{2.1}$$

with $\boldsymbol{\sigma}$ the Cauchy stress tensor, $div(\cdot)$ the divergence differential operator, $\rho$ the mass density and $\mathbf{u}$ the displacement vector. $\ddot{\mathbf{u}}$ is the second order temporal

derivative of the displacement vector: $\ddot{\mathbf{u}} = \frac{\partial^2 \mathbf{u}}{\partial t^2}$

Under the assumption of small-strain, the **Hooke's law** for isotropic materials can be applied

$$\boldsymbol{\sigma} = \Lambda tr(\boldsymbol{\epsilon})\mathbf{I} + 2\mu\boldsymbol{\epsilon} \tag{2.2}$$

where $\Lambda$ and $\mu$ are Lamé's elastic constants, $tr(\cdot)$ is the *trace* matrix operator, $\mathbf{I}$ is the identity tensor and $\boldsymbol{\epsilon}$ is the strain tensor which is defined as

$$\boldsymbol{\epsilon} = \frac{1}{2}(\overrightarrow{grad}\,\mathbf{u} + (\overrightarrow{grad}\,\mathbf{u})^T), \tag{2.3}$$

with $\overrightarrow{grad}(\cdot)$ the gradient differential operator and $(\cdot)^T$ the transpose matrix operator.

Substituting the strain tensor in **Eq. 2.2** by its definition in **Eq. 2.3** gives the stress tensor

$$\boldsymbol{\sigma} = \Lambda div(\mathbf{u})\mathbf{I} + \mu(\overrightarrow{grad}\,\mathbf{u} + (\overrightarrow{grad}\,\mathbf{u})^T). \tag{2.4}$$

Substitution of **Eq. 2.4** into **Eq. 2.1** finally gives the Navier's displacement equation of motion

$$(\Lambda + \mu)\overrightarrow{grad}\,div(\mathbf{u}) + \mu\Delta\mathbf{u} = \rho\ddot{\mathbf{u}} \tag{2.5}$$

with $\Delta(\cdot)$ the Laplacien operator in Cartesian coordinates.

Applying divergence and curl operators to **Eq. 2.5** gives

$$(\Lambda + 2\mu)\Delta(div\,\mathbf{u}) = \rho\frac{\partial^2}{\partial t^2}(div\,\mathbf{u}), \tag{2.6}$$

$$\mu\Delta(curl\,\mathbf{u}) = \rho\frac{\partial^2}{\partial t^2}(curl\,\mathbf{u}), \tag{2.7}$$

with the operators' relations: $\Delta(\mathbf{u}) = \overrightarrow{grad}\,div(\mathbf{u}) - curl(curl\,\mathbf{u})$, $curl(\overrightarrow{grad}\mathbf{u}) = \mathbf{0}$ and $div(curl\mathbf{u}) = 0$.

**Eq. 2.6** and **Eq. 2.7** show that in an isotropic medium, the volumetric deformation (associated with the divergence operator) is separable from the distortion deformation (associated with the curl operator). **Eq. 2.6** and **Eq. 2.7** can also be obtained by applying Helmoltz's theorem on **Eq. 2.5**, by uncoupling the displacement vector on the irrotational movement and the movement without volume change.

Since **Eq. 2.6** and **Eq. 2.7** are applicable for every point in the isotropic medium, they can also be written as two wave equations:

$$(\Lambda + 2\mu)\Delta\mathbf{u} = \rho\ddot{\mathbf{u}}, \tag{2.8}$$

$$\mu\Delta\mathbf{u} = \rho\ddot{\mathbf{u}}. \tag{2.9}$$

The propagation velocities are

$$V_p = \sqrt{\frac{\Lambda + 2\mu}{\rho}}, \tag{2.10}$$

$$V_s = \sqrt{\frac{\mu}{\rho}}. \tag{2.11}$$

P-waves are the fastest body wave, which correspond to the compressional (or dilatation) waves. The propagation direction of P-waves is parallel to the direction of polarization. S-waves correspond to shear (or distortional) waves and their propagation direction is orthogonal to the particle motion; there is no S-wave in fluid.

Poisson's ratio is a parameter which describes the material's expansion or contraction in the directions perpendicular to the direction of stretching force. Poisson's ratio can be expressed as function of P-wave and S-wave velocities ratio $\gamma = \frac{V_P}{V_s}$

$$\nu = \frac{1}{2} \cdot \frac{2 - \gamma^2}{1 - \gamma^2}. \tag{2.12}$$

As $\gamma = \frac{V_P}{V_s} \geq 1$, the Poisson's ratio $\nu < 0.5$.

### 2.1.2 Rayleigh Waves in Homogeneous Elastic Medium

In the previous part, we demonstrate that in a homogeneous, isotropic and infinite linear medium, wave equations can be separated into compressional and shear waves respectively. However, in presence of boundary conditions, another solution occurs: the superposition of P-waves and S-waves provide surface waves which propagates along the surface.

According to Helmoltz's decomposition theorem, the displacement vector can be described by a scalar potential $\Phi$ and a vector potential $\mathbf{\Psi}$

$$\mathbf{u} = \overrightarrow{grad}\Phi + curl\mathbf{\Psi}, \tag{2.13}$$

which can be expanded

$$\begin{cases} u_1 = \dfrac{\partial \Phi}{\partial x_1} + \dfrac{\partial \Psi_3}{\partial x_2} - \dfrac{\partial \Psi_2}{\partial x_3}, \\ u_2 = \dfrac{\partial \Phi}{\partial x_2} + \dfrac{\partial \Psi_1}{\partial x_3} - \dfrac{\partial \Psi_3}{\partial x_1}, \\ u_3 = \dfrac{\partial \Phi}{\partial x_3} + \dfrac{\partial \Psi_2}{\partial x_1} - \dfrac{\partial \Psi_1}{\partial x_2}, \end{cases} \tag{2.14}$$

with $curl(\Phi) = 0$ and $\overrightarrow{grad} \cdot \mathbf{\Psi} = 0$.

Supposing that the Rayleigh waves are propagating along the $x_1$ direction and that the displacement component on the $x_3$ direction is zero, **Eq. (2.14)** can be simplified as following:

$$\begin{cases} u_1 = \dfrac{\partial \Phi}{\partial x_1} + \dfrac{\partial \Psi}{\partial x_2}, \\ u_2 = \dfrac{\partial \Phi}{\partial x_2} - \dfrac{\partial \Psi}{\partial x_1}, \end{cases} \tag{2.15}$$

with the potential vector having only one component on $x_3$ and then can be written as $\mathbf{\Psi} = [0, 0, \Psi]$.

Substituting **Eq. (2.15)** in **Eq. (2.5)** gives two differential equations

$$\frac{\partial^2 \Phi}{\partial x_1^2} + \frac{\partial^2 \Phi}{\partial x_2^2} = \frac{1}{V_P^2} \frac{\partial^2 \Phi}{\partial t^2}, \tag{2.16}$$

$$\frac{\partial^2 \Psi}{\partial x_1^2} + \frac{\partial^2 \Psi}{\partial x_2^2} = \frac{1}{V_S^2} \frac{\partial^2 \Psi}{\partial t^2}. \tag{2.17}$$

Considering a plane wave propagating along a semi-infinite space $(x_1, x_2)$ with $x_2 \geq 0$, the two potential scalars can be written as:

$$\begin{cases} \Phi(x_1, x_2, t) = \phi(x_2) e^{jk(ct - x_1)}, \\ \Psi(x_1, x_2, t) = \psi(x_2) e^{jk(ct - x_1)}. \end{cases} \tag{2.18}$$

Substituting **Eq. (2.18)** into **Eq. (2.16)** and **Eq. (2.17)** yields

$$\frac{\partial^2 \phi}{\partial x_2^2} + (\frac{\omega^2}{V_P^2} - k^2)\phi = 0, \tag{2.19}$$

$$\frac{\partial^2 \psi}{\partial x_2^2} + (\frac{\omega^2}{V_S^2} - k^2)\psi = 0. \tag{2.20}$$

To solve the differential equations, two parameters $p$ and $q$ are introduced, which are defined as

$$p^2 = k^2 - \frac{\omega^2}{V_P^2}, \tag{2.21}$$

$$q^2 = k^2 - \frac{\omega^2}{V_S^2}. \tag{2.22}$$

The solutions for the differential equations are

$$\begin{cases} \phi(x_2) = A_1 e^{-px_2} + A_2 e^{+px_2}, \\ \psi(x_2) = B_1 e^{-qx_2} + B_2 e^{+qx_2}, \end{cases} \tag{2.23}$$

where $A_1$, $A_2$, $B_1$, $B_2$ are constants and depend on the boundary conditions.

In order to satisfy the semi-infinite medium condition, i.e. the surface waves have an exponential decaying modal shape as function of depth, $p$ and $q$ should be positive. Moreover, to respect the law of conservation of energy, $A_2$ and $B_2$ are equal to zero. The potential scalars are now

$$\begin{cases} \Phi(x_1, x_2, t) = A_1 e^{-px_2} e^{jk(ct - x_1)}, \\ \Psi(x_1, x_2, t) = B_1 e^{-qx_2} e^{jk(ct - x_1)}. \end{cases} \tag{2.24}$$

The Hooke's law in **Eq. 2.4** gives

$$\begin{cases} \sigma_{12} = \mu(\dfrac{\partial u_1}{\partial x_2} + \dfrac{\partial u_2}{\partial x_1}), \\ \sigma_{22} = (\Lambda + 2\mu)\dfrac{\partial u_2}{\partial x_2} + \Lambda \dfrac{\partial u_1}{\partial x_1}, \end{cases} \tag{2.25}$$

and the substitution of **Eq. 2.15** and **Eq. 2.24** in **Eq. 2.25** yields

$$\begin{cases} \sigma_{12} = \mu(2\dfrac{\partial^2\Phi}{\partial x_1 \partial x_2} - \dfrac{\partial^2\Psi}{\partial x_1^2} + \dfrac{\partial^2\Psi}{\partial x_2^2}), \\ \sigma_{22} = (\Lambda + 2\mu)\dfrac{\partial^2\Phi}{\partial x_2^2} + \Lambda\dfrac{\partial^2\Phi}{\partial x_1^2} - 2\mu\dfrac{\partial^2\Psi}{\partial x_1 \partial x_2}. \end{cases} \tag{2.26}$$

The stress-free boundary condition at the ground surface of the half-space ($x_2 = 0$) may be expressed by the equations:

$$\begin{cases} \sigma_{12} = 0, \\ \sigma_{22} = 0. \end{cases} \tag{2.27}$$

Thus substituting **Eq. 2.24** in **Eq. 2.26** gives

$$\begin{cases} \dfrac{B_1}{A_1} = \dfrac{(\Lambda + 2\mu)p^2 - \Lambda k^2}{j2\mu qk}, \\ \dfrac{B_1}{A_1} = \dfrac{-j2kp}{k^2 + q^2}, \end{cases} \tag{2.28}$$

which means:

$$\left[(\Lambda + 2\mu)p^2 - \Lambda k^2\right](k^2 + q^2) - 4\mu pqk^2 = 0. \tag{2.29}$$

Square elevation of **Eq. 2.29** gives the Rayleigh dispersion equation:

$$\left(\frac{V_R}{V_S}\right)^6 - 8\left(\frac{V_R}{V_S}\right)^4 + 8\left(\frac{V_R}{V_S}\right)^2 \cdot \left[1 + 2\left(1 - \frac{V_S^2}{V_P^2}\right)\right] - 16\left(1 - \frac{V_S^2}{V_P^2}\right) = 0, \tag{2.30}$$

with the definition of Rayleigh wave velocity $V_R = \frac{\omega}{k}$, presenting the velocity of propagation of a wave moving along the free surface of an half-space. From the Rayleigh dispersion equation, one can see that $V_R$ depends on $V_P$ and $V_S$, which are medium's frequency-independent parameters. Thus, in a homogeneous, elastic, isotropic and linear half-space, the Rayleigh wave is non-dispersive, i.e., its propagation velocity is independent of frequency.

***Rayleigh wave velocity.*** In 1967, Viktorov made an approximation of the solution of Rayleigh dispersion equation, which is

$$K = \frac{V_R}{V_S} = \frac{0.87 + 1.12\nu}{1 + \nu}. \tag{2.31}$$

Since the Poisson's ratio $0 < \nu < 0.5$, the ratio between Rayleigh and shear velocities is given by

$$0.87 < K < 0.96. \tag{2.32}$$

Using the body wave velocities in **Eq. 2.10** and **Eq. 2.11**, the shear and compressional wave ratio can be written as

$$\gamma = \frac{V_s}{V_p} = \sqrt{\frac{1 - 2\mu}{2(1 - \mu)}}. \tag{2.33}$$

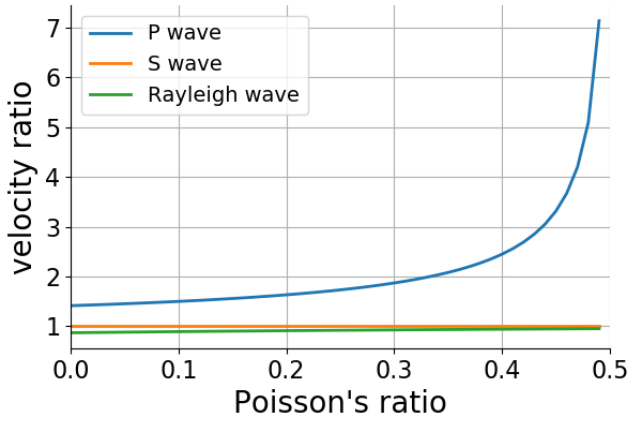


Figure 2.1: Relation between Poisson's ratio and velocity of propagation in a homogeneous, elastic, isotropic and linear medium.

The shear and compressional wave ratio $\gamma$ depends on the Poisson's ratio and its range is $\gamma \in (0, \frac{1}{\sqrt{2}})$. **Fig. 2.1** shows that in an linear elastic homogeneous medium, the difference between shear and Rayleigh waves velocities is very weak.

***Particle movement.*** Substituting $\Phi$ and $\Psi$ (**Eq. 2.24**) in **Eq. 2.14**, the displacements in $x_1$ and $x_2$ directions can be written as

$$\begin{cases} u_1 = \left(-jkA_1 e^{-px_2} - qB_1 e^{-qx_2}\right) e^{jk(ct-x_1)} \\ u_2 = \left(-pA_1 e^{-px_2} + jkB_1 e^{-qx_2}\right) e^{jk(ct-x_1)} \end{cases}. \tag{2.34}$$

The relations between $A_1$ and $B_1$ are deduced in **Eq. 2.28**. The amplitude of the displacements can be formulated as

$$\begin{cases} U_1 = jkA_1 \quad \left[-e^{-px_2} + 2\frac{\frac{p}{k}\frac{q}{k}}{1+(\frac{q}{k})^2} e^{-qx_2}\right] \\ U_2 = kA_1 \quad \left[-\frac{p}{k} e^{-px_2} + 2\frac{\frac{p}{k}}{1+(\frac{q}{k})^2} e^{-qx_2}\right] \end{cases}, \tag{2.35}$$

with $\frac{p}{k} = \sqrt{1-(\frac{V_R}{V_P})^2}$ (**Eq. 2.21**) and $\frac{q}{k} = \sqrt{1-(\frac{V_R}{V_S})^2}$ (**Eq. 2.22**).

According to the formulations of displacement above, one can calculate the Rayleigh wave displacements, in horizontal and vertical directions respectively. We notice that $U_1$ is an imaginary number whereas $U_2$ is a real number. These characteristics indicate that, the horizontal and vertical motions are out of phase of 90°. Thus in a homogeneous, elastic, isotropic and linear half-space, the particle movement of Rayleigh waves is retrograde elliptical.

**Fig. 2.2** gives examples of particle displacements and motions at three depths for a Poisson's ratio of 0.28. All the medium's parameters are given in **Table 2.1**. When $f = 50\,Hz$, the wavelength $\lambda$ is equal to $20\,m$. The horizontal and vertical displacements in **Fig. 2.2 (a)** are presented as functions of the depth normalized by the wavelength. The amplitudes of displacement are also normalized by the maximum of the vertical amplitude. When the depth is around $\lambda/5$, the horizontal displacement is vanishing (i.e. the Rayleigh wave

movement is purely vertical). This depth is called the *critical depth* where the particle movement changes from retrograde to prograde **Fig. 2.2 (b)**.

Table 2.1: Parameters in a homogeneous, elastic, isotropic and linear half-space. $V_P$: compressional-wave velocity; $V_S$: shear-wave velocity; $V_R$: Rayleigh wave velocity; $\rho$: density; $\nu$: Poisson's ratio.

| $V_P\,[m/s]$ | $V_S\,[m/s]$ | $V_R\,[m/s]$ | $\rho\,[kg/m^3]$ | $\nu$ |
|---|---|---|---|---|
| 2000 | 1100 | 1017 | 2200 | 0.28 |

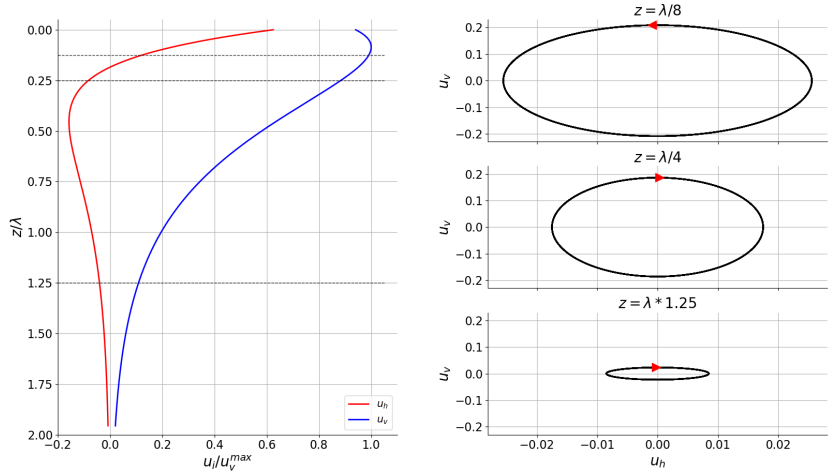


(a) (b)

Figure 2.2: (a) Horizontal ($u_h$) and vertical ($u_v$) displacements of Rayleigh wave as function of depth, normalized by wavelength $\lambda = 20\,m$ ($f = 50\,Hz$). The Poisson's ratio is equal to 0.28. (b) Particle motion at depths equal to $\lambda/8$, $\lambda/4$ and $\lambda \times \frac{5}{4}$ respectively. $u_h$ and $u_v$ correspond respectively to $u_1$ and $u_2$ in **Eq. 2.15**.

### 2.1.3 Rayleigh Waves in Vertically Heterogeneous Elastic Media

In a vertically heterogeneous media, i.e. a vertically layered media, Rayleigh wave features are dispersive, i.e. its propagating velocity depends on wavelength thus on frequency. To analyze the propagation problem in such a medium, one needs to solve an eigenvalue problem (Aki and Richards, 2002, Chapter 7). As an illustration of the method principle, we presents in this section the eigenvalue problem associated with Rayleigh waves, for the horizontal and vertical displacements.

Based on the study of the Rayleigh wave displacements in a linear elastic

homogeneous half space, the displacements can be assumed as

$$\begin{cases} u_1 = jr_1(x_2,k,\omega)e^{jk(ct-x_1)} \\ u_2 = r_2(x_2,k,\omega)e^{jk(ct-x_1)} \\ u_3 = 0 \end{cases} \tag{2.36}$$

where $u_2$ presents a prograde motion out of phase of 90° to $u_1$. Using Hooke's law (**Eq. 2.4**), the stress field can be calculated as

$$\begin{cases} \sigma_{11} = j[-(\Lambda+2\mu)kr_1 + \Lambda\dfrac{dr_2}{dx_2}]e^{jk(ct-x_1)} \\ \sigma_{22} = j[-\Lambda kr_1 + (\Lambda+2\mu)\dfrac{dr_2}{dx_2}]e^{jk(ct-x_1)} \\ \sigma_{33} = j\Lambda[-kr_1 + \dfrac{dr_2}{dx_2}]e^{jk(ct-x_1)} \\ \sigma_{12} = j\mu[\dfrac{dr_1}{dx_2} - kr_2]e^{jk(ct-x_1)} \\ \sigma_{13} = \sigma_{23} = 0 \end{cases} . \tag{2.37}$$

$\sigma_{13} = \sigma_{23} = 0$ because of the free surface condition. Since the stress component $\sigma_{12}$ and $\sigma_{22}$ are continuous in depth $x_2$, they can be written as

$$\begin{cases} \sigma_{12} = jr_3(x_2,k,\omega)e^{jk(ct-x_1)} \\ \sigma_{22} = r_4(x_2,k,\omega)e^{jk(ct-x_1)} \end{cases} . \tag{2.38}$$

Using the dynamic equilibrium principle (**Eq. 2.1**), the differential equations for the motion-stress vector $r_1$, $r_2$, $r_3$, $r_4$ are

$$\frac{d}{dx_2}\begin{pmatrix} r_1 \\ r_2 \\ r_3 \\ r_4 \end{pmatrix} = \begin{bmatrix} 0 & k & \frac{1}{\mu} & 0 \\ \frac{-k\Lambda}{\Lambda+2\mu} & 0 & 0 & \frac{1}{\Lambda+2\mu} \\ k^2\zeta - \omega^2\rho & 0 & 0 & \frac{k\Lambda}{\Lambda+2\mu} \\ 0 & -\omega^2\rho & -k & 0 \end{bmatrix} \begin{pmatrix} r_1 \\ r_2 \\ r_3 \\ r_4 \end{pmatrix}, \tag{2.39}$$

where $\zeta = 4\mu(\Lambda+\mu)/(\Lambda+2\mu)$. This relation can also be rewritten as

$$\frac{df(x_2)}{dx_2} = A(x_2)f(x_2). \tag{2.40}$$

This equation defines a differential eigenvalue problem with the linear operator $\frac{d}{dx_2}$, and the motion and stress vectors are $r_1, r_2$ and $r_3, r_4$ respectively. With the boundary conditions considering a upper free surface above a semi-infinite medium:

$$\begin{cases} r_3 = 0,\ r_4 = 0 & x_2 = 0 \\ r_1 \to 0,\ r_2 \to 0 & x_2 \to \inf \end{cases} , \tag{2.41}$$

the Rayleigh wave velocity is calculated by solving the eigenproblem in **Eq. 2.40**, i.e. at one frequency $\omega$, looking for the wavelengths $k_n$, $j \in [1,N]$ which satisfy the eigenproblem described above. The values of $k_n$ are the **eigenvalues** associated with the eigenproblem, and their corresponding motion-stress vectors $r_i^{(n)}$, $i \in [1,4]$ are the **eigenfunctions**.

Each $k_n$ corresponds to a mode of propagation of Rayleigh wave (we note Rayleigh wave in all the thesis for simplicity of terminology even if the strictly correct term is "Pseudo-Rayleigh wave" in case of a layered medium) in the given vertically heterogeneous medium. In a vertically heterogeneous medium, different modes of propagation exists because of constructive interference. When $n = 1$, the mode is called the fundamental mode. In a medium where the shear-wave and the compressional-wave velocities increase with depth, the fundamental mode is considered preponderant (Foti et al., 2014; Socco et al., 2010).

### Numerical Techniques to solve the Rayleigh Eigenproblem

As explained above, the objective of the Rayleigh eigenproblem is to find the roots of the dispersion equation, which are the wavenumbers corresponding to the modes of propagation of Rayleigh waves at different frequencies. In the case of a vertically inhomogeneous media, there are many methods to solve this linear problem of first order ordinal differential equations with variable coefficients, including the numerical integration (Takeuchi et al., 1972), the finite difference method (Boore, 1972), the boundary element method (Manolis and Beskos, 1988), the spectral element method (Faccioli et al., 1996), and the **Propagator Matrix Method**.

The **transfer matrix method**, also called **Thomson-Haskell method**, is originally developed by Thomson (1950) and improved by Haskell (1953). In fact, Gilbert and Backus (1966) developed the general formulation of the Propagator Matrix Method and the Thomson-Haskell method is a special case of the Propagator Matrix Method, with the assumption that the medium is stratified with homogeneous layers. The global dispersion equation can be constructed by a sequence of matrix multiplication, with the continuity conditions of stress and displacement at each interface. Each matrix is formed by the parameters of the corresponding layer. The eigenvalues computation of the dispersion equation gives the wavenumbers at each frequency. Then the eigenfunctions can be determined for each mode of propagation, as function of depth. Knopoff (1964) proposed an alternative matrix procedure, which proved to be more stable and precise for higher modes computation, and faster than the Thomson-Haskell technique (Schwab, 1970). Other researchers have also helped to improve through, for example, the delta matrix method (Pestel and Leckie, 1963; Dunkin, 1965), the reduced delta matrix method (Watson, 1970), the Schwab-Knopoff method (Schwab and Knopoff, 1970, 1972), and the Abo-Zena method (Abo-Zena, 1979).

In the early 1970s, some researchers attempted to apply the finite element method to solve wave propagation problems (Lysmer and Drake, 1972; Lysmer and Waas, 1972). Later, Kausel and Roësset (1981) proposed the **dynamic stiffness matrix method**, which is a finite-element formulation derived from the Thomson-Haskell method. In this method, the Thomson-Haskell transfer matrices are replaced by layer stiffness matrices, which can be used to solve the surface wave eigenproblems and the elastodynamic problems under static and dynamic loads (Kausel, 1981).

Another important algorithm to solve the eigenproblem has been developped with the method of **reflection and transmission matrix** (R/T method), proposed by Kennett and his colleagues (Kennett, 1974; Kennett and Kerry, 1979). In this method, the reflection and transmission matrices of each layer are con-

Table 2.2: Parameters of a two-layer reference model.

| layer $(i)$ | $V_{P_i}\,[m/s]$ | $V_{S_i}\,[m/s]$ | $\rho_i\,[kg/m^3]$ | $\nu_i$ | $h_i\,[m]$ |
|---|---|---|---|---|---|
| 1 | 1000 | 600 | 1500 | 0.22 | 8 |
| 2 | 2000 | 1100 | 2200 | 0.28 | $\infty$ |

structed by the reflection and transmission coefficients, defined by the relation between up-going and down-going wave amplitudes. Then the global reflection and transmission matrices are obtained by the combination of the reflection and transmission matrices of each layer, through a recursive algorithm. The R/T method gives a physical interpretation as it explicitly models the constructive interference that leads to the formation of the surface waves modes. The R/T method has been generalized by Kennett (1983); Luco and Apsel (1983). Further studies of Chen (1993) and Hisada (1994, 1995) on the generalized R/T method have made it possible to provide stable and accurate Rayleigh wave phase velocities for both low and high frequencies. Lai and Rix (1998) further developed the generalized R/T method for visco-elastic media.The fast generalized R/T method (Pei et al., 2008) has improved the speed of computation while keeping the stability and accuracy of the generalized R/T method.

In this thesis work, we compute the Rayleigh wave dispersion curve using the Geopsy software, which uses the Dunkin's formalism (Dunkin, 1965; Wathelet, 2004). For reasons of convenience and flexibility in the development of methodological tests, the Geopsy software has been implemented in Python in this PhD thesis work. **Fig. 2.3** presents the Rayleigh wave phase velocity in a layered medium (model parameters are available in **Table 2.2**): the first five modes are shown.

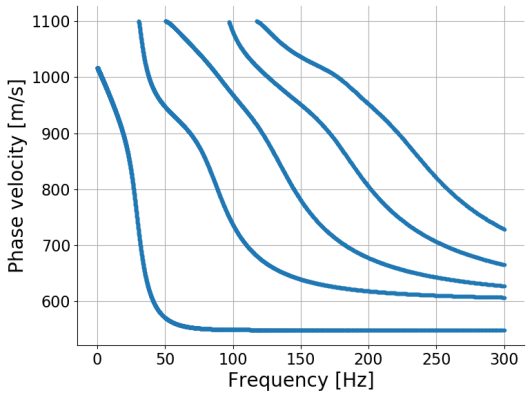


Figure 2.3: Rayleigh wave dispersion curve in a vertically heterogeneous medium (medium's parameters are available in **Table 2.2**).

### Sensitivity Kernel

The seismic properties of a 1D medium, noted the model parameters $\mathbf{m}$, are the S-wave and P-wave velocities ($V_s$ $V_p$), the density ($\rho$), as a function of depth $x_3$. The sensitivity kernel of the surface waves can provide quantitative information

about the effect of medium's variations on the dispersion data (e.g. the phase velocity), by calculating the partial derivative of the dispersion data with respect to the model parameters.

Aki and Richards (2002) (chapter 7) deduced the sensitivity kernel for Love waves, i.e. the Love wave phase velocity derivative with respect to the model parameters. Here we apply the same approach on the Rayleigh wave to establish the Rayleigh wave sensitivity kernel. In the first step, Hamilton's principle is applied to the Lagrangian density (i.e. the kinetic energy minus the elastic strain energy: see Aki and Richards (2002), chapter 2 for more details) of the Rayleigh wave to deduce the fractional change in phase velocity at a given frequency:

$$\left[\frac{\delta V_{ph}}{V_{ph}}\right]_{\omega} = \frac{1}{4V_g V_{ph} I k^2}\Big(\int_0^{\infty}(kr_1 + \frac{dr_2}{dx_3})^2\,\delta\Lambda dx_3 + \int_0^{\infty}(2k^2r_1^2 + 2(\frac{dr_2}{dx_3})^2 + (kr_2 - \frac{dr_1}{dx_3})^2)\,\delta\mu dx_3 - \int_0^{\infty}(\omega^2(r_1^2 + r_2^2))\,\delta\rho dx_3\Big). \tag{2.42}$$

$\delta$ represents the infinitesimal change of either the parameters ($\Lambda$, $\mu$, $\rho$) or the phase velocity. $I = \frac{1}{2}\int_0^{\infty}\rho(r_1^2 + r_2^2)dz$ is the energy integral. The partial derivative of Rayleigh wave phase velocity with respect to $\Lambda$, $\mu$, $\rho$ can be deduced using the method introduced in Aki and Richards (2002) (chapter 7):

$$\left[\frac{\partial V_{ph}}{\partial \Lambda}\right]_{\mu,\rho,\omega} = \frac{1}{4V_g I k^2}(kr_1 + \frac{dr_2}{dx_3})^2, \tag{2.43}$$

$$\left[\frac{\partial V_{ph}}{\partial \mu}\right]_{\Lambda,\rho,\omega} = \frac{1}{4V_g I k^2}\left[2k^2r_1^2 + 2(\frac{dr_2}{dx_3})^2 + (kr_2 - \frac{dr_1}{dx_3})^2\right], \tag{2.44}$$

$$\left[\frac{\partial V_{ph}}{\partial \rho}\right]_{\mu,\Lambda,\omega} = -\frac{1}{4V_g I k^2}(\omega^2(r_1^2 + r_2^2)). \tag{2.45}$$

Using **Eq. 2.10** and **Eq. 2.11**, the partial derivatives of $V_{ph}$ as a function of the medium's parameters ($V_s$, $V_p$ and $\rho$) can be formulated as follows:

$$\left[\frac{\partial V_{ph}}{\partial V_p}\right]_{V_s,\rho,\omega} = \frac{V_p\rho}{2V_g I k^2}(kr_1 + \frac{dr_2}{dx_3})^2, \tag{2.46}$$

$$\left[\frac{\partial V_{ph}}{\partial V_s}\right]_{V_p,\rho,\omega} = \frac{V_s\rho}{2V_g I k^2}[(kr_2 - \frac{dr_1}{dx_3})^2 - 4kr_1\frac{dr_2}{dx_3}], \tag{2.47}$$

$$\left[\frac{\partial V_{ph}}{\partial \rho}\right]_{V_p,V_s,\omega} = \frac{V_p}{2\rho}\left[\frac{\partial V_{ph}}{\partial V_p}\right]_{V_s,\rho,\omega} + \frac{V_s}{2\rho}\left[\frac{\partial V_{ph}}{\partial V_s}\right]_{V_p,\rho,\omega} - \frac{1}{4V_g I k^2}\omega^2(r_1^2 + r_2^2). \tag{2.48}$$

It should be pointed out that the sensitivity kernel of the group velocity has no analytical formulation (Aki and Richards, 2002).

This sensitivity kernel notion is a key tool for the studies presented in the following chapters because it makes possible to assess the a priori efficiency of an input data for recovering the medium parameters through an invert problem with enough sensitivity. It will be developed in the next chapter (Chapter 3)

for the innovative input data which will be proposed and will be detailed as a function of depth in the last chapter (Chapter 5) to answer the need for a specific analytical approach we propose.

## 2.2 Surface Wave Methods

In the previous sections, we have introduced the main properties of Rayleigh wave: in a homogeneous linear elastic half-space, the Rayleigh wave is non-dispersive, i.e. the propagation speed is independent on the frequency. However, in a vertically heterogeneous medium, the Rayleigh wave velocity depends on the frequency. Thus, one can extract information about the depth velocity profile of the medium by studying Rayleigh wave dispersion curves. To do this, multiple receivers are located at the medium upper surface along the propagation direction, for recording the particle motion (usually the vertical component) in view of deriving the dispersion relations.

Spectral Analysis of Surface Waves (SASW) is a method firstly proposed by researchers in 1980s (Nazarian et al., 1983; Stokoe et al., 1994), making use of two receivers aligned with an active harmonic source. Basically, the phase velocity can be derived as the ratio of the distance between receivers divided by the phase variation of the two recorded signals for each frequency component. However, using only two receivers limits the estimation of Rayleigh wave velocity when multiple modes occur because of the poor wavenumber resolution.

Then, researchers proposed a more robust method called MASW (Multi-channel Analysis of Surface Waves), making use of a linear array of receivers (McMechan and Yedlin, 1981; Gabriels et al., 1987; Park et al., 1998; Foti et al., 2000). The MASW method enhances the production rate in the field and makes the processing of the data faster, less subjective, and more robust compared to the SASW method. Several signal processing techniques can be used for extracting the dispersion curve of Rayleigh wave phase velocity, such as the $f-k$ transform (Foti et al., 2000; Gabriels et al., 1987), the $\tau-p$ transform (McMechan and Yedlin, 1981), the phase-difference method (Mokhtar et al., 1988; Park et al., 1998), or the linear Radon transform (Luo et al., 2008). Among them, the phase-difference method, achieved by processing an optimization of the $\tau - p$ transform, provides a high spectrum resolution with an optimized number of receivers (Park et al., 1998; Socco et al., 2010; Xia, 2014). In our study, we use the phase-difference method to extract the dispersion curve of Rayleigh wave phase velocity in frequency-velocity domain as explained below.

### 2.2.1 MASW $f - v$ method

With the help of a series of receivers, the particle motion can be recorded at each receiver position, giving a data set in time-offset domain $s(t, x)$, which is also called seismogram. Then, 1D Fourier Transform can be applied in time domain at one receiver position $x$, giving a 2D $f - x$ spectrum $S(f, x)$:

$$S(f,x) = \int_t s(t,x) e^{j2\pi ft} dt. \tag{2.49}$$

The source signal at position $x = 0$ can be written as $R(f) = A(f)e^{-j\phi(f)}$ with $A(f)$ and $\phi(f)$ the corresponding amplitude and phase.After a propagation

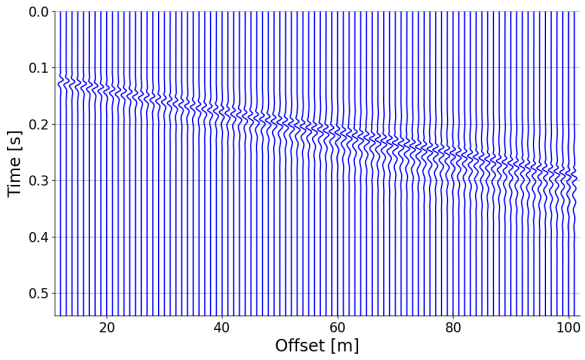


(a)

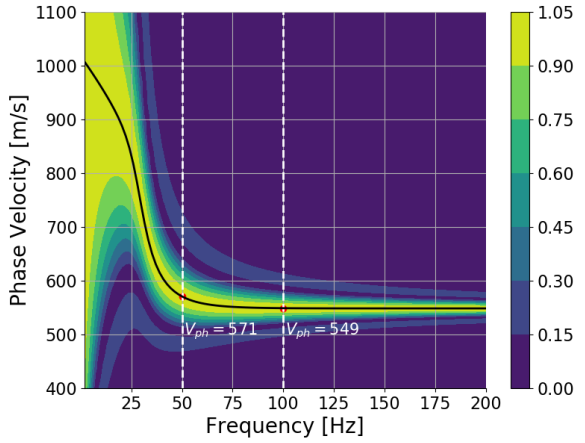


(b)

Figure 2.4: (a) Simulated seismogram in a two-layer medium. The active source is a Ricker wavelet with a central frequency equal to $50\,Hz$. 90 receivers are linearly arranged with a receivers' space of $1\,m$. (b) 2D Rayleigh wave dispersion spectrum in $f - v$ domain with a normalized amplitude at each frequency. The black line corresponds to the fundamental mode of Rayleigh wave phase velocity. The medium's parameters are provided in **Table 2.2**.

distance $x$, the recorded signal is

$$S(f,x) = A(f)e^{-j\phi(f)}e^{-j2\pi f\frac{x}{V_{ph}}} \tag{2.50}$$

with $V_{ph}$ the surface wave phase velocity at frequency $f$. The phase-difference method (Park et al., 1998) calculates the dispersion diagram as follows:

$$D(f,v) = \int_x \frac{S(x,f)}{|S(x,f)|}e^{j2\pi f\frac{x}{v}}dx. \tag{2.51}$$

**Eq. 2.51** can also be written for discrete offset $x_i$:

$$D(f,v) = \Delta x\sum_i^{N_x}\frac{S(x_i,f)}{|S(x_i,f)|}e^{j2\pi f\frac{x_i}{v}}, \tag{2.52}$$

with $\Delta x$ the receivers' space. **Fig. 2.4 (a)** shows a simulated Rayleigh wave seismogram, propagating in a medium, characterized by the model parameters given in **Table 2.2**. **Fig. 2.4 (b)** presents the dispersion diagram, calculated using **Eq. 2.52**. The amplitude of the dispersion diagram is normalized by the maximum value at each frequency. The phase velocity dispersion curve is assessed by selecting these maxima (black curve in **Fig. 2.4**).

## 2.3 Surface wave inversion

Given the parameters of a medium, one can describe its physical behavior, for example, the velocity of propagation, the particle movements, the dispersion relations, etc.. This procedure is called the **forward problem**. The **inverse problem** consists of using recorded measurement on a medium, to infer some of its parameters.

In the framework of surface wave inversion, a variety of observed data can be used: the surface wave group velocity (Pedersen et al., 2003; Saygin and Kennett, 2012; Yuan and Bodin, 2018), the Rayleigh or Love wave phase velocity (Socco et al., 2009; Safani et al., 2005), the coupled Rayleigh wave phase velocity and the attenuation (Lai and Rix, 1998; Bergamo et al., 2016), the ellipticity of Rayleigh wave (Maranò et al., 2012; Poggi et al., 2012; Hobiger et al., 2013), etc. Although the input data used in the inversion is different, the purpose is the same: by inverting the measured data, the model parameters are estimated by a numerical process and the state of the medium can be deduced.

In order to carry out this numerical process, there are numerous inversion algorithms. All of them are based on an iterative search mechanism and they are divided into two categories, respectively the local and global optimization techniques. Local inversions can be applied when the problem is considered locally linear around a model near the final solution (called the initial model). Global inversions do not require linearization nor an initial model: they search the model parameter with a (pseudo) random search method. Which ever inversion technique is used, a misfit (or objective) function is needed for quantifying the difference (discrepancies) between the measured data and the calculated data in the estimated model. In the following, these two inversion techniques will be briefly introduced. A Monte Carlo technique, the Neighborhood Algorithm, will be introduced with more details as it is used in this thesis work.

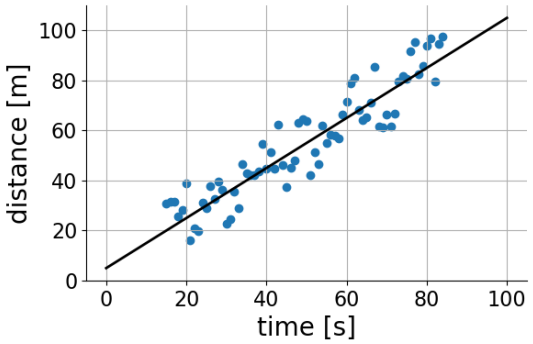


Figure 2.5: Example of the linear problem $x = at + b$. The blue dots are the observation data $(t_i, d_i)$. The black line is the estimated line.

### 2.3.1 Local inversion technique

In a given physical system, the model parameters $\mathbf{m}$ and the data $\mathbf{d}$ are related under physical law(s). If this relation is linear for $\mathbf{m}$ and $\mathbf{d}$, one can write

$$\mathbf{d} = \mathbf{G}\mathbf{m} \tag{2.53}$$

with the matrix $\mathbf{G}$ called the data kernel, $\mathbf{m}$ and $\mathbf{d}$ are two vectors.

**Example: Linear problem for a straight line x=at+b**

A simple example is the linear movement equation $x = at + b$ (**Fig 2.5**): $x$ is the position (of a car, for example) at time $t$, $a$ is the velocity and $b$ is the initial position. The inverse problem is to solve the equation, or in other words, find out the model parameter $\mathbf{m} = [a, b]^T$. For $N$ time observations, the linear equation can be written in the form of matrix $\mathbf{x} = \mathbf{G}\mathbf{m}$:

$$\begin{pmatrix} x_1 \\ x_2 \\ \dots \\ x_N \end{pmatrix} = \begin{bmatrix} t_1 & 1 \\ t_2 & 1 \\ \dots & \dots \\ t_N & 1 \end{bmatrix} \begin{pmatrix} a \\ b \end{pmatrix}. \tag{2.54}$$

In **Fig 2.5**, the blues dots present the observed distance $x_i$ at time $t_i$ and the black line presents the estimated line for equation $x = at + b$. Each measure point $t_i$ corresponds to an observed distance $x_i^{obs}$ and an estimated distance $x_i^{est}$. Defining the **misfit function** $E$ as

$$E = \sum_i^N (x_i^{obs} - x_i^{est})^2, \tag{2.55}$$

the best estimated line (black line in the **Fig 2.5**) gives the minimum value of $E$. Substituting $x_i^{est} = at_i + b$, **Eq 2.55** can also be written as

$$E = \sum_i^N (x_i^{obs} - at_i - b)^2. \tag{2.56}$$

The minimum of the **misfit function** $E$ can be found out by solving the equations

$$\frac{\partial E}{\partial a} = 2\sum_{i}^{N}(at_i - x_i^{obs} + b)t_i = 0, \tag{2.57}$$

$$\frac{\partial E}{\partial b} = 2bN + 2\sum_{i}^{N}(at_i - x_i^{obs}) = 0, \tag{2.58}$$

or in a matrix form using **Eq. 2.54**:

$$\mathbf{G}^T\mathbf{G}\mathbf{m} - \mathbf{G}^T\mathbf{x} = 0. \tag{2.59}$$

### General least-square solution

For a general linear problem, the misfit function $E$ is usually defined as the $L2$ norm distance (e.g. **Eq. 2.56**) which can be expressed

$$E = (\mathbf{d} - \mathbf{G}\mathbf{m})^T(\mathbf{d} - \mathbf{G}\mathbf{m}), \tag{2.60}$$

or

$$E = \sum_{i}^{N}\left[d_i - \sum_{j}^{M}G_{ij}m_j\right]\left[d_i - \sum_{k}^{M}G_{ik}m_k\right] \tag{2.61}$$

with $M$ and $N$ respectively representing the lengths of the vectors $\mathbf{m}$ and $\mathbf{d}$. Writing the element $m_q$ ($q \in [1, M]$) in the model parameter vector $\mathbf{m}$, to find the model parameter $\mathbf{m}$ which gives the minimum $E$, one should solve the equation

$$\frac{\partial E}{\partial m_q} = 0. \tag{2.62}$$

The partial derivative of the error $E$ with respect to $m_q$ can be written (Menke, 2018)

$$\frac{\partial E}{\partial m_q} = 2\sum_{j}^{M}m_j\sum_{i}^{N}G_{iq}G_{ij} - 2\sum_{i}^{N}G_{iq}d_i = 0 \tag{2.63}$$

and then expressed in matrix form:

$$\mathbf{G}^T\mathbf{G}\mathbf{m} - \mathbf{G}^T\mathbf{d} = 0. \tag{2.64}$$

The solution of **Eq. 2.64** can be written in the case where $[\mathbf{G}^T\mathbf{G}]^{-1}$ exists

$$\mathbf{m}^{est} = \mathbf{G}^{-g}\mathbf{d}, \tag{2.65}$$

with $\mathbf{G}^{-g} = [\mathbf{G}^T\mathbf{G}]^{-1}\mathbf{G}^T$.

The existence of $[\mathbf{G}^T\mathbf{G}]^{-1}$ has been discussed in Menke (2018). Briefly speaking, when the number of data is more than the number of unknowns, i.e. $N > M$, the problem is overdetermined. In this case, $[\mathbf{G}^T\mathbf{G}]^{-1}$ exists and the "best" solution can be calculated using **Eq. 2.65**. When $N < M$, there are more unknowns than data. The problem is underdetermined. In the case where $N = M$, the problem is even-determined. There is only one solution of $\mathbf{m}$ which fits perfectly the data, i.e. the error is zero. Others cases, such as the purely underdetermined problem and the mixed-determined problem, have also been discussed in Menke (2018).

**Local inversion in surface wave methods**

The local inversion techniques can be applied in geophysical problems when the problem is linearized around an initial model parameter $\mathbf{m_0}$. A good guess of the initial model is needed to make sure that the real model values of the medium is nearby this initial model. The calculated data $\mathbf{d}^{cal} = \mathbf{G}\mathbf{m_0}$ will be compared with the measured data $\mathbf{d}^{mes}$ with a defined misfit function (for example, a $L2$ norm distance). If the initial model parameter $\mathbf{m_0}$ equals to the real one, the misfit function should be zero. If not, another model parameter $\mathbf{m_i}$ ($i$ is the number of searched model in the inversion) should be used to recalculate $\mathbf{d}^{cal}$ which will be recompared with the measured data, until a best model parameter is found. The process is therefore iterative to converge to the minimum misfit value.

Most of the local inversion techniques are gradient-based. For example, when inverting Rayleigh wave phase velocity to estimate the model parameter of a medium, the Jacobian matrix $\mathbf{J_s}$, of which elements are the first-order partial derivatives of Rayleigh phase velocity with respect to the model parameter, is used to guide the model selection at each iteration (Xia et al., 1999; Calderón-Macías and Luke, 2007).

An advantage of the local inversion techniques is that the computational cost is relatively low, even with a large the number of unknowns because only few numbers of direct problems have to be calculated. Another attractive feature of the local inversion techniques is that the resolution and the model covariance can be calculated (Sambridge and Mosegaard, 2002). The resolution measures the degree of the model parameter's independence from each other, and the model covariance gives information about the propagation of the data uncertainty into the model parameter (Lai et al., 2005).

However, the local inversion techniques can be applied when the non-linearity of the problem is relatively weak, with a good guess of the initial model. When the non-linearity becomes important, the misfit function **Eq. 2.60** is quickly non-convex when the parameters move away from the global minimum, making it difficult to converge toward the global minimum and thus difficult to optimize the inversion process. Therefore, the initial model is an important issue in the local inversion for surface waves techniques as well as for other methods. Since the solution is considered to be near the initial model, a bad initial model could lead the inversion to a local minimum (of the misfit function), thus the final inversion result could be different to the true model (Socco et al., 2010).

### 2.3.2 Monte Carlo Inversion Technique

The moderate computation time associated to local inversion becomes less important as computers getting more and more powerful. This favors the Monte Carlo Inversion technique (MCI) to solve geophysical problems, which are usually non-linear with non-unique solutions. MCI searches the model parameters in the whole parameter space, with a random or pseudo-random search method, regardless of an initial model.

Since Keilis-Borok and Yanovskaja (1967) firstly introduced MCI in geophysical problem, it has been widely used and well developed. For example, the Simulated Annealing (SA) (Kirkpatrick et al., 1983; Geman and Geman, 1984; Aarts and Korst, 1988), the Genetic Algorithm (GA) (Stoffa and Sen,

1991; Sambridge and Drijkoningen, 1992; Gallagher and Sambridge, 1994), the Neighborhood Algorithm (NA) (Sambridge, 1999a,b; Wathelet, 2008), etc. A review has been made by Sambridge and Mosegaard (2002), in which the origins and the developments of the MCI have been described in detail.

Different inversion algorithms have their advantage and application domain. In this thesis work, the NA is chosen to solve the surface wave inverse problem. It is widely used in the near-surface applications, thanks to the easy use and fast calculation of the free software Geopsy (Dinver package for the inversion) developed by M. Wathelet and his colleagues. In the following, the NA will be introduced with more details.

### Neighborhood Algorithm

The Neighborhood Algorithm (NA) is firstly proposed by Sambridge in 1999 (Sambridge, 1999a,b) and then developed by Wathelet (Wathelet, 2008). The main idea of NA is to use the information of the current generated models to guide the new models' generation. Another innovative point is that NA uses Voronoi cells to assist in generating models. Indeed, given $N$ models $\mathbf{m_i}$ ($i \in [1, N]$), the Voronoi cell can separate the parameter space in a unique way: each cell is the nearest neighbor region of the center model $\mathbf{m_i}$. The mathematical definition of Voronoi cell with its center model $\mathbf{m_i}$ is:

$$V(\mathbf{m_i}) = \{\mathbf{m} | \|\mathbf{m} - \mathbf{m_i}\| \leq \|\mathbf{m} - \mathbf{m_j}\|\}, \text{for } j \neq i, \text{ and } i, j \in [1, N], \qquad (2.66)$$

with $\|\cdot\|$ the $L2$ norm distance between two model parameters.

In NA inversion, four tuning parameters are needed: $n_{s_0}$, $n_s$, $n_r$, $n_i$. Their functions are described in the following four steps:

1. Generating $n_{s_0}$ initial models in the parameter space by the Markov-Chain random walk (Hastings, 1970). The parameter space is separated into $n_{s_0}$ Voronoi cells.
2. Calculating the misfit function of the generated models in the previous step and chose the best $n_r$ models and their corresponding Voronoi cell.
3. Generating $n_s$ models in the previous selected $n_r$ Voronoi cells, following a uniform random walk (Wathelet, 2008). $n_s/n_r$ new models are generated for each cell.
4. Repeating step 2 and 3 for $n_i$ iteration.

According to the four steps above, the total number of generated models are $N = n_{s_0} + n_s \times n_i$. However, in the calculation, $n_s/n_r$ can be not an integer. In Wathelet (2008), $n_s/n_r$ is rounded down. In our Python program, a small modification has been made at step 3:

- Generating $n_s$ models in each of the previous selected $n_r$ Voronoi cells, following a uniform random walk (Wathelet, 2008). $n_s \times n_r$ new models are generated.

In this way, the total number of generated models will be $N = n_{s_0} + n_s \times n_r \times n_i$. In either case, the number of Voronoi cells grows exponentially in the region where the values of the misfit function are small.

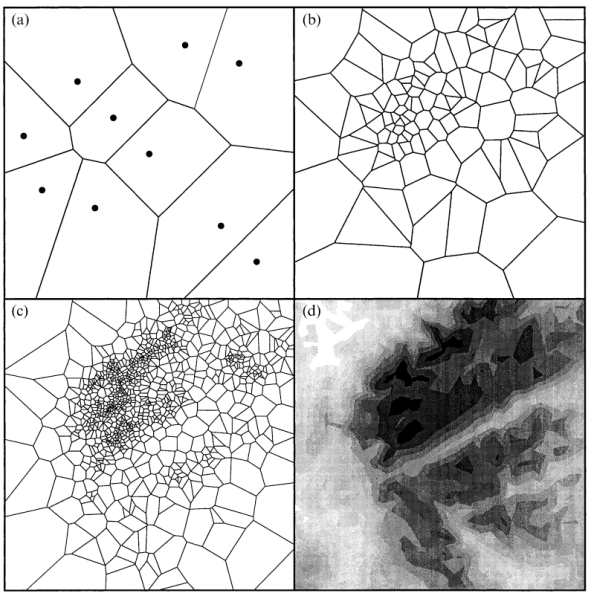


Figure 2.6: (a) to (c): Voronoi cells in a 2D parameter space with increasing number of cells (10, 100 and 1000) (Sambridge (1999a), Figure 1). (d) Contour of the misfit functions, with decreasing values from light to deep color. In the deepest color regions, the Voronoi cells are sampled thus more models are searched in these regions.

### 2.3.3 Uncertainty Estimation

The uncertainty in geophysical inverse problems consists of two main parts: the modelization uncertainty and the measurement uncertainty (Tarantola, 2005). Inversion problems can be ill-posed, i.e. the existence, the uniqueness and the stability of the inversion result may be not verified. In this case, the modelization uncertainty should be considered.

The measurement uncertainties are mainly coming from the noise in the recorded signals, the inaccuracy of receivers' placement and static shifts, and less affected by the receiver's tilt and coupling (O'Neill, 2004). Most of the surface wave measurements are considered under the Gaussian assumption (Tarantola, 2005; Menke, 2018), i.e. the probability density for the measurement error $\epsilon$ is a Gaussian distribution, with zero mean and variance $\sigma^2$:

$$f(\epsilon) = \frac{1}{(2\pi)^{\frac{1}{2}}\sigma} e^{-\frac{1}{2}\left(\frac{\epsilon}{\sigma}\right)^2}. \tag{2.67}$$

Or in matrix form with the error vector $\boldsymbol{\epsilon} = \mathbf{d} - \mathbf{d}^{obs}$:

$$f(\boldsymbol{\epsilon}) = \frac{1}{(2\pi)^{N/2}\sqrt{det(\mathbf{C_D})}} e^{-\frac{1}{2}(\mathbf{d}-\mathbf{d}_{obs})^T \mathbf{C_D}^{-1}(\mathbf{d}-\mathbf{d}_{obs})}. \tag{2.68}$$

$N$ is the length of $\mathbf{d}$ and $\boldsymbol{\epsilon}$. $\mathbf{C_D}$ the covariance matrix, representing the total uncertainty: $\mathbf{C_D} = \mathbf{C_T} + \mathbf{C_d}$, with the measurement uncertainty $\mathbf{C_d}$ and the modelization (theoretical) uncertainty $\mathbf{C_T}$.

However, it should be mentioned that O'Neill (2004) used a series of field tests to show that the Gaussian distribution is not valid at low frequencies. A Lorentzian distribution is more appropriate at low frequencies where the surface wave phase velocity has poor resolution. O'Neill proposes to use the realistic dispersion error for the data uncertainty, which is a function of the receiver length and the measured phase velocity.

Note that, it is a difficult task to study all uncertainty issues in surface wave problems. In the following, we will focus on how to treat the uncertainty from the measurements to the inversion results, in local and global inversions respectively.

### Uncertainty Estimation in Local Inversion

The linear relation between the estimated model parameter $\mathbf{m}$ and the data $\mathbf{d}$ can be written as (Menke, 2018)

$$\mathbf{m} = \mathbf{M}\mathbf{d} + \mathbf{v} \tag{2.69}$$

where $\mathbf{M}$ and $\mathbf{v}$ are some matrix and some vector. For example, $\mathbf{M} = [\mathbf{G}^T\mathbf{G}]^{-1}\mathbf{G}^T$ for the least-square solution (see Chapter 2.3.1); $\mathbf{v}$ is related to a priori information for underdetermined problems (Menke, 2018). Then it is possible to write the mean value and the covariance of the model parameter as (Menke, 2018)

$$\overline{\mathbf{m}} = \mathbf{M}\overline{\mathbf{d}} + \mathbf{v} \tag{2.70}$$

$$\mathbf{C_m} = \mathbf{M}\mathbf{C_D}\mathbf{M}^T. \tag{2.71}$$

**Eq. 2.71** shows that the uncertainty in the estimated model parameter can be calculated from the uncertainty in the data. In the surface wave measurements, where the Rayleigh wave phase velocity is measured and the model parameter is the shear-wave velocity $V_s$, if the inverse problem is solved by the linear inversion techniques, the uncertainty of $V_s$ can be estimated by the following formula (Tarantola, 2005)

$$\begin{aligned} Cov[V_S] \approx & \left[(\mathbf{J}_S^T(Cov[V_R])^{-1}\mathbf{J}_S)^{-1}\mathbf{J}_S^T(Cov[V_R])^{-1}\right] \cdot Cov[V_R] \\ & \cdot \left[(\mathbf{J}_S^T(Cov[V_R])^{-1}\mathbf{J}_S)^{-1}\mathbf{J}_S^T(Cov[V_R])^{-1}\right]^T. \end{aligned} \tag{2.72}$$

$Cov[V_R]$ is the covariance matrix of the measured Rayleigh wave phase velocity $V_R$, $\mathbf{J_s}$ is the Jacobian matrix of $V_R$, i.e. the partial derivative of $V_R$ with respect to the model parameter $V_s$.

**Eq. 2.72** has been used by Lai and Rix (1998) when $V_R$ is inverted by Occam's algorithm (Constable et al., 1987), a local inversion technique, and been further used to estimate the uncertainty in the inverted S-wave profile, obtained from two field measurements (Lai et al., 2005). The same equation has been used in Strobbia and Foti (2006) to estimate the uncertainty of the inversion results in the Multi-Offset Phase Analysis (MOPA). In this procedure, the phase-offset data is extracted after signal processing on the measured seismic data, and is used to calculate the wavelength $k$ using a regression procedure. The Rayleigh phase velocity is then obtained by $V_{ph} = \frac{2\pi f}{k}$ and be inverted using local inversion.

### Uncertainty Estimation in Global Inversion

The local inversion techniques give one inversion result of model parameters (e.g. the $V_s$ or $V_p$ profile as function of depth) and the model error can be estimated using the **Eq. 2.72**. Unlike the local inversion techniques, which are matrix-based methods, it is difficult to quantitatively estimate the data uncertainty propagation to the inverted model parameter, when global inversion techniques are applied. Besides, the global inversion gives a family of inverted models, instead of one single model. Each of them has a corresponding misfit value which represents the fitting level with respect to the measurements. The expected family of inverted models should have an acceptable misfit value in the frame of the uncertainty of the method. Thus, the estimation of the uncertainty in global inversion results would make it possible to select the acceptable models from all searched models. It is related to both the inversion algorithm and the inversion input parameter.

When NA inversion (Sambridge, 1999a,b; Wathelet, 2008) is applied in surface wave inversion, the data error is usually introduced in the misfit function as following (Wathelet, 2004):

$$misfit = \sqrt{\frac{1}{N_f}\sum_{i}^{N_f}\left(\frac{d_i^{mes} - d_i^{cal}}{\sigma_i}\right)^2}. \tag{2.73}$$

$N_f$ is the number of samples in the measured data (the number of frequencies or wavelength, for example), $\sigma$ is the uncertainty of the measured data, and $d_i^{mes}$, $d_i^{cal}$ are the measured and calculated data at point $i$. When $\sigma$ is not available, it can be replaced by $d^{mes}$.

Note that, as the iteration number increases, the NA inversion converges towards the zone(s) where the model parameters are close to the real one (see **Fig. 2.6**). After a certain number of iteration, the misfit functions of the inverted model parameters are all equal to a lowest reachable value, and it is difficult to estimate which one(s) is(are) the best model(s).

The most common method to select the best inverted models for surface wave inversion is to give a user-defined threshold: when the misfit function of the inverted model parameter is lower than the threshold, the model parameter is considered acceptable. Hobiger et al. (2013) use this method to select the inversion results on both theoretical test and measured data, during the inversion of the Rayleigh wave ellipticity. Renalier et al. (2010) apply seismic ambient noise cross-correlation technique to retrieve 3D $V_s$ profiles. The acceptable models are those having misfit values less than 1.2 times the minimum misfit value of all searched models. Some authors also verified that the dispersion curves of the selected inversion results should be within the error bars of the measured data (Snoke and Sambridge, 2002; Endrun et al., 2008; Leparoux et al., 2012; Pasquet et al., 2015b). In this case, the use of error bars, e.g. Gaussian distribution or realistic error (O'Neill, 2004), affects the model selection.

Another method to select the inversion results is to fix the number of resulting models. Saygin and Kennett (2012) used the local group dispersion information to produce a 3D wavespeed model: from the total 50000 searched models, the best 5000 models (with lowest misfit values) are considered acceptable models.

One sees that neither method estimates quantitatively the uncertainty of model parameters. A study of Dettmer et al. (2012) has also pointed out that in most of inversion works, the uncertainty of model parameter has been estimated using qualitative and relative approaches. In their study, in order to quantify the effect of the uncertainty in data-error statistics on the uncertainty of model parameters, the hierarchical autoregressive data-error model has been introduced to invert the microtremor array dispersion data. This hierarchical autoregressive data-error model is particularly suitable for trans-dimensional inversion problem, in which the length of model parameter $\mathbf{m}$ (the number of elements in the model parameter) is considered unknown (Sambridge et al., 2013).

In our thesis work, the inverted model parameter will be selected with a threshold in the misfit values to select the chosen resulting models, without the consideration of error bars related to the measurement. This approach is chosen because the NA algorithm will be applied for the inversion of numerical data and measured data obtained from reduced-scale models in the laboratory. The errors in the numerical data can be controlled and are not the main concern in the inversion. The measurement errors in the laboratory are small since a laser interferometer is used for the recording of the data with a precision level for positioning equal to $10\,\mu m$. Moreover, different inversion input parameters are proposed and tested in this thesis work. It is impossible to use one error bar to describe the measurement uncertainty for all types of data.

## 2.4 Reduced-scale modeling experiments

Numerical simulations are usually under multiple assumptions, such as the isotropic/elastic media, 1D/2D models, homogeneous medium, etc., whereas complex modeling schemes lead to expensive computational costs. Thus, field measurements, which are realistic by definition, would be relevant for validating imaging and inverse methods. However, in most of real contexts, the mechanical properties cannot be well known and the measurement uncertainties due to the source and receiver coupling can further complicate the estimation of the medium. Thus, reduced scale modeling in the laboratory is a useful intermediate step between the numerical modeling and the field measurements, especially for validating new numerical modeling methods. Laboratory experiments provide well controlled conditions to study the physical phenomena. In addition, the measurement parameters can be chosen and verified and the experimental artifacts can be identified.

The use of reduced-scale models in geophysics dates back to the 1930s. Rieber (1936) uses the ultrahigh-speed photographic technique to produce snapshots of acoustic waves in the air for the purpose of study the seismic waves (direct, reflected and refracted). Since then, different ultrasonic techniques have been developed and two popular of them are piezoelectric based and laser based techniques.

The piezoelectric technology is firstly introduced by Press et al. (1954) and Oliver et al. (1954) in the geophysics domain, using piezoelectric transducers as sources and receivers. Following by the development of numerical modeling and processing methods based on multiple sources and receivers measurement in 1960s, the piezoelectric techniques have been widely used and developed in

the next decades: Hilterman (1970) validates a 3D acoustic model of arbitrary shape; French (1974) expands the migration method of processing seismic reflection data for handling 3D problems; Bishop et al. (1985) apply seismic first-arrival travel time tomography on reduced-scale models in order to produce a velocity-depth model of the medium and similarly, Lo et al. (1988) analyze the performance of several tomography algorithms with different source-receiver configurations and the size and properties of the models; Pratt (1999) uses reduced-scale model to verify the seismic waveform inversion in the frequency domain.

However, some issues of piezoelectric techniques have also be pointed out (Buddensiek et al., 2009; Fukushima et al., 2009), such as the coupling problem between the transducer and the sample, the non-plat transfer function of the piezoelectric transducers, the size of the transducer with respect to the wavelengths, etc. More recently, the laser based techniques have gained more interests which overcome the main issues of piezoelectric techniques in particular for the signals recordings. Thus, a piezo-electric transducer can be used as an active source and a laser interferometer, based on the optical interaction of a laser beam, is able to measure the particle movement and record as seismic data. Some works are based on these techniques, for example, Kaslilar (2007) developed an inverse scattering method to image near-surface heterogeneities using scattered surface waves. This method is validated by ultrasonic laboratory data, measured on a small scale aluminum block with a hole filled with epoxy. Bretaudeau et al. (2013) apply a 2D FWI approach in the frequency domain on a three-layered epoxy-resin model, in order to analyze the feasibility of this method in a near-surface context. Pasquet et al. (2016) built a reduced scale tank filled with dry glass beads to simulate granular media. P-wave first-arriving time and the phase velocity of surface waves are extracted and inverted from the ultrasonic data in order to estimate the varying water levels. Filippi et al. (2019) used reduced-scale epoxy-resin models to simulate underground geological medium, in order to understand the seismic wave propagation phenomena in the presence of cavity.

In this framework, the ultrasonic measurement laboratory MUSC (Non-contact Untrasonic Measurements, or Mesure Ultrasonique Sans-Contact in French) was built to reproduce seismic data in small scale models in Gustave Eiffel University (formely ifstar). The MUSC bench was first built by Bretaudeau et al. (2011) and then upgraded by Valensi et al. (2015). Bretaudeau et al. (2011) describe the set-up in the MUSC laboratory, which contains an optical table with two moving arms, a TEMPO-FS200 laser interferometer, a piezo-electric transducer as a source and small-scaled models. The experimental data recorded in MUSC are compared to simulated numerical data using the finite-element methods. A good agreement between the experimental and numerical data validates the use of MUSC laboratory for the purpose of studying physical phenomena in small scale models. Valensi et al. (2015) validate the upgrade of the device, making the measurement of horizontal particle displacement possible. More recently, Pageot et al. (2017) verified the reproductivity of the data produced in MUSC laboratory, by comparing 2D numerical data (simulated by the Spectral Element Method) and 3D experimental data.

The MUSC laboratory is used as an experimental tool in this thesis work, in order to produce seismic data on several reduced-scale models, which will be used for the inversion tests in the following chapters. The MASW methods

are applied on these measured data in order to extract the dispersion diagrams and dispersion curves. Both numerical and experimental data are used in the inversion process (NA inversion algorithm) for testing and validating the new propositions in each chapter.

# Chapter 3

# Frequency derivative of Rayleigh wave phase velocity for fundamental mode dispersion inversion: parametric study and experimental application

The study in this chapter aims to study the sensitivity of the Rayleigh wave dispersion data. The approach proposes to used the frequency derivative of Rayleigh wave phase velocity as an innovate inversion input data. The sensitivity study of the phase velocity derivative as well as the classical dispersion data, phase and group velocities, are carried out for a simple two-layer model and compared for variations of the shallow layer and the deep layer shear-wave velocity. The phase velocity derivative is tested on both numerical data and experimental data, obtained from two reduced-scale models, made by epoxy-resin. For that, a combined strategy is proposed to increase the accuracy of results while maintaining robustness in dispersion extraction.

This chapter is structured as a scientific article since it corresponds to the version published in Geophysical Journal International (Wang et al., 2020b).

## 3.1 Introduction

The subsurface media are particularly affected by climate change and associated climatic events through variations in water table levels and fluid transfers in the unsaturated zone, known as the Critical Zone. These phenomena create alteration zones that can potentially lead to collapses. For these reasons, monitoring mechanical changes in the subsurface media in areas of human activity, particularly when they involve buildings, is becoming increasingly important. These needs are therefore among the key issues of current geophysical research.

Among non-destructive seismic approaches for assessing the mechanical properties of shallow underground media, the properties of surface waves are widely used due to the energy they transport and their long propagation distances (Socco and Strobbia, 2004; Foti et al., 2017). Using the dispersion of surface waves in a layered structure, the properties of the medium are inferred by solving an inverse problem. This method, as a standard procedure for surface wave analysis, contains three steps: 1) acquisition, 2) processing for extracting the dispersion data that will serve as the inversion input data, and 3) the inversion whose output parameters are shear-wave velocity, compressional-wave velocity and density, as function of depth. Classically the phase velocity dispersion is used for subsurface investigations, and the group velocity dispersion is used for seismology approaches. The common methods to extract these two dispersion data are recalled below.

A sensitivity study by Bhattacharya (2015) showed that group velocity is more efficient than phase velocity to explore the anisotropic nature of a medium. The multiple filter method (MFM) proposed by Dziewonski et al. (1969) is based on band-pass frequency filters to analyze earthquake signals. Using different band-pass filters, waves with frequencies around the center frequency are isolated. Thus, the delay between the source wavelet and the arrival of the signal, both filtered for the current frequency, is used for assessing the group velocity corresponding to the current frequency. The main difficulty in using the multiple filter technique is the possible interference between higher modes when the envelope of the filtered signals is not sharp enough to contain a very narrow frequency band (Gabriels et al., 1987). Based on MFM, the reassignment method (Kodera et al., 1976; Auger and Flandrin, 1995) calculates the center of gravity of a signal pulse, which helps improve the accuracy of the group velocity assessment. Pedersen et al. (2003) developed a good adaptation for both synthetic seismograms and field data relating to shallow earth structures. However, the reassignment can blur the distinction between waves that are located close together, thus generating complexity in the time-frequency domain. In addition, in the case of strong frequency dispersion, the phase velocity can be efficiently extracted for several modes if a large set of receivers is involved (Socco and Strobbia, 2004). Thus, as mentioned by these authors, this dispersion data, i.e. the phase velocity, is commonly used in subsurface investigation. The principal of its extraction is explained below.

Indeed, the classical measurement setup for subsurface geophysics applications involves a set of several receivers for a processing method called MASW (Multichannel Analysis of Surface Waves). This approach, first implemented by geophysicists in the 1980s for near-surface characterization (McMechan and Yedlin, 1981; Gabriels et al., 1987) and improved in the following decades (Park et al., 1998; Foti et al., 2000), is the most commonly used method in the case of geophysical Near Surface investigations. By applying an active source and a linear array of receivers, the MASW method enhances the production rate in the field and makes the processing of the data faster, less subjective, and more robust compared to classical one-source one-receiver systems (Foti et al., 2014). The processing stage consists in extracting from recordings the dispersion data that will be inverted. With the MASW approach, the dispersion data comprises the dispersion curves of the phase velocity. Several signal processing techniques can be used for extracting it, such as the $f-k$ transform (Yilmaz, 1987), the $\tau-p$ transform (McMechan and Yedlin, 1981), the phase-difference

method (Park et al., 1998; Mokhtar et al., 1988), or the linear Radon transform (Luo et al., 2008). The phase-difference method, achieved by processing an optimization of the $\tau - p$ transform, provides a high spectrum resolution of the dispersion diagram with an optimized number of receivers (Park et al., 1998; Socco et al., 2010; Xia, 2014). It has been chosen for this study. For this procedure, the Fourier Transform is applied to each signal of the seismic shot. After normalizing the amplitude, a phase shift correction is applied to each frequency component as a function of the receiver-source distance, through a series of possible phase velocities. The corrected frequency components are summed over the entire shot to obtain a dispersion diagram in the $v - f$ domain. On the latter, the areas of maximum values correspond to the extracted phase velocity estimated as a function of frequency for the fundamental mode and the excited higher modes.

Whatever the dispersion data used (i.e. group or phase velocity), the general approach of dispersion inversion of surface waves makes it possible to characterize the propagating media for investigating the Earth on a global scale up to the first meter deep or even the sub-millimeter scale, depending on the propagating wavelength range used. Thus, surface wave analysis should be suitable for monitoring the mechanical variations of the subsurface. For example, Planès et al. (2016) used the passive seismic-interferometry technique to analyze internal erosion in earth dams and levees. They were able to monitor a 20% reduction in surface wave velocity on a canal embankment model and a 30% variation in a field-scale levee testing experiment. The same technique has been used on a sea levee in the Netherlands, using traffic noise on a bridge and the noise from a wind turbine as sources, and a $3 - 5\%$ increment of the group velocity was estimated during low tide (Planès et al., 2017). Joubert et al. (2018) applied the cross-correlation and deconvolution methods of seismic noise, to estimate a variation of less than 10% of relative surface wave velocity as a function of increasing sea level. It is noteworthy that these authors did not apply any inversion processing to their data sets.

Indeed, in the case of slight modifications in the medium, the inversion method must discriminate small parameter variations leading to several issues that alter the efficiency of the process and degrade its potential. These inaccuracies are due to accuracy limits in acquisition, dispersion data extraction, or inversion processes. Note that using passive measurements makes possible to continuously record the signal without any action at the source from the geophysicist. The problem of measurement errors is different from the active setup, but the inversion process is similar with the same limit problems. To overcome the problem of acquisition and phase velocity extraction, different works have proposed new approaches as a function of field conditions. For example, Le Feuvre et al. (2015) improved the determination of subsurface shear-wave velocity from ambient noise using cross-correlations and beamforming. Dangeard et al. (2018) proposed a statistical approach for estimating picking errors in the case of standard surface wave inversion for time-lapse studies. The latter tackled the repeatability issue of the method but did not overcome the "Realistic Error", the term given by O'Neill (2004), who used a statistical approach to define an uncertainty law for the extraction of the phase velocity. Studies on these effects (Lai et al., 2005; O'Neill, 2004) proved that the uncertainty in surface wave measurements has a greater impact on low frequencies, making it more difficult to assess deep media variations precisely. More recently, studies in a two-layer

medium (Wang et al., 2018) showed that conventional phase velocity dispersion curve inversion is not capable of estimating a variation ratio lower than 10% in the deep layer. Other possibilities for increasing the efficiency of results could be used to tackle the inversion process, for example the misfit function, which can be based on different norms or diagram distances (e.g. Wang et al. (2019)).

We can summarize the needs and problems described above as follows. The publications on dike monitoring mentioned show the interest of surface waves to identify areas of damage and water penetration. In order to monitor detailed evolutions before a potential break, the methodology must allow identifying small variations in surface wave velocity. This is not straightforward or even possible for the inversion of surface wave dispersion in the current classical procedure. In order to improve its performances, different levers can be used, some of which have been analyzed in the literature, such as errors on measurements and dispersion data extraction, or the distance norm between estimated and recorded data. However, despite the progress made in these studies, the results available are not sufficient to make the methodology effective if phase velocity variations are lower than 20%. Therefore, we propose here to study another lever that is complementary to the previous ones.

In this framework, our concern is to study the effect of the Rayleigh Phase Velocity Derivative with respect to frequency $\frac{dV_{ph}}{df}$ (abbreviated as PVD). More particularly, our aim is to study its sensitivity and impact on the convergence and precision of the inversion results. This proposition is based on the idea that information on the variation of a medium's properties as a function of depth is contained in the variation of the phase velocity as a function of frequency and thus potentially in the phase velocity derivative. Consequently, the PVD could provide more sensitive information on the shear-wave velocity depth profile in the medium. Firstly, to analyze the sensitivity of the PVD, qualitative and quantitative approaches regarding its behavior will be implemented before testing it on the inversion process. For these analyses, all the stages of the methods (including the geometry of the measurement setup and the inversion process) follow the most usual procedures for geophysical approaches in shallow media. The inversion method used is summarized hereafter.

The inversion stage consists in assessing the shear-wave velocity 1D model from surface wave dispersion data. To do this, a local or a global optimization method can be used. The global approach, which is used for our study, makes it possible to explore the parameter space without defining any initial model. It provides a set of possible models associated with a value of the misfit function. The latter indicates the error level, for example, thanks to a L2 norm, between the dispersion data extracted from measurements and those theoretically calculated. More precisely, the global optimization method used for this study is based on the Neighborhood Algorithm (NA), commonly used by geophysicists. The NA is a stochastic search method in a given parameter space, making use of Voronoi cells to compute the misfit function in the parameter space (Sambridge, 1999b). Like other global inversion methods (genetic algorithm, simulated annealing, etc.), the NA generates pseudo-random samples in the parameter. The originality of NA is that the new samples generated at each iteration are guided and improved by the previous ones. A later study by Wathelet (2008) improved the capacity of random model generation in a parameter space with irregular boundaries.

All these process stages will be used here for a two-layer medium with in-

creasing shear-wave and compressional-wave velocities as a function of depth, and for the fundamental mode which is considered as the most preponderant in this case (Foti et al., 2014; Socco et al., 2010). The aim is to determine the fundamental effects of the PVD on the most basic underground medium in the 1D case. The paper is organized as follows:

In a first part below, the two-layer reference model, the phase velocity derivative $\frac{dV_{ph}}{df}$, and its extraction are presented. In the second part, the behavior of the PVD is analyzed qualitatively by observing its variations over a frequency range for small velocity modifications. In the next part, the theoretical sensitivity of the PVD is calculated and analyzed. All these features are compared to those of the traditional dispersion data: the phase velocity and the group velocity of Rayleigh Waves. Then, inversion tests are provided and analyzed in the two last parts. These tests are performed respectively on theoretical dispersion curves and on experimental data recorded in the laboratory using two-layer resin models with a shear-wave velocity difference equal to 17% in the deep layer. These measurement data-sets are obtained to simulate at reduced scale field recordings carried out for typical shallow underground media.

## 3.2 Definition and Formulation of the Phase Velocity Derivative

In a homogeneous isotropic elastic linear medium, Rayleigh wave velocity is independent of frequency. The Rayleigh phase velocity $V_{ph}$ and group velocity $V_g$ are equal. However, in a multilayered medium, phase and group velocities are functions of the angular frequency $\omega$ (with the relation $\omega = 2\pi f$ and $f$ being the frequency) and wavenumber $k$, and defined as follows

$$V_{ph} = \frac{\omega}{k} \tag{3.1}$$

$$V_g = \frac{d\omega}{dk}. \tag{3.2}$$

The Rayleigh phase velocity can be written as a function of frequency, wavenumber and medium parameters $\mathbf{m_j}$ (shear-wave velocity $V_s$, compressional-wave velocity $V_p$, layer thickness $h$ and density $\rho$) with $j \in [1, 4]$:

$$V_{ph} = f(V_s, V_p, h, \rho, \omega, k), \tag{3.3}$$

Then, the phase velocity derivative can be expressed as follows:

$$dV_{ph} = \left[\frac{\partial V_{ph}}{\partial \omega}\right]_{k,m_j} d\omega + \left[\frac{\partial V_{ph}}{\partial k}\right]_{\omega,m_j} dk + \sum_{i}^{4} \left[\frac{\partial V_{ph}}{\partial m_j}\right]_{k,\omega} dm_j. \tag{3.4}$$

Since the medium parameters are independent of frequency, we can write $\frac{dm_j}{d\omega} = 0$. Then, dividing by the term $d\omega$ on both sides of **Eq. 3.4** gives

$$\frac{dV_{ph}}{d\omega} = \left[\frac{\partial V_{ph}}{\partial \omega}\right]_{k,m_j} + \left[\frac{\partial V_{ph}}{\partial k}\right]_{\omega,m_j} \frac{dk}{d\omega}. \tag{3.5}$$

Table 3.1: Parameters of a two-layer reference model. $V_p$: compressional-wave velocity; $V_s$: shear-wave velocity; $\rho$: density; $\nu$: Poisson's ratio; and $h$: layer thickness.

| layer ($i$) | $V_{p_i}^{ref}$ $[m/s]$ | $V_{s_i}^{ref}$ $[m/s]$ | $\rho_i^{ref}$ $[kg/m^3]$ | $\nu_i^{ref}$ | $h_i^{ref}$ $[m]$ |
|---|---|---|---|---|---|
| 1 | 1000 | 600 | 1500 | 0.22 | 8 |
| 2 | 2000 | 1100 | 2200 | 0.28 | $\infty$ |

The partial derivatives of phase velocity with respect to frequency $\left[\frac{\partial V_{ph}}{\partial \omega}\right]_k = \frac{1}{k}$ and to wavenumber $\left[\frac{\partial V_{ph}}{\partial k}\right]_\omega = -\frac{\omega}{k^2}$ are substituted in **Eq. 3.5**:

$$\frac{dV_{ph}}{d\omega} = \frac{1}{k} - \frac{\omega}{k^2}\frac{dk}{d\omega}, \tag{3.6}$$

and with the definition of group velocity in **Eq. 3.2**:

$$\frac{dV_{ph}}{d\omega} = \frac{1}{k} - \frac{\omega}{k^2}\frac{1}{V_g}. \tag{3.7}$$

Therefore, the analytical formulation of the phase velocity derivative with respect to frequency is

$$\frac{dV_{ph}}{df} = \frac{V_{ph}(V_g - V_{ph})}{fV_g}. \tag{3.8}$$

**Eq. 3.8** shows that the phase velocity derivative can be formulated as a function of the group and phase velocities, according their theoretical definitions. Note that since surface waves are mostly sensitive to shear-wave velocity (Takeuchi et al., 1972; Lai and Rix, 1998; Aki and Richards, 2002), only shear-wave velocity variations are considered in the following study (see sensitivity formulations in section 4). To study the phase velocity derivative $\frac{dV_{ph}}{df}$, sensitivity to small variations is first analyzed qualitatively and compared with the Rayleigh wave phase and group velocities. The study is based on a two-layer medium whose parameters are given in **Table 3.1** with $V_{p_i}$ being the compressional-wave velocity of the $i$th layer, $V_{s_i}$ the shear-wave velocity, $\rho$ the density and $\nu_i$ the Poisson's ratio. The thickness of the top layer is $8\,m$ and the deep layer is assumed to be semi-infinite.

To understand the basic behavior of $\frac{dV_{ph}}{df}$, the study proposed here deals with a 1D two-layer model as it is the most basic medium. The parameter values are chosen to be typical of simple subsurface media, as an illustrative case for the qualitative analysis. However, the analysis below is based on non-dimensional observations in order to be generalizable.

## 3.3 Parametric Study

Based on the reference model given in **Table 3.1**, we conducted a qualitative analysis of the inversion input data $V_{ph}$, $V_g$ and the phase velocity derivative with respect to frequency, $\frac{dV_{ph}}{df}$, to highlight the effects of the shear-wave velocity and first layer depth variations. The Geopsy software (Wathelet, 2004) is used to calculate the theoretical phase and group dispersion curves. The computation

of the theoretical dispersion curve is based on the eigenvalue problem originally described by Thomson (1950) and Haskell (1953) and then modified by Dunkin (1965). The propagator matrix method (Gilbert and Backus, 1966) is used to solve the eigenvalue problem in a 1D stratified medium. The root search is based on the Lagrange polynomial, which efficiently speeds up the calculations. Thanks to the rapidity of the computation, a series of phase and group dispersion curves are calculated for various media following the variation ratio defined as

$$\alpha(V_{s_i}) = \frac{\Delta V_{s_i}}{V_{s_i}^{ref}} = \frac{V_{s_i}^{var} - V_{s_i}^{ref}}{V_{s_i}^{ref}} \tag{3.9}$$

with $V_{s_i}^{ref}$ being the reference shear-wave velocity given in **Table 3.1** and $V_{s_i}^{var}$ the variable shear-wave velocity of the medium. The dispersion curves are calculated in a frequency band $[1, 150]\,Hz$ and represented as a function of wavelength normalized by the interface depth $h_1$ in order to obtain results that can be generalized as much as possible to other similar cases (i.e. other ranges of values but similar ratios compared to the propagating wavelength).

### 3.3.1 $V_{s_1}$ variation

The shear wave velocity of the first layer varies with a variation ratio $\alpha(V_{s_1}) \in [-5, 5]\%$ and a corresponding Poisson's ratio $\nu_1 \in [0.17, 0.26]$. **Fig. 3.1** shows, on the left, the phase and group velocities of the Rayleigh wave, as well as $\frac{dV_{ph}}{df}$, as a function of $\frac{\lambda}{h_1}$. The right part of **Fig. 3.1** shows variations of dispersion data ($\Delta V_{ph}$, $\Delta V_g$, $\Delta \partial_f V_{ph}$), normalized by the reference dispersion curves

$$(\Delta X)_{norm} = \frac{\Delta X}{X_{ref}} \times 100\% = \frac{X_{var} - X_{ref}}{X_{ref}} \times 100\% \tag{3.10}$$

with $X$ being the dispersion data and $X_{ref}$ the reference dispersion data when $\alpha(V_{s_1}) = 0$.

**Fig. 3.1** shows that $V_{ph}$ and $V_g$ vary over a wider range than $\frac{dV_{ph}}{df}$ for the wavelength range taken into account. However, the values of the dispersion data variations are higher when normalized by the reference model values. As expected, it can be seen that when the shear wave velocity of the first layer varies, the variations of $V_{ph}$ are larger for short wavelengths, i.e. higher frequencies. Also, for $\lambda \geq 4h_1$, they become very weak, which makes them indistinguishable from each other. Regarding the group velocity, the variations are also larger for shorter wavelengths and the maximum is reached for $\lambda \approx 3h_1$.

$\frac{dV_{ph}}{df}$ curves present variations over a different frequency range. Indeed, $\frac{dV_{ph}}{df}$ tends to zero for lower wavelengths for which the Rayleigh wave penetrates only in the shallow layer. When $\lambda \approx 3.2h_1$, where the values of $\frac{\delta V_{ph}}{\delta f}$ are minimum, their variations are significant and reach a normalized value equal to 20% for a 5% variation of velocity whereas it is about 10% for the group velocity. $(\Delta \partial_f V_{ph})_{norm} = 0$ at $\lambda \approx 5h_1$ and when $\lambda \geq 5h_1$, the variations are not as large as at short wavelengths. However they are more visible than the second lobes at $(\Delta V_{ph})_{norm}$ or $(\Delta V_g)_{norm}$.

Regarding the behavior for $\lambda = 3.2h_1$, a physical explanation can be given by analyzing the cumulative amplitude of displacement in depth depending on the wavelength. The figures are presented in Appendix D. Indeed, for the wavelength $\lambda = 3.2h_1$, the normalized amplitude of the particle displacement is 0.5

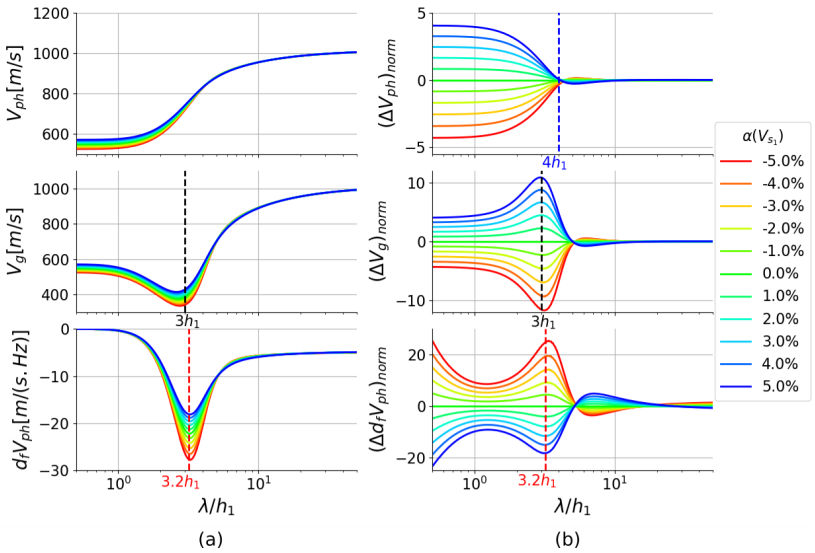


Figure 3.1: (a) Dispersion curves of the Rayleigh wave phase velocity (top), group velocity (middle) and phase velocity derivative (bottom) with the variation ratio $\alpha(V_{s_1}) = \pm 5\%$. (b) Normalized variations with respect to the dispersion curves of the reference model.

at the depth corresponding to the interface between the two media and the normalized cumulative amplitude is 0.5 (see **Fig. D.1** in Appendix D). This means that at the wavelength $\lambda = 3.2h_1$, 50% of the cumulative amplitude of the surface wave propagates in the shallow layer and 50% in the deep layer. Therefore, at this point, the propagation of the Rayleigh wave is influenced by both media. The cumulative amplitude derivative with respect to wavelength confirms that the variation is highest at $\lambda = 3.2h_1$ around the interface. By varying the frequency slightly, the dominant influence comes from the shallow or deep layer, depending on the direction of the variation. This corresponds to the inflection point of the phase velocity curve, where the absolute value of the first derivative (as a function of frequency) is maximal.

### 3.3.2 $V_{s_2}$ variation

The shear-wave velocity of a semi-infinite medium varies with the variation of ratio $\alpha(V_{s_2}) \in [-5, 5]\%$ which gives a Poisson's ratio of $\nu_2 \in [0.25, 0.31]$. Variations of phase and group velocities ($V_{ph}$, $V_g$) and the derivative of phase velocity $\frac{dV_{ph}}{df}$ are shown in **Fig. 3.2**.

It can be seen that the phase velocity is sensitive to variations of the deep layer at long wavelengths and the variations become increasingly larger as the wavelength grows. The same occurs for the group velocity: $(\Delta V_g)_{norm}$ equals zero at short wavelengths and increases as the wavelength increases. The values of $(\Delta V_g)_{norm}$ is maximum when $\lambda \approx 3.4h_1$ and returns to zero at $\lambda \approx 5.3h_1$. Then, with a change of sign, the variations of the group velocity are significant at long wavelengths. Variations of $V_{s_2}$ do not change the minima $\frac{\delta V_{ph}}{\delta f}$ location

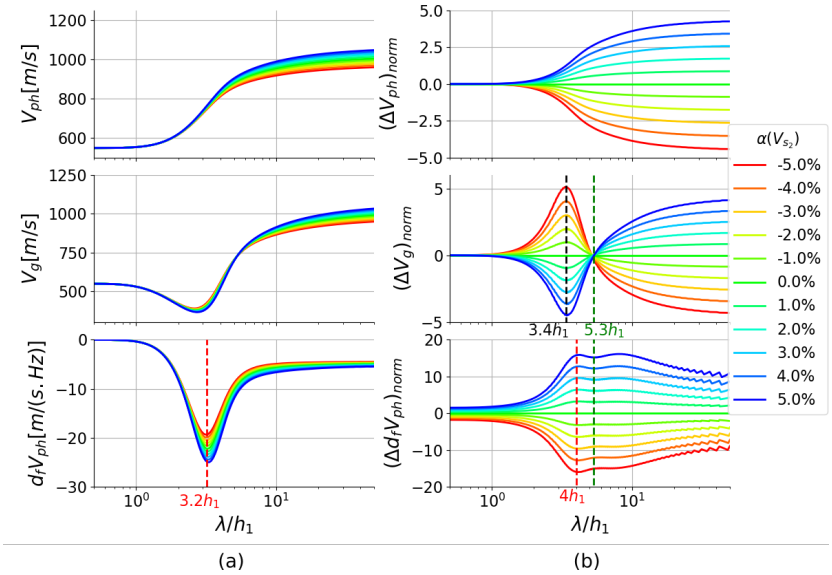


Figure 3.2: (a) dispersion curves of the Rayleigh wave phase velocity (top), group velocity (middle) and phase velocity derivative (bottom) with the variation of ratio $\alpha(V_{s_2}) = \pm 5\%$. (b) normalized variations with respect to reference model dispersion curves.

at $\lambda = 3.2h_1$. The variation of $\frac{dV_{ph}}{df}$ is maximum and decreases gradually along the wavelength with an inflection point around $\lambda = 5.3h_1$ where $(\Delta V_g)_{norm} = 0$.

### 3.3.3 $h_1$ variation

The PVD is a derivative of the phase velocity as a function of frequency, and which is used to calculate the phase velocity gradient. In a two-layer medium, the depth of the first layer changes the slope of the phase velocity dispersion curve. In the following we consider a variation in the depth of the first layer.

Interestingly, for a two-layer medium, the gradient of both the phase and group velocity dispersion curves with respect to wavelength is a linear function related to the thickness of the shallow layer, causing the minimum phase velocity derivative to occur at $\lambda = 3.25h_1$. Normalized variations (**Fig. 3.3**) show that the group velocity is more sensitive to changes in the depth of a shallow medium than the phase velocity, while the variations of the phase velocity derivative are much larger.

It is important to note that $(\Delta \partial_f V_{ph})_{norm}$ approaches infinity at a short wavelength for $h_1 = 4\,m$ and $6\,m$. This is because when calculating the relative difference, the reference curve approaches zero at a short wavelength, but the absolute difference between the reference and variation curves is relatively large, leading to a ratio close to infinity. This reflects the instability of the PVD at high frequencies, which demands precise processing of the measurement data, since small changes of data may cause huge deviations in the inversion results, thus affecting the overall assessment of the media. This requires more attention especially for inversion, as discussed in section 5: Numerical Illustration. How-

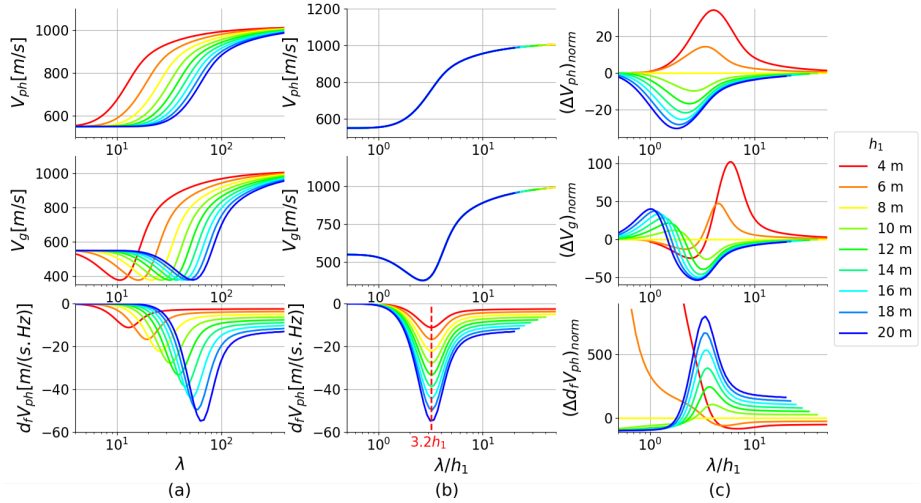


Figure 3.3: (a) Dispersion curves of the Rayleigh wave phase velocity (top), group velocity (middle) and phase velocity derivative (bottom) with depth variation $h_1 \in [4, 12]m$, as a function of wavelength. (b) Dispersion curves as a function of normalized wavelength. (c) Normalized variations of the dispersion data.

ever, in this first stage of the study, the results indicate that the high sensitivity of the PVD could lead to more accurate assessment of the evaluation properties of the depth profile $V_s$. Indeed, the sensitivity of the PVD under study is high at intermediate frequencies for which the dispersion data are generally stable if the frequency range of the source is chosen correctly. This would therefore permit distinguishing small differences between two media or small variations between two states of the same medium, such as in the case of monitoring the variation of water penetration in sea dikes (Planès et al., 2017; Joubert et al., 2018), or the water content in granular material (Pasquet et al., 2016; Dangeard et al., 2018).

Before testing this numerically with the inversion process, we propose in the following part to analyze the theoretical sensitivity behavior of the PVD. This approach will provide a general result regarding the points identified above.

## 3.4 Sensitivity Kernels

The formulation of the sentivity of the inversion input data to changes in a medium parameter is given by the partial derivative of this inversion data with respect to the medium parameter. Sensitivity can thus be calculated for the fundamental mode which is the subject of this study. It is intended to provide quantitative information on the effect of the medium variation on the inversion input data of interest, prior to future studies on the effects of higher modes, following the same principle. Here we follow the approach established by Aki and Richards (2002) for Love waves and apply it to Rayleigh waves to quantitatively compare the behavior of the different inversion input data analyzed, i.e. phase velocity, group velocity and the phase velocity derivative with respect to

frequency. In the first step, Hamilton's principle is applied to the Lagrangian density of the Rayleigh wave to deduce the fractional change in phase velocity at a given frequency

$$\left[\frac{\delta V_{ph}}{V_{ph}}\right]_{\omega} = \frac{1}{4V_g V_{ph} I k^2}\Big(\int_0^{\infty}(kr_1 + \frac{dr_2}{dz})^2\,\delta\Lambda dz + \int_0^{\infty}(2k^2 r_1^2 + 2(\frac{dr_2}{dz})^2 + (kr_2 - \frac{dr_1}{dz})^2)\,\delta\mu dz - \int_0^{\infty}(\omega^2(r_1^2 + r_2^2))\,\delta\rho dz\Big), \tag{3.11}$$

with $z$ being the depth, $\Lambda$ and $\mu$ Lamé coefficients, $r_1(k,\omega,z)$ and $r_2(k,\omega,z)$ Rayleigh displacement vectors in the horizontal and vertical directions, respectively, and $I = \frac{1}{2}\int_0^{\infty}\rho(r_1^2 + r_2^2)dz$ the energy integral. Aki and Richards (2002) described the method used to calculate the partial derivative of the Love phase velocity with respect to the medium parameter. Here, we perform the same work for the Rayleigh wave to obtain the following formulation:

$$\left[\frac{\partial V_{ph}}{\partial \Lambda}\right]_{\mu,\rho,\omega} = \frac{1}{4V_g I k^2}(kr_1 + \frac{dr_2}{dz})^2, \tag{3.12}$$

$$\left[\frac{\partial V_{ph}}{\partial \mu}\right]_{\Lambda,\rho,\omega} = \frac{1}{4V_g I k^2}\left[2k^2 r_1^2 + 2(\frac{dr_2}{dz})^2 + (kr_2 - \frac{dr_1}{dz})^2\right], \tag{3.13}$$

$$\left[\frac{\partial V_{ph}}{\partial \rho}\right]_{\mu,\Lambda,\omega} = -\frac{1}{4V_g I k^2}(\omega^2(r_1^2 + r_2^2)). \tag{3.14}$$

Given the equations of $V_p$, $V_s$ as a function of $\Lambda$, $\mu$, $\rho$: $V_p = \sqrt{\frac{\Lambda+2\mu}{\rho}}$ and $V_s = \sqrt{\frac{\mu}{\rho}}$, the sensitivity of the Rayleigh phase velocity as a function of depth, i.e. the partial derivatives of $V_{ph}$ as a function of the medium's parameters ($V_s$, $V_p$ and $\rho$) can be formulated as follows:

$$\left[\frac{\partial V_{ph}}{\partial V_p}\right]_{V_s,\rho,\omega} = \frac{V_p \rho}{2V_g I k^2}(kr_1 + \frac{dr_2}{dz})^2, \tag{3.15}$$

$$\left[\frac{\partial V_{ph}}{\partial V_s}\right]_{V_p,\rho,\omega} = \frac{V_s \rho}{2V_g I k^2}[(kr_2 - \frac{dr_1}{dz})^2 - 4kr_1\frac{dr_2}{dz}], \tag{3.16}$$

$$\left[\frac{\partial V_{ph}}{\partial \rho}\right]_{V_p,V_s,\omega} = \frac{V_p}{2\rho}\left[\frac{\partial V_{ph}}{\partial V_p}\right]_{V_s,\rho,\omega} + \frac{V_s}{2\rho}\left[\frac{\partial V_{ph}}{\partial V_s}\right]_{V_p,\rho,\omega} - \frac{1}{4V_g I k^2}\omega^2(r_1^2 + r_2^2). \tag{3.17}$$

Since there is no analytical expression for group velocity sensitivity (Aki and Richards, 2002), the sensitivity kernels for both the group velocity and the phase velocity derivative are calculated numerically. For group velocity, we use Taylor's theorem.

$$V_g(m) = V_g(m_0) + \left[\frac{\partial V_g}{\partial m}\right]_{m_0}(m - m_0) + h_1(m)(m - m_0), \tag{3.18}$$

with $m$ representing the medium's parameters and $lim_{m \to m_0} h_1(m) = 0$. Under this condition, we write

$$\left[\frac{\partial V_g}{\partial m}\right]_{m_0} = \frac{V_g(m) - V_g(m_0)}{m - m_0}. \tag{3.19}$$

For a given medium, the Rayleigh phase velocity can be expressed as a function of the frequency and the medium's parameters: $V_{ph} = f(\omega, V_s, V_p, \rho)$. The total derivative of the phase velocity is written as:

$$dV_{ph} = \frac{\partial V_{ph}}{\partial \omega} d\omega + \sum \frac{\partial V_{ph}}{\partial m} dm \tag{3.20}$$

with $m$ a vector of the medium parameters $V_s, V_p$ and $\rho$ which are independent of frequency, we obtain:

$$\frac{dV_{ph}}{d\omega} = \frac{\partial V_{ph}}{\partial \omega} + \sum \frac{\partial V_{ph}}{\partial m} \frac{dm}{d\omega} = \frac{\partial V_{ph}}{\partial \omega}. \tag{3.21}$$

According to the symmetry of second derivatives in mathematics, we can write:

$$\frac{\partial}{\partial \omega}\left(\frac{\partial V_{ph}}{\partial m}\right) = \frac{\partial}{\partial m}\left(\frac{\partial V_{ph}}{\partial \omega}\right) = \frac{\partial}{\partial m}\left(\frac{dV_{ph}}{d\omega}\right). \tag{3.22}$$

Thus, the sensitivity kernel of the phase velocity derivative can be assessed numerically by calculating the gradient of $\frac{\partial V_{ph}}{\partial m}$, related to the frequency. The latter was calculated previously as the Rayleigh phase velocity sensitivity. The resulting sensitivity kernels for each inversion input data, i.e. phase velocity, group velocity and its derivative, for the fundamental mode, are presented in **Fig. 3.4** as a function of normalized wavelength. Note that, as mentioned previously, for this study, the sensitivity is calculated and presented as related only to the shear-wave velocity parameter. In **Fig. 3.4**, the blue curves show the sensitivity of the inversion input data to variations of shear-wave velocity of the shallow layer ($V_{s_1}$) and orange curves show the shear-wave velocity of the half-space $V_{s_2}$ variations. To make the results comparable, all the curves are normalized by the maximum sensitivity value of each inversion input data.

In **Fig. 3.4**, it can be seen that with $V_{s_1}$ variations, both $V_{ph}$ and $V_g$ have high sensitivity values at short wavelength. However, when variations occur in the deep layer ($V_{s_2}$), it is necessary to have a long wavelength to obtain more sensitivity, but precise estimation of the medium is difficult due to high uncertainties (Lai et al., 2005). In contrast, the resulting sensitivity of the PVD is found to be significant at $\lambda \approx 3.4h_1$ for both $V_{s_1}$ and $V_{s_2}$ variations. From the standpoint of inversion, regarding this two-layer reference medium, this behavior indicates that the shear-wave velocity variations occurring in whichever layer can be estimated by the phase velocity derivative over a limited range of wavelengths, where the phase velocity derivative is sensitive.

The analysis of the sensitivity kernel in **Fig. 3.4** is in good agreement with the previous qualitative analysis shown in **Fig. 3.3**. The maximum sensitivity and largest variations of the phase velocity derivative occur for the same order of wavelength ($\lambda \approx 3.4h_1$). In addition, the sensitivity kernels for models with different first layer depths ($h_1$) but with the same shear-wave velocities are also calculated. The same conclusion as for the qualitative analysis is also found: the

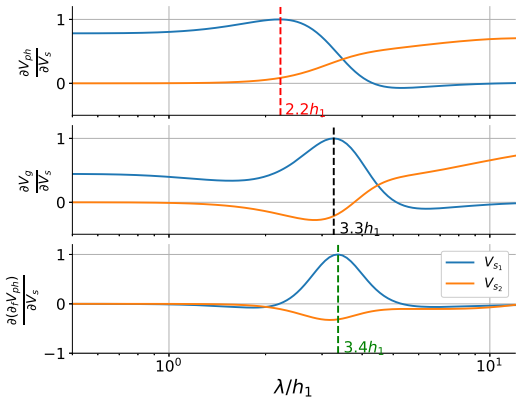


Figure 3.4: Rayleigh phase velocity sensitivity kernel (top), group velocity sensitivity kernel (middle) and phase velocity derivative sensitivity (below) with respect to the shear-wave velocities of the shallow layer ($V_{s_1}$) and the deep layer $V_{s_2}$. Sensitivity values normalized by the maximum value of sensitivity with respect to $V_{s_1}$ and presented as a function of wavelength normalized by the depth of the shallow layer $h_1$.

maximum sensitivity of the phase velocity derivative still occurs for $\lambda \approx 3.2h_1$, under the assumption of fixed model shear-wave velocities.

## 3.5 Inversion Tests

In the previous two sections, we discussed the sensitivity of the PVD $\frac{dV_{ph}}{df}$ both qualitatively and quantitatively. In this part, we apply $\frac{dV_{ph}}{df}$ in a numerical inversion problem to verify its feasibility. Three types of dispersion data are taken as inversion input data: $V_{ph}$, $V_g$ and $\frac{dV_{ph}}{df}$. For that, theoretical dispersion curves of $V_{ph}$ and $V_g$ are calculated using Geopsy software (Wathelet, 2004). The PVD is then calculated using **Eq. 3.8**. Note that, since only the fundamental mode is tackled, the dispersion curve calculated is that of the fundamental mode only.

The parameters of the reference model are presented in **Table 3.1** and we assume that the medium has undergone minor changes such that its shear wave velocities change with variation ratios $\alpha(V_{s_i}) \leq 5\%$. The dispersion curves are calculated for the reference model and the models with shear-wave velocity variations in a frequency range $[1, 160]\,Hz$ with a frequency sampling step of $0.5\,Hz$. This frequency band has been chosen for these inversion tests because it corresponds to that of an ideal pulse source centered on $50\,Hz$, this central value being itself typical of a hammer shot used in subsurface geophysics. **Fig. 3.5** presents the dispersion curves of the three dispersion data, as function of frequency.

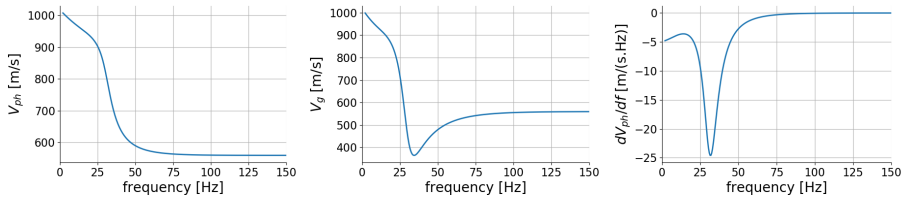


(a) (b) (c)

Figure 3.5: Theoretical dispersion curves of the reference medium (**Table 3.1**). (a) $V_{ph}$, (b) $V_g$, (c) $\frac{dV_{ph}}{df}$.

### 3.5.1 Misfit function and a priori information

The dispersion data are tested below for an inversion process by a global optimization through the Neighborhood Algorithm (NA), as indicated in the introduction: the NA computes the misfit function in the parameter space, where the pseudo-random samples are generated at each iteration by making use of Voronoi cells, and then guided and improved by the samples generated at the previous iteration. Each sample corresponds to one ground model (i.e. a set of the research parameters: $V_s$ of each layer in the model) and corresponds to one calculated dispersion curve using Geopsy software. The objective (also called misfit) function is defined as the L-2 norm relative difference between measured and calculated inversion data values, $x_{mes}$ and $x_{cal}$ respectively, in the frequency domain

$$misfit = \sqrt{\frac{1}{N_f}\sum_{i}^{N_f}(\frac{x_{mes} - x_{cal}}{x_{mes}})^2}, \tag{3.23}$$

where $N_f$ is the number of inversion input data in the frequency domain, $x$ is the inversion input data, $V_{ph}$, $V_g$ or $\frac{dV_{ph}}{df}$. We define an indicator function such that its value is between 0 and 1

$$P = e^{-misfit}. \tag{3.24}$$

In our inversion, the compressional-wave velocity $V_p$, the first layer depth $h_1$ and the density $\rho$ are fixed, only the shear-wave velocities of both layers $V_{s_i}$ are inverted and are searched in the domain $[-20\%, +20\%] \times V_{s_i}^{ref}$. NA needs several tuning parameters in an inversion process: $n_{s_0} = 50$ the number of samples randomly distributed in the parameter space as well as the Voronoi cells number at the initial iteration; $n_r = 5$ the number of best cells to consider for the next iteration; $n_s = 10$ the number of new generating samples at each selected cell; and $n_i = 15$ the total number of iteration. Finally, a total of 800 $(= n_{s_0} + n_r \times n_s \times n_i)$ models are calculated in each inversion.

### 3.5.2 Inversion results of $V_{ph}$ and $V_g$

**Fig. 3.6** and **Fig. 3.7** present the inversion results of the phase velocity and the group velocity, respectively, with each dot corresponding to one inverted model. Black dots are inversion results for the reference medium ($\alpha = 0$) and

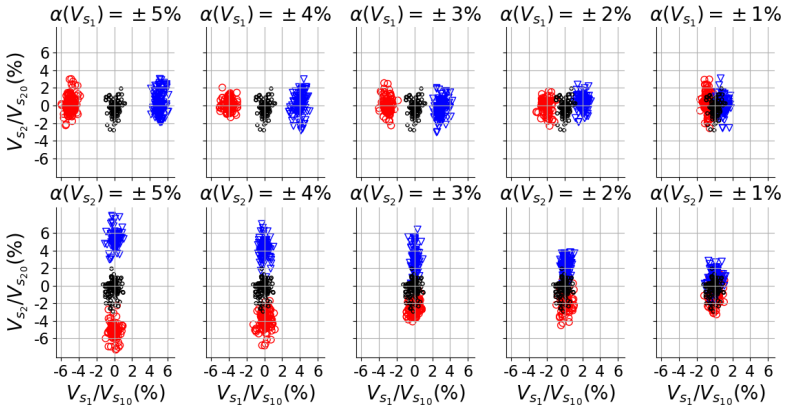


Figure 3.6: $V_{ph}$ inversion results. Each dot corresponds to one inverted model with the colors representing reference and shear-wave velocity variation media. Black: $\alpha(V_{s_i}) = 0$; red: $\alpha(V_{s_i}) < 0$; blue: $\alpha(V_{s_i}) > 0$.

blue dots are inverted models for the medium with the variation $\alpha > 0$, the red dots represent $\alpha < 0$. A maximum probability value of 99% (99%$P_{max}$) is used as a limit for all the inversion models in each inversion, which means only the models with $P \geq 0.99\, P_{max}$ are selected as acceptable. In each figure, the top four images show the selected inversion results when small variations occur in the shallow medium ($\alpha(V_{s_1})$), and the bottom four correspond to the cases of small variations in the deep medium ($\alpha(V_{s_2})$).

For both the phase velocity and the group velocity (**Fig. 3.6, Fig. 3.7**), when small variations occur in the shallow medium $\alpha(V_{s_1})$, those greater than 3% can be well estimated because the inversion results can be clearly distinguished from those of the reference model. When the variation is equal to 2%, the inversion results begin to overlap and when $\alpha(V_{s_1}) = 1\%$, the inversion results cannot be separated. For variations in the deep medium ($\alpha(V_{s_2})$), the inversion results overlap when $\alpha(V_{s_2}) = 4\%$. Therefore, in this two-layer medium, the classical inversion method can estimate variations of the shear-wave velocity in the shallow medium which are greater than 3%. However, for variations in the deep medium, only variations greater than 5% can be estimated.

### 3.5.3 Inversion results of $\frac{dV_{ph}}{df}$

As shown in section 3, the qualitative analysis of the behavior of the PVD, $\frac{dV_{ph}}{df}$ tends to zero at high frequencies (short wavelengths) where the shear-wave velocity variation is small (see **Fig. 3.5**), which causes the objective function to tend to infinity. Consequently, the inversion of $\frac{dV_{ph}}{df}$ tends to find models that better fit the dispersion curves at high frequencies. To avoid this problem, we propose here to invert a combined dispersion curve by using the derivative of the dispersion velocity for lower frequencies and dispersion velocities for the higher frequencies. The frequency limit between the two ranges is chosen here in order to integrate the derivative of the phase velocity over a sufficiently wide range including the zone of maximum sensitivity. According to the sensitivity curves of $\frac{dV_{ph}}{df}$ (**Fig. 3.4**), $\frac{dV_{ph}}{df}$ is most sensitive when $\lambda \in [2, 6]h_1 = [16, 48]\, m$,

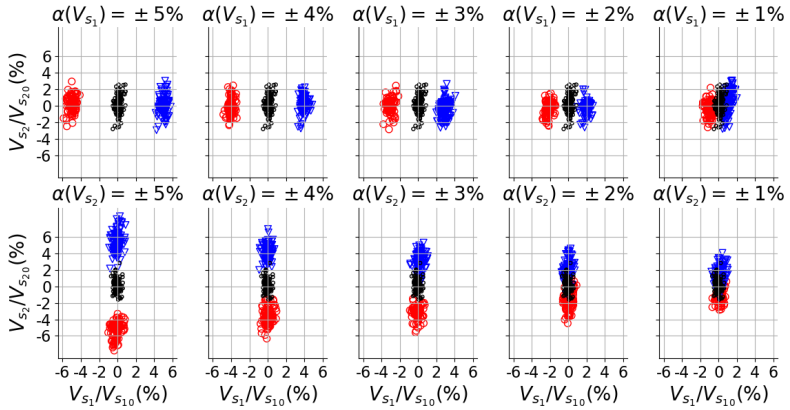


Figure 3.7: $V_g$ inversion results. Each dot corresponds to one inverted model with the colors representing reference and shear-wave velocity variation media. Black: $\alpha(V_{s_i}) = 0$; red: $\alpha(V_{s_i}) < 0$; blue: $\alpha(V_{s_i}) > 0$.

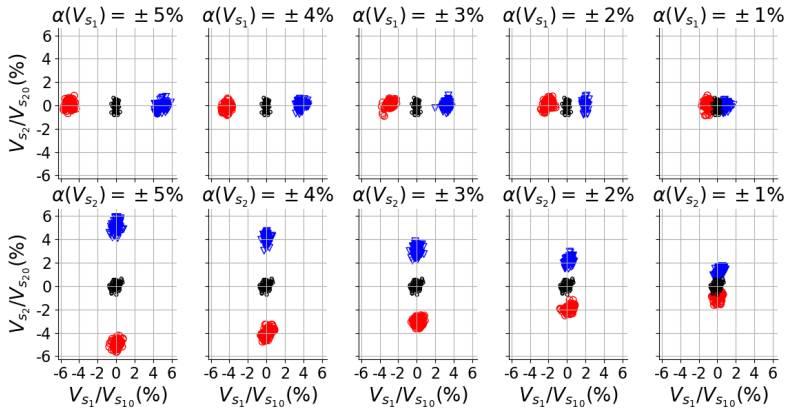


Figure 3.8: Combined data inversion results. Each dot corresponds to one inverted model with the colors representing reference and shear-wave velocity variation media. Black: $\alpha(V_{s_i}) = 0$; red: $\alpha(V_{s_i}) < 0$; blue: $\alpha(V_{s_i}) > 0$.

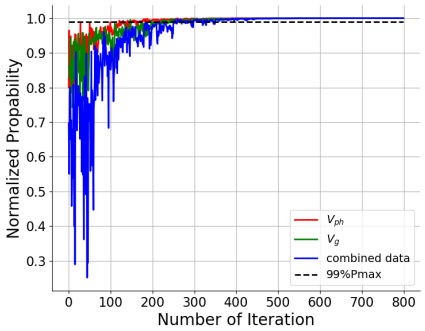


Figure 3.9: Normalized probability curves for $V_{ph}$, $V_g$ and combined dispersion curves as function of iteration number.

which corresponds to the frequency range $[20, 40]\,Hz$ in the tested case. Thus, the combined dispersion curve is $\frac{dV_{ph}}{df}$ when $f < 60\,Hz$ and $V_{ph}$ when $f \geq 60\,Hz$. Note that the frequency range limits for $\frac{dV_{ph}}{df}$ have been chosen here by considering the part of the dispersion curves featuring the higher variations but it remains arbitrary. This choice for the limits values could be driven by a benchmark test approach in further studies with the objective to automatically recover the optimum values of the frequencies boundaries.

**Fig. 3.8** shows that the combined data inversion has a quasi-equivalent estimation for the shallow layer $V_{s_1}$. But when variations occur in the deep medium, the inversion of the combined data better estimates small $V_{s_2}$ variations. The normalized convergence curve of the indicator $P$ in **Fig. 3.9** shows that all inversion processes converge after around 300 iterations and the number of selected models for both inversions varies between $[550, 650]$. In order to obtain a clearer view of the selected models, they are presented quantitatively in **Fig. 3.10**.

The inversion results of the combined dispersion curve and $V_{ph}$ are shown in **Fig. 3.10**: the inverted shear-wave velocities are plotted as a function of the variation ratio $\alpha$. The black line presents the expected values, and the colored zones show, extreme inverted values for $V_{ph}$ (red zone) and the combined dispersion curve (grey zone), respectively, which correspond to extreme $V_s$ values in **Fig. 3.8**. The advantage of combined data inversion is obvious for $V_{s_2}$ because the result area is narrower around the expected value. In the next section, the procedure is tested with real laboratory measurements.

## 3.6 Application on Real Data from Laboratory Measurements

Two reduced-scale models made of epoxy resin (**Fig. A.1**), were designed to validate and illustrate our results experimentally. The parameters and dimensions of the first model (named *baseline*) are given in **Table 3.2**. Using the sample parameters provided by previous studies on this type of resin (Filippi et al., 2019), we calculated the size of the model to minimize and delay the boundary effects. Moreover, the latter are reduced because the borders of the

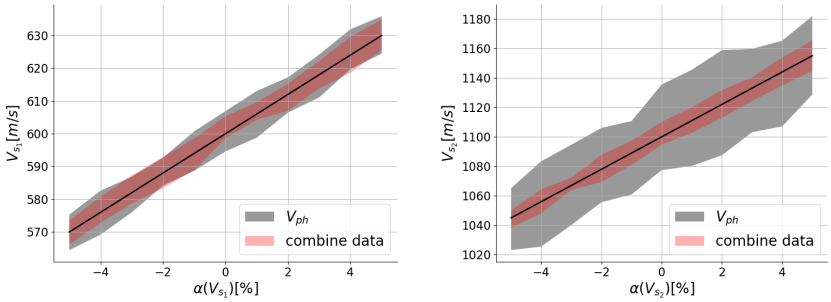


(a) (b) $V_{s_2}$

Figure 3.10: Inversion results of shear-wave velocities for (a) shallow layer $V_{s_1}$ and (b) deep layer $V_{s_2}$, using $V_{ph}$ and $\frac{dV_{ph}}{df}$ separately. The black line presents the exact shear-wave velocity value for each variation ratio $\alpha$.

Table 3.2: *Baseline* model parameters and dimensions. $h_i$: layer thickness; $l$ and $w$: length and width of model. Scale ratio between the numerical and the experimental model dimensions is 1000.

| layer | $V_{p_i}$ $[m/s]$ | $V_{s_i}$ $[m/s]$ | $\rho_i$ $[kg/m^3]$ | $\nu_i$ | $h_i$ $[mm]$ | l $[mm]$ | w $[mm]$ |
|---|---|---|---|---|---|---|---|
| 1 | 1300 | 703 | 450 | 0.29 | 8.0 | 265 | 235 |
| 2 | 2048 | 933 | 1300 | 0.37 | 203 | 265 | 235 |

models are rounded using a radius larger than or equal to the central wavelength (Pageot et al., 2015). The radius of the rounded borders is $12\,mm$ ($r \approx \frac{V_R}{f}$) and is identical for both resin models. The second model (named *repeatline*) was similar to the first one but with a higher shear-wave velocity in depth. The variation ratio is $\alpha(V_{s_2}) = 17\%$ as $V_{s_2} = 1100\,m/s$ for the *repeatline* model.

### 3.6.1 Model Measurements

The measurements were conducted in the MUSC (Measurement at Ultrasonic SCale) laboratory which permits carrying out seismic analogical measurements at reduced scale (Bretaudeau et al., 2011). The scale ratio between the numerical and experimental model dimensions is 1000, i.e. $1\,m$ in the numerical model is $1\,mm$ in the laboratory model, and $1\,Hz$ corresponds to $1\,kHz$ (Pageot et al., 2017). A Ricker wavelet with a central frequency of $100\,kHz$ was generated with a dry contact point piezoelectric transducer and the signals were recorded with a moving laser interferometer, with a sampling rate equal to $10\,MHz$ (see **Fig. A.1 (a)** in Appendix A for an illustration of the experimental set-up). More specifications of the MUSC measurement bench are available in (Bretaudeau et al., 2011) for any reproduction of the experiment. **Fig. A.1 (b)** in Appendix A shows the position of the piezo-electric source and the measurement points of the laser receivers (maximum offset equal to $90\,mm$ with a space of $1\,mm$). Like all the recordings published from the MUSC bench, the measurements are available to the scientific community and can be obtained as free data on request by email.

Seismograms measured on the two models were then analyzed and processed.

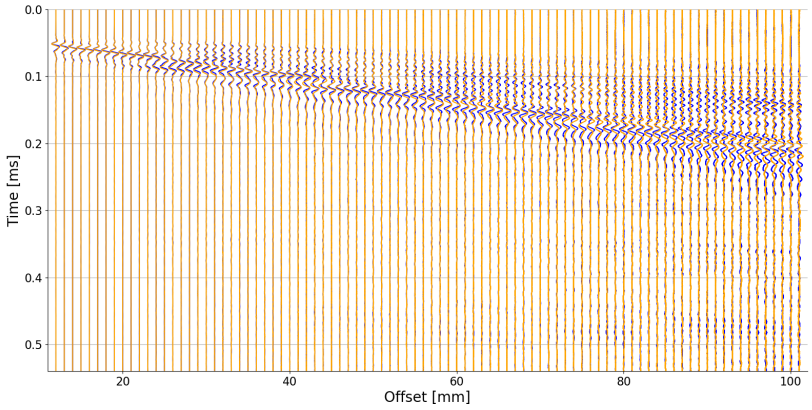


(a)

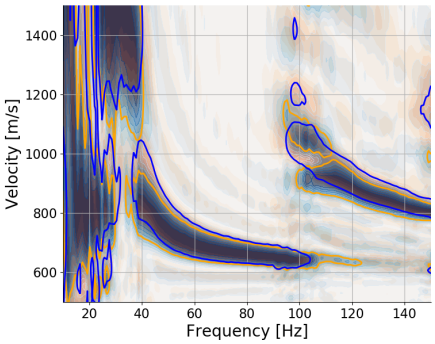


(b)

Figure 3.11: (a) Measured seismograms for the baseline model (orange) and the repeatline model (blue), normalized by maximum values at each trace. (b) Dispersion diagrams for the baseline (orange) and the repeatline (blue), normalized by the maximum value at each frequency. The value of the contour line is equal to 0.5. The measured dispersion diagrams are presented separately in **Fig. A.3** for a clear display of each one.

**Fig. 3.11 (a)** shows the measured *baseline* and *repeatline* seismograms. The phase velocity dispersion diagrams are extracted from the measured seismograms, using the phase-shift method (**Fig. 3.11 (b)**). The dispersion diagrams are calculated in the frequency range $[10, 150]\,Hz$ and at each frequency, the phase velocity is searched in the velocity range $[500, 1500]\,m/s$ with the velocity resolution equal to $2\,m/s$. They are then normalized by the maximum value at each frequency and the value of the contour line plotted is 0.5. The difference is visible between the diagrams at low frequency, which corresponds to velocity variations in the deep layer. The $V_{ph}$ dispersion curves are then extracted by automatic picking and their gradients give the $\frac{dV_{ph}}{df}$ dispersion curves (**Fig. 3.12**).

It should be pointed out that the PVD is extracted here using the gradient of the measured phase velocity curve instead of using the group velocity as proposed in **Eq. 3.8**. As he matter of fact, the high contrast of the shear wave velocity between the two layers, which gives a very steep variation of the group velocity as a function of frequency (i.e. a high dispersion), makes the choice of the frequency filter range, in the MFM procedure described in introduction, too difficult for accurately defining the group velocity required in **Eq. 3.8** for $\frac{dV_{ph}}{df}$. Indeed, a wide frequency range can bias the central frequency where the group velocity is searched; on the contrary, a narrow frequency range cannot contain enough energy to estimate the group velocity properly. This critical point of the group velocity assessment, above the scope of this study, should be tackled in further approaches, as mentioned in the final discussion of this paper.

As previously stated, only the fundamental mode is inverted. The cut-off frequency at high frequencies is fixed at $90\,kHz$ to avoid the higher mode perturbation for both baseline and repeatline models. The signals at low frequency (below $35\,kHz$), which presents a low signal-to-noise ratio and requires unavailable large receiver offset to be correctly assessed and mitigate the near field effects as highlighted by Bodet et al. (2009), who recommend a minimum frequency such as the maximum wavelength is lower than half of the receiver offset, are not used. According to these criteria, in the following, the frequency band is chosen in $[35, 90]\,Hz$ for both models. See **Fig. A.3** for a better visualization. However, as mentioned in the previous part concerning the theoretical tests, a further study should deal with the frequencies boundaries that can be automatically defined for optimal results.

The PVD $\frac{dV_{ph}}{df}$ and the classical dispersion data $V_{ph}$ are now inverted to perform an accurate evaluation of the difference between the two models. As in section 5, the inversions are carried out using $V_{ph}$ and combined dispersion curves. The combined dispersion curve consists of $\frac{dV_{ph}}{df}$ at medium frequencies ($f \in [42, 70]\,Hz$) and $V_{ph}$ at low and high frequencies ($f \in [35, 42] \cup [70, 90]\,Hz$). These limits are defined to avoid both an oscillation effect at low frequencies and a normalization problem at high frequencies. In the following, we invert the $\frac{dV_{ph}}{df}$ dispersion curve, without the normalization in the misfit function, and discuss its robustness.

### 3.6.2 Inversion results

In the Neighborhood Algorithm inversion process, we consider the compressional-wave velocity and density set as provided in **Table 3.2**. The shear-wave ve-

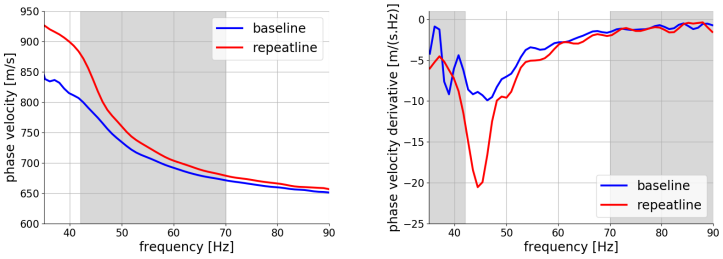


(a) (b)

Figure 3.12: Measured dispersion curves of (a) the phase velocity $V_{ph}$ and (b) the phase velocity derivative $\frac{dV_{ph}}{df}$. The combined data of *baseline* and *repeatline* consist of non-gray parts of the blue and red curves in the two images, respectively.

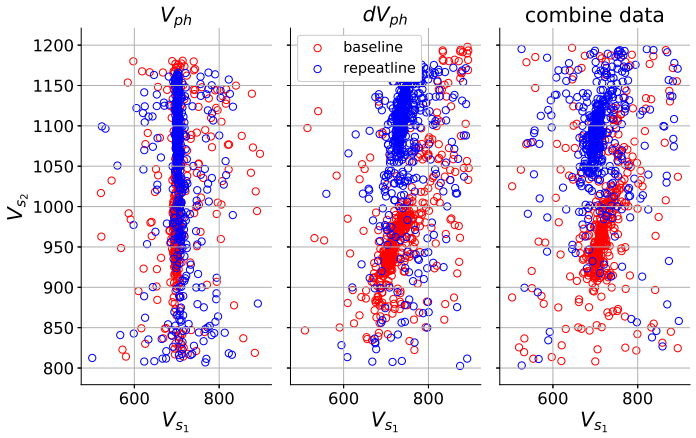


Figure 3.13: Inversion results of baseline (red) and repeatline (blue).

locities of each layer are searched in the range $V_{s_1} \in [500, 900]\, m/s$, $V_{s_2} \in [800, 1200]\, m/s$ and in the depth of the first layer in the range $h_1 \in [7.2,\ 8.8]\, m$. **Fig. 3.13** shows the resulting couples of shear-wave velocities ($V_{s_1}$,$V_{s_2}$) recovered by all the inversion processes, where $V_{s_1}$ and $V_{s_2}$ correspond to the shallow and deep layer, respectively. The results are shown for all three inversions: solely $V_{ph}$, solely $\frac{dV_{ph}}{df}$, combined $V_{ph}$ and $\frac{dV_{ph}}{df}$ curves. There are 1520 models ($n_{s_0} = 20$, $n_r = 10$, $n_s = 10$, $n_i = 20$) in each inversion process and the convergence indicator curves are plotted in **Fig. 3.14**. The convergence curves of $V_{ph}$ and combined data inversions tend towards the same level but reach a lower value for $\frac{dV_{ph}}{df}$ because of the non-normalization in the misfit function.

The result scatter plots in **Fig. 3.13** focus more on the true value on the $V_{s_1}$ axis when $V_{ph}$ is considered for the inversion than when it is for the other inversion data. However, $\frac{dV_{ph}}{df}$ and the combined data inversions give better estimations on $V_{s_2}$, as we can see better discrimination between the results of the baseline and repeatline models. To analyze the inversion results quantitatively,

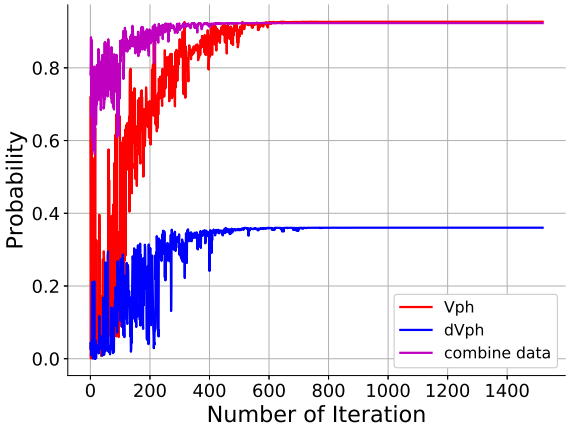


Figure 3.14: Probability curves for baseline inversion using $V_{ph}$, $\frac{dV_{ph}}{df}$ and combined dispersion curves, respectively.

histograms of inverted models are shown in **Fig. 3.15**, as a function of inverted $V_{s_1}$ and $V_{s_2}$, separately. $\mu_b$ and $\sigma_r$ are mean values and standard deviations for each group of models where $b$ represents the baseline and $r$ the repeatline. As there is no variation in the shallow layer between *baseline* and *repeatline*, the two inverted $V_{s_1}$ should be identical.

Compared to $\frac{dV_{ph}}{df}$ and combined data inversion, $V_{ph}$ inversion provides inverted $V_{s_1}$ values with smaller standard deviations for both *baseline* and *repeatline*, which corresponds to the more focused results in **Fig. 3.13**. In **Fig. 3.15 (a)**, the two histograms of combined data inversion are superimposed but the differences between $\mu_b$ and $\mu_r$ are significant due to several bigger inverted $V_{s_1}$ values of the repeatline (the part between 710 and 750 $m/s$).

The assessment of the deep layer variation is presented in **Fig. 3.15 (b)**. The variation ratio $\alpha(V_{s_2})$ is equal to $16.0 \pm 0.7\%$ for $V_{ph}$ alone, $16.4 \pm 1.1\%$ for $\frac{dV_{ph}}{df}$ alone and $17.1 \pm 0.3\%$ for combined data inversions. The result of $V_{ph}$ is smaller than the reference value 17%, and the error of the $\frac{dV_{ph}}{df}$ inversion result is larger than that of the other two inversions. The result of the combined data inversion is not only the closest to the expected reference value but it also has the smallest error. The improvement of the combined approach on the experimental data may seem small. However, the relative error with respect to the true model is divided by 2 and 6 depending on the data set, and the standard deviation is divided by 1.7 in both cases.

Using the mean values of the inverted models in **Fig. 3.15**, the calculated dispersion curves and the measured dispersion curves are plotted for the baseline and the repeatline in **Fig. 3.16**. We can see that the dispersion curve calculated from the inversion results of $\frac{dV_{ph}}{df}$ is wholly above the measured curves, in both **Fig. 3.16 (a)** and **(b)** although their corresponding derivative curves fit well with the trend measured in **(c)** and **(d)**. Indeed, two "parallel" dispersion curves share one gradient curve, which means using only $\frac{dV_{ph}}{df}$ for the optimization search in the inversion process can result in the identification of several solutions

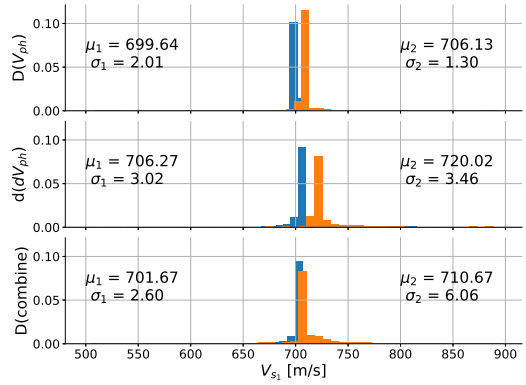


(a)

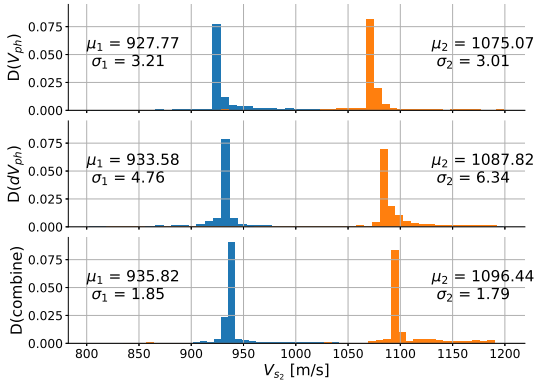


(b)

Figure 3.15: Density histograms of baseline (blue) and repeatline (orange) inverted models as a function of (a) $V_{s_1}$ and (b) $V_{s_2}$. The surface of each histogram is equal to 1.

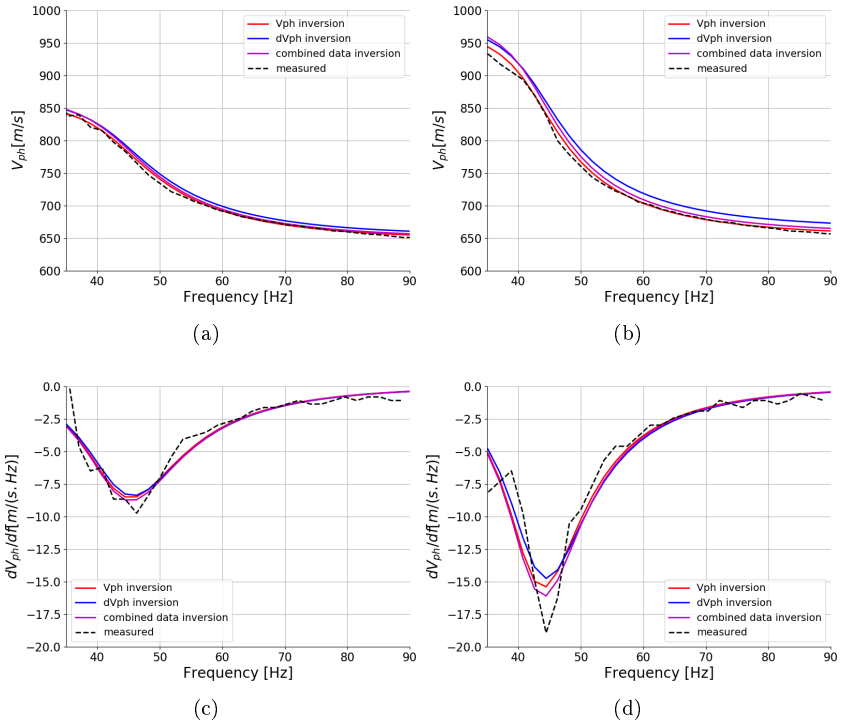


Figure 3.16: (a) and (b): Phase velocity dispersion curves for the measured data of (a) *baseline* and (b) *repeatline*, and their corresponding inverted models from different inversion data. (c) and (d): Phase velocity derivative dispersion curves for the measured data of (c) *baseline* and (d) *repeatline*, and their corresponding inverted models.

that do not correspond to the real model. The combined data method avoids this problem since $V_{ph}$ replaces $\frac{dV_{ph}}{df}$ at both low and high frequencies. Thus, when using the combined data in inversion, both the high sensitivity of $\frac{dV_{ph}}{df}$ and the calibration value to $V_{ph}$ are taken into account. The results of the combined data inversion in **Fig. 3.16 (c)** and **(d)** are closer to the minimum values of the measured curves.

Viewed globally it should be noted that the MASW approach involves several steps regarding the overall indeterminacy of the method: the measurements and their uncertainties, the extraction of the dispersion data, the convergence of the inversion process according to the criterion of the cost function and the inversion input data and its sensitivity. This study proposed to explore the effects of introducing the derivative of the Rayleigh wave phase velocity (PVD) in the process, independently of the issue of the measurement errors. Indeed, dissociating the effects of the different key elements of the process is crucial for the first stage. However further works will attempt to associate the effects of the measurements errors in order to identify their impacts. Thus, integrating the effect of errors on the data will contribute to the feasibility of the method in specific cases.

## 3.7 Conclusion and discussion

In this paper, the derivative of the Rayleigh wave phase velocity $\frac{dV_{ph}}{df}$ is introduced in the surface wave inversion method, to estimate small variations in media (variation ratio smaller than 10%). Based on two-layer media, we discussed the performance of the PVD when small variations occur in both layers, in particular shear-wave velocity variations. In the qualitative analysis, the dispersion curves of $V_{ph}$, $V_g$ and $\frac{dV_{ph}}{df}$ were calculated theoretically for several series of two-layer media with variations of shear-wave velocities and the depth of the shallow layer. $\frac{dV_{ph}}{df}$ displayed greater sensitivity compared to the phase and group velocities, especially for the deep layer variations: for the deep layer when the shear-wave velocity variation was equal to 5%, the variation of $\frac{dV_{ph}}{df}$ was around 18% while it was only 5% for $V_{ph}$ and $V_g$. Then, in the quantitative analysis, the calculation of sensitivity curves confirmed that $\frac{dV_{ph}}{df}$ contained information from both layers when $\lambda \approx 3.4h_1$. As a reminder, the sensitivity of $V_{ph}$ and $V_g$ follows the following rule: a variation of the shallow layer provided high sensitivity at a short wavelength while a long wavelength was needed for high sensitivity to variation in the deep layer.

The feasibility of using $\frac{dV_{ph}}{df}$ was then verified numerically by inverting the dispersion curves calculated from synthetic noisy signals. The high sensitivity of $\frac{dV_{ph}}{df}$ was particularly interesting but it should be used with care in the inversion process, due to its high oscillation in the case of noise and to the derivative property which leads to confusion with the $V_{ph}$ curves that share the same gradient in the frequency domain. To avoid this problem, we proposed to use combined data that consists of $V_{ph}$ and $\frac{dV_{ph}}{df}$. We verified that the combined data contained both the high sensitivity of $\frac{dV_{ph}}{df}$ and the robustness of $V_{ph}$ at the same time. Then, two two-layer models made of resin-epoxy were used to illustrate this result experimentally. The difference between them was a 17% variation of shear-wave velocity in the deep layer. The $V_{ph}$ inversion estimated

the variation of the deep layer at (16.4±1.1)% while the combined data inversion estimated the variation of the medium at $(17 \pm 0.3)\%$. Moreover, regarding the expected velocity values of the deep layer, the combined method gives more precise results with a smaller error, which are divided by 1.9 and 6.9 depending on the data set as well as standard deviations divided by 1.7. This improvement makes sense when looking at changes in media for small variations such as in continuous monitoring.

The methodology proposed, which combined the two inversion data, used the performance of each one valid over distinct frequency ranges, and combined them over the whole frequency range of the measured data. The results showed that it is an appropriate inversion strategy because it allows using the phase velocity derivative over the frequency range for which it is most sensitive. We proposed to define this frequency range according to the feature of the phase velocity derivative: its use was limited to the part for which it presented a minimum, without taking into account the areas for which the result of the calculation showed strong oscillations at lower frequencies or the plateau area for the higher frequencies. However, this criterion remained qualitative here and could be the subject of further studies in the near future. It will also be interesting to analyze the behavior of the PVD for higher modes. Indeed, the experiments, which were carried out on two-layer epoxy resin models, confirmed that $\frac{dV_{ph}}{df}$ is complementary to $V_{ph}$ in the inversion. Work is now in progress using epoxy resin models with smaller variations of mechanical properties, and time-lapse inversion.

Moreover, other major points should be investigated in further studies: the experimental tests in the last part on real measurements have highlighted the complexity of using the low frequency signal. The dispersion uncertainties for the lowest frequencies in the case of subsurface measurements are due, on the one hand, to the effects of near fields and, on the other hand, to the ratio between phase shift and wavelength (Bodet et al., 2009). Therefore, we propose, for future studies, to characterize all the uncertainties, including those for lower frequencies, for the phase velocity but also for the calculation of its derivative. The range of uncertainty for each frequency can be linked to the width of the lobe envelope associated with the fundamental mode in the dispersion diagram. The limits of this lobe can be computed analytically as proposed by (Wang et al., 2020a). Derivatives of these limits as a functions of frequency, also analytically available, could identify the uncertainty associated with the phase velocity derivative. The effects of these uncertainties on inversion by the method proposed in this article could be further addressed by including it in the misfit weighting.

Finally, in the experimental tests, the phase velocity derivative was calculated by the gradient of the phase velocity and not by **Eq. 3.8** which uses the group velocity. The latter is indeed very difficult to evaluate in a robust way when the contrast between the two media is strong and implies a high velocity dispersion: in this case, the choice of the filter width is critical and beyond the scope of the present study. Therefore, we propose, for future studies, to analyze the impact of the velocities contrast on the choice of this filter and the values from which assessment of the phase velocity derivative is more interesting by calculating the phase velocity gradient.

## Acknowledgments

We would like to thank M. Wathelet, the co-developer of the *Geopsy* software. Our thanks are also extended to D. Pageot, G. Gugole and T. Devie for their help with the experimental measurements and data management. This work was co-funded by University Gustave Eiffel and the Région Pays de la Loire. Finally, we would like to thank J. Virieux for an informal discussion which gave birth to the idea of this innovative approach.

# Chapter 4

# Differential time-lapse inversion of surface waves phase velocity dispersion using the histogram distance between fundamental modes in dispersion diagrams

In this chapter, the notion of "differential inversion" is introduced in surface wave inversion for the purpose of monitoring the temporal variations of medium. We call it Differential Time-Lapse Surface Wave Inversion (DTLSWI). For the proposed approach, two types of dispersion data difference are tested and compared as inversion input data: the phase velocity difference and the phase velocity dispersion diagram distance. The former is the simple difference between two phase velocity dispersion curves, and the later is an innovative parameter for surface waves inversion, based on a statistical distance and considering the area of interest of the dispersion diagram as a histogram of phase velocity distributions. Both data differences are tested by numerical data and laboratory-measured data, based on two-layer models and compared with classical surface wave phase velocity dispersion curve inversion.

This chapter will be published in a few months as the second article associated to this thesis work. Thus, the presented structure follows this of a scientific article and may provide repetitions with previous chapters, particularly in some parts of the introduction.

## 4.1 Introduction

The monitoring of civil engineering structures and subsurface media is an important topic in current geophysical research. The variations of the medium properties due to the environmental changes, or the inner damages due to the

aging issue can potentially lead to collapsing phenomena. Among the non-destructive seismic approaches, surface waves are widely used, thanks to their high energy level and long propagation distances. We can cite, for example, applicated targets like, the inner erosion in earthen dams and levees (Planès et al., 2016), the velocity variations and attenuation due to the water infiltration in see dikes (Joubert et al., 2018), the water lever variation in granular media (Pasquet et al., 2016) and of shallow aquifers Pasquet et al. (2015a), and the ground water storage at mesoscale (Lecocq et al., 2017).

There are three steps in the standard procedure of surface wave methods, summarized as following. (1) Acquisition: the signal acquisition uses a series of receivers to capture the arriving signals, emitted from an active source (e.g. hammer) or a passive source (e.g. see waves). (2) Processing: the dispersion data is extracted from the acquisition recordings and will serve as the inversion input data, which could be the dispersion curve or the diagram of the phase velocity, generally used for subsurface investigations. (3) Inversion: the properties of the medium, which is usually a depth profile of shear-wave velocity, are inferred by solving an inverse problem.

The second step of the method mentioned above, considering a 1D layered medium for which the surface waves are dispersive, i.e. the phase velocity depends on frequency, aims to extract the dispersion relation for further understanding of the medium properties. By applying signal processing on the measured data, i.e. the seismogram in time-space domain, one extracts the dispersion relation of the medium from a dispersion diagram usually presented in frequency-velocity domain. The maximum amplitude of the dispersion diagram at a given frequency corresponds to the surface wave phase velocity ($V_{ph}$). For the third step of the method, the surface wave phase velocity ($V_{ph}$) is an input data classically used in the surface wave inversion process. The later looks for the model of which the theoretical dispersion curve is the closest to the measured one.

When inverting the surface wave phase velocity, the inversion can be performed on one mode, generally the fundamental mode which is dominent, or for several modes if they can be identified. However, the study of Zhang and Chan (2003) shows the difficulty of modes identification, the failure of which can lead to incorrect results. Moreover, in several cases, such as shear-wave velocity decreasing as function of depth or if there are strong shear-wave velocity contrasts, the dispersion curve consists in superimposed modes, also called "effective mode" (Tokimatsu et al., 1992). To overcome this problem, researchers have proposed different methods. Maraschini et al. (2010) propose to construct the Thomson-Haskell matrix using the searched model parameter and the observed dispersion curve. By minimizing the Thomson-Haskell matrix determinant, one could estimate the model parameter corresponding to the measurement, without the need of modes identification. However, in this approach, the presence of local minima is a major issue. Ryden and Park (2006) propose to invert the dispersion diagram by defining its misfit function involving the sum the each pixel in the diagram which demands a high computational cost. These studies and results show the interest of using the surface wave dispersion diagram as inversion input data. In this regards, we can note that for each frequency, the dispersion diagram forms a lobe with a particular shape which can be considered as a distribution of velocity. Some information is contained in this velocity distribution shape, for example, the width of lobes, the amplitude, the integrated

surface as function of velocity. Moreover, by using this part of the dispersion diagram, which will be called "principal lobe" hereafter, it is possible to avoid the noise contained in other parts of the diagram.

To take into account this information in the inversion process, we propose to consider the dispersion diagram lobes as a set of histograms and assess the histograms distance between measured and calculated data. Note that the approach of an alternative distance calculation for the inversion process was already conducted for other seismic data. For example, in the study of Engquist and Froese (2013), the conventinal misfit function, the $L2$ norm distance, is replaced by the Wasserstein distance, which is a mathematical tool widely used in optimal transport problems, for the comparison of 1D seismic signals. Then, Métivier et al. (2016) expanded this method for the entire seismogram comparison using a variant of the Wasserstein distance. As far as our proposal is concerned, the distances we implement come from the statistical domain, and concern the early approaches in Artificial Intelligence for image recognition.

Indeed, as the computer power has been rapidly growing in the recent decades, the machine intelligence is developed with high rapidity and widely applied in both scientific research and daily life. To teach a machine how to "think" like a human, one main task is the pattern recognition, which is "the study of how machines can observe the environment, learn to distinguish patterns of interest from their background, and make sound and reasonable decisions about the categories of the patterns" (Jain et al., 2000). One of the best approaches for pattern recognition is the statistical classification (Duda et al., 1973). Cha and Srihari (2002) introduced it to measure the distance between two histograms. In this study, we introduce the histogram distance to measure the difference between surface wave dispersion diagrams, which is called diagram distance.

In parallel to the issue of input data for inversion, the monitoring approach involves a key element: the sensitivity of the inverse method to variations, possibly weak, of the medium parameters. The current available approaches for surface waves and their key points are summarized below.

For the monitoring purpose, a series of measurements of the medium at different times can be used to estimate the temporal variations in the medium, which is called time-lapse monitoring (Arts et al., 2003; Bergamo et al., 2016; Planès et al., 2016). The dispersion data, extracted from the acquisition recording at the initial state, is called the baseline and the dispersion data recorded after a period of time is called the repeatline. When applying the inversion procedure on the baseline and the repeatline, one makes a time-lapse inversion (TLI), which is able to assess the medium properties' variation with time. The classical time-lapse inversion includes two independent inversions on the baseline and the repeatline, followed by the rebuilding of the medium properties.

Major concerns in the application of time lapse inversion are the indeterminacy of the inversion results themselves in the case of weak variations from one time step to another and the difficulty to make robust and informative inversion of two data sets with close information but with noise. Strategies have been implemented to overcome this problem in the context of monitoring underground reservoirs, using the Full Waveform Inversion method (FWI). Watanabe et al. (2004) proposed a differential method to invert the crosswell seismic data for reservoir monitoring during gas production tests, using FWI in the frequency domain. Instead of two independent inversions of the measured baseline and

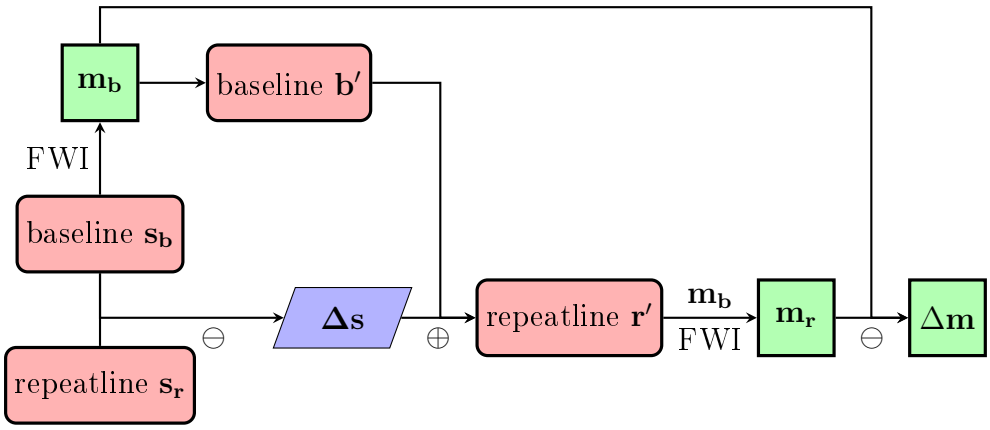


Figure 4.1: Workflow of Double Difference Full Waveform Inversion (DDFWI).

repeatline and the extraction of the model parameter variations from the subtraction of the inversion results, this differential method (1) uses the inversion result of the measured baseline to reconstruct a synthetic baseline; (2) adds the subtraction of the measured baseline and repeatline to the synthetic baseline in order to reconstruct a synthetic repeatline; (3) inverts the synthetic repeatline using the inversion result of the measured baseline as the initial model; (4) subtracts the inversion results of the measured baseline and repeatline to get the model parameter variations. This method is also called the Double Difference Inversion (DDI) and has been proved to produce more reliable estimation of the medium changes compared to the conventional FWI where two independent inversions are performed on the baseline and the repeatline data (e.g., Denli and Huang (2009); Zhang and Huang (2013); Yang et al. (2013); Zheng et al. (2011)). The workflow of the DDI method is presented in **Fig. 4.1**.

This approach has some non-operabilities in the context of the surface wave analysis using a global inversion technique. Actually, one advantage of the DDI is that the inversion of the repeatline uses the inversion result of the baseline as initial model, which is close to the true model of the repeatline, under the circumstances of weak variations between baseline and repeatline. However, this advantage disappears in the case of surface wave inversion with the global search algorithm as no initial model is used. Nevertheless, by subtracting the baseline and the repeatline, the synthetic repeatline contains the velocity variations caused by the model difference. Based on this idea, we propose to test a new method for inverting the surface waves temporal variations in a global research approach, which is the Differential Time-Lapse Surface Wave Inversion (DTLSWI).

Based on the description above, a new surface wave inversion algorithm is proposed in our study: the differential time-lapse surface wave inversion (DTLSWI), which uses the data difference between the baseline and repeatline as inversion input data. Two data difference are tested in this study for comparison: the $V_{ph}$ difference ($V_{ph}$-DTLSWI) and the diagram distance (DD-DTLSWI). To present this study and results, we first introduce the mathematical definition of histogram distance for better understanding of the diagram distance in the following. Then, two measurements gathers (on epoxy-resin models and mortar-

concrete slabs respectively) are presented with details for a better application and comprehension of the diagram distance. Finally, the DTLSWI approach is tested numerically and experimentally, using the synthetic data and the laboratory data respectively.

## 4.2 Histogram Distance

As proposed in introduction, the lobe shape of the fundamental mode in a dispersion diagram of surface wave data can be considered as a set of velocity distributions (one per frequency). A histogram is an approximate representation of a data distribution. Comparing two histograms, i.e. finding their similarity and difference, is an important subject in pattern classification and clustering. There are two methodologies to measure a histogram distance: the vector approach treats a histogram as a d-dimensional vector, such like *city-block* (*L1-norm*), *Euclidean* (*L2-norm*) and *correlation*, etc. (Pass et al., 1997), and the statistical approach regards the histogram as an empirical estimate of a probability density distribution (PDF) (Duda et al., 1973), for example Bhattacharyya distance (*B-distance*) (Kailath, 1967), Kullback-Leibler distance (*K-L distance*) (Kullback and Leibler, 1951).

In the study of Cha and Srihari (2002), the authors have compared the different approaches of histogram distances and mentioned that a disadvantage of the conventional methods of histogram distance calculation, is that the similarity between histograms is not taken into account. To overcome this disadvantage, Cha and Srihari propose a new method to measure the distance between ordinal type histograms, i.e. the data described by the histograms are numbers, such like ages, lengths, velocities, etc. It can be used in the study of the surface wave velocity, to make a comparison between two dispersion diagrams. Thus, we recall below the formulations of the six different ways mentioned above for calculating these distances between histograms which will be tested for DD-DTLSWI in the following parts.

We use the following notations and symbols to define a histogram. A set $X$ contains $q$ elements: $X = \{x_0, x_1, ..., x_i, ..., x_{q-1}\}$, and each element $x_i$ is a measurement. Consider a set of $r$ elements $A$ where $A = \{a_0, a_1, ..., a_j, ..., a_{r-1}\}$ and $a_j \in X$. The histogram of the set $A$ along the measurement $x_i$ is then

$$H_i(A) = \sum_{j=0}^{r-1} \delta_{ij} \quad where\ \delta_{ij} = \begin{cases} 1 & if\ a_j = x_i\,, \\ 0 & otherwise. \end{cases} \tag{4.1}$$

When a histogram is considered as a vector, the standard vector norms can be used to measure the histogram distance as follows:

$L_1$ norm:

$$D_{L1}(A, B) = \sum_{i=0}^{q-1} |H_i(A) - H_i(B)|. \tag{4.2}$$

$L_2$ norm:

$$D_{L2}(A, B) = \sqrt{\sum_{i=0}^{q-1} (H_i(A) - H_i(B))^2}. \tag{4.3}$$

Table 4.1: Number of students at each height range. $165\,cm$ represents the height range $[164.5, 165.5]\,cm$, same for the rest of height ranges.

| height | 165 | 166 | 167 | 168 | 169 | 170 | 171 | 172 | 173 | 174 |
|---|---|---|---|---|---|---|---|---|---|---|
| H(A) | 10 | 8 | 7 | 5 | 2 | 1 | 1 | 1 | 4 | 2 |
| H(B) | 8 | 7 | 3 | 5 | 2 | 1 | 1 | 3 | 4 | 7 |

Another approach to measure the histogram distance is to compute the correlation, which can gives the degree to which two sets of measurement are linearly related:

$$D_{corr}(A,B) = \frac{E[(H(A) - \overline{H(A)})(H(B) - \overline{H(B)})]}{\sigma_A \sigma_B}, \tag{4.4}$$

where $E[\cdot]$ is the expected value operator, $\overline{H(\cdot)}$ is the mean value of the histogram and $\sigma_A$, $\sigma_B$ are the standard deviations which are defined as

$$\sigma_A = \sqrt{\frac{1}{q}\sum_{i=0}^{q-1}(H_i(A) - \overline{H(A)})^2}, \quad \sigma_B = \sqrt{\frac{1}{q}\sum_{i=0}^{q-1}(H_i(B) - \overline{H(B)})^2} \tag{4.5}$$

In the probability point of view, the histogram distance can be considered as the overlap between two distributions. Here we define the probability density function as follows:

$$P_i(A) = \frac{H_i(A)}{\sum_{i=0}^{q-1} H_i(A)}. \tag{4.6}$$

The *B-distance* measures the similarity between two probability distributions (Kailath, 1967) and its formulation is

$$D_{Bha}(A,B) = -log \sum_{i=0}^{q-1} \sqrt{P_i(A)P_i(B)}. \tag{4.7}$$

Another famous approach is the *K-L distance* which generalized Shannon's concept of entropy (Kullback and Leibler, 1951; Shore and Gray, 1982)

$$D_{KL}(A,B) = \sum_{i=0}^{q-1} P_i(B) log \frac{P_i(B)}{P_i(A)}. \tag{4.8}$$

However, the common disadvantage of those distances is that, either the similarity (the overlapping part of two distributions) or the difference (the vector norms) is used to measure the histogram distance. Indeed, an efficient comparison of two histograms should contain information of both the similarity and the difference. For this reason, Cha and Srihari have introduced a new measure of histogram distance, using the notion of the *minimum difference of pair assignments* that will be used in this study:

$$D_{ord}(A,B) = \sum_{i=0}^{q-1} \mid \sum_{j=0}^{i} (H_j(A) - H_j(B)) \mid . \tag{4.9}$$

As an illustration of the principle, an example is given in **Table 4.1**. **Fig. 4.2** shows the histograms $H(A)$ (red bars) and $H(B)$ (blue bars), assuming that

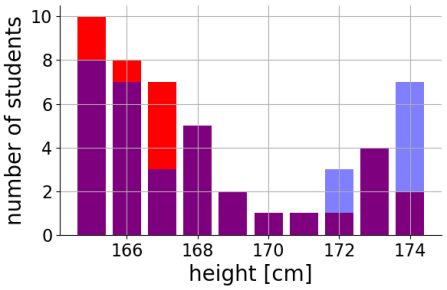


Figure 4.2: Example of histograms $H(A)$ (red bars) and $H(B)$ (blue bars), representing the number of students in each height class. The purple bars are the overlapping parts of $H(A)$ and $H(B)$.

the height of two groups (A and B) of students is measured and presenting the number of student respectively by two histograms $H(A)$ and $H(B)$ in the total range $[164.5, 174.5]\,cm$. The purple bars are the overlapping parts of $H(A)$ and $H(B)$, i.e. the equal number of students for each height class which is contained in both groups A and B.

Using the histogram distances defined above, the histogram distances of $H(A)$ and $H(B)$ are calculated as follows: $D_{L1}(A,B) = 14$, $D_{L2}(A,B) = 7.07$, $D_{corr}(A,B) = 0.70$, $D_{Bha}(A,B) = 0.016$, $D_{KL}(A,B) = 0.072$, $D_{ord}(A,B) = 50$. It is difficult to tell which histogram distance(s) is (are) the best by simply comparing these values. In section 4, those histogram distances will be applied for comparing two surface wave dispersion diagrams, where the advantages and limits of each distance can be shown more clearly. In section 5, the DD-DTLSWI, which uses the diagram distances as inversion input data, will be applied on numerical data and laboratory data, in order to test the feasibility of the use of diagram distance for the surface wave inversion.

## 4.3 Measured data

Two sets of laboratory ultrasonic measurements are presented in this section, which will be used to test the DTLSWI approach. The first one is carried out on four two-layer epoxy-resin models. These blocks are made for simulating natural subsurface media at reduced scale. The shallow layer is similar for each of them whereas the deep layer presents specific S-waves velocity for each one. The second measurements are recorded on three two-layer slabs consisting of a mortar layer on a concrete slab, where variations occur in the shallow layer (mortar). The specification of the models and data are summarized below. Note that in case of the mortar-concrete slabs, internal non-homogeneity may occur. Thus more cares are taken when processing the mortar-concrete slabs data and the details will be given in the following.

### 4.3.1 Epoxy-resin models

Four reduced-scale models made of epoxy-resin (see **Fig. A.1** in Appendix A) have been designed in order to physically simulate a series of successive

Table 4.2: $C0$ model parameters and dimensions. $h_i$: layer thickness; $l$ and $w$: length and width of model. Scale ratio between the numerical and the experimental model dimensions is 1000. A photo of one epoxy-resin model is shown on **Fig. A.1** in Appendix A.

| layer | $V_{p_i}$ $[m/s]$ | $V_{s_i}$ $[m/s]$ | $\rho_i$ $[kg/m^3]$ | $\nu_i$ | $h_i$ $[mm]$ | l $[mm]$ | w $[mm]$ |
|---|---|---|---|---|---|---|---|
| 1 | 1300 | 703 | 450 | 0.29 | 7.2 | 265 | 235 |
| 2 | 2048 | 933 | 1300 | 0.37 | 203 | 265 | 235 |

measurements in a variable medium. The parameters $m$ (compressional-wave velocity $V_p$, shear-wave velocity $V_s$, density $\rho$ and layer thickness $h$) and the dimensions of the first model (named $C0$) are given in **Table 4.2**. To minimize and delay the boundary effects, the size of model has been optimized and the edges of the models are rounded using a radius larger than or equal to the central wavelength (Pageot et al., 2015). The radius of the rounded edges is $12\,mm$ for all the epoxy-resin models. Besides, the scale ratio between the numerical and experimental model dimensions is 1000, i.e. $1\,m$ in the numerical model is $1\,mm$ in the laboratory model, and $1\,Hz$ corresponds to $1\,kHz$ (Pageot et al., 2017).

The three other models are respectively called $C25$, $C45$ and $C65$, which are similar in shape to the $C0$ model. The shear-wave velocities of the deep layer of $C25$, $C45$ and $C65$ models are respectively $990\,m/s$, $1038\,m/s$ and $1086\,m/s$. We introduce here the variation ratio $\alpha(V_{s_i}, X, Y)$ to describe the change of shear-wave velocity $V_{s_i}$ of model $Y$ in the $i$-th layer, with respect to the $X$ model:

$$\alpha(V_{s_i}, X, Y) = \frac{V_{s_i}(Y) - V_{s_i}(X)}{V_{s_i}(X)}. \tag{4.10}$$

Substituting $X$ by $C0$ and $Y$ by $C25$, $C45$ and $C65$, the corresponding variation ratios of the deep layer are 6%, 12% and 17%.

The measurements recorded on the epoxy-resin models have been conducted in the MUSC (Measurement at Ultrasonic SCale) laboratory which makes it possible to carry out seismic analogical measurements at reduced scale. A Ricker wavelet with a central frequency of $100\,kHz$ was generated with a dry contact point piezoelectric transducer and the signals were recorded with a moving laser interferometer, with a sampling rate equal to $10\,MHz$ (see **Fig. A.1 (a)** in Appendix A for an illustration of the experimental set-up). **Fig. A.1 (b)** in Appendix A shows the position of the piezo-electric source and the measurement points of the laser receivers. The receivers distances to the source position are $x \in [12, 102]\,mm$ with a receiver spacing of $1\,mm$ for the experimentation conducted in this study. More specifications of the MUSC measurement bench are available in Bretaudeau et al. (2011). Like all the recordings published from the MUSC bench, the measurements are available to the scientific community and can be obtained as free data on request by email.

The measured seismograms for the four models are presented in **Fig. A.2** in Appendix A. To see the difference, the seismograms are superimposed and zoomed in the zone $t \in [0.1, 0.3]\,ms$ and $x \in [92, 101]\,mm$. We note the very slight differences between two successive data-sets carried out on models with close velocities. The phase velocity dispersion diagrams (**Fig. 4.3, (a)** to **(d)**) are then extracted from the measured seismograms, using the phase-difference processing method (Park et al., 1998, 1999; Mokhtar et al., 1988). The dis-

Table 4.3: The parameters and dimensions of mortar-concrete slabs $D01$, $D06$ and $D08$. w/c is the water-to-cement ratio of the mortar layer. $h$, $l$, and $w$ are the thickness, the length and the width of the layers and slabs.

The parameters and dimensions of the slab $D01$.

| layer | w/c | $V_p$ $[m/s]$ | $\rho$ $[kg/m^3]$ | $h$ $[m]$ | $l$ $[m]$ | $w$ $[m]$ |
|---|---|---|---|---|---|---|
| mortar | 0.40 | 3660 | 2100 | 0.03 | 1.2 | 0.8 |
| concrete | - | 4300 | 2400 | 0.2 | 1.2 | 0.8 |

The parameters and dimensions of the slab $D06$.

| layer | w/c | $V_p$ $[m/s]$ | $\rho$ $[kg/m^3]$ | $h$ $[m]$ | $l$ $[m]$ | $w$ $[m]$ |
|---|---|---|---|---|---|---|
| mortar | 0.55 | 3150 | 2000 | 0.03 | 1.2 | 0.8 |
| concrete | - | 4300 | 2400 | 0.2 | 1.2 | 0.8 |

The parameters and dimensions of the slab $D08$.

| layer | w/c | $V_p$ $[m/s]$ | $\rho$ $[kg/m^3]$ | $h$ $[m]$ | $l$ $[m]$ | $w$ $[m]$ |
|---|---|---|---|---|---|---|
| mortar | 0.70 | 2642 | 1870 | 0.03 | 1.2 | 0.8 |
| concrete | - | 4300 | 2400 | 0.2 | 1.2 | 0.8 |

persion diagrams are calculated in the frequency range $[20, 150]\,kHz$ in order to visualize the fundamental mode and the first higher mode for all epoxy-resin models. At each frequency, the phase velocity is limited in the velocity range $[500, 1100]\,m/s$ with the resolution $1\,m/s$. Black dots in each diagram correspond to the maximum amplitude at each frequency, i.e. the picked phase velocity dispersion curve. Red dots show the limits of the principal lobe where the energy is most contributing (the limits of principal lobe are calculated analytically using **Eq. 4.19** as explained in section 4.1). The normalized amplitude of diagram at frequency $f = 45\,Hz$ and $f = 85\,Hz$ are presented in **Fig. 4.3, (e)** and **(f)**, as function of velocity.

### 4.3.2 Mortar-concrete slabs

Three mortar-concrete slabs are used and each slab is made by a layer of mortar, superimposed on the surface of a concrete slab. The mortar layers of the three slabs have different water-to-cement ratio (w/c) which changes the mechanical properties of each slab. The parameters and the dimensions of the slabs are given in **Table 4.3**. The compressional-wave velocities of mortar layers are determined using the seismic refraction method (Press et al., 1954; Palmer, 1981).

The experimental set-up is made by an ultrasonic source and a receiver probe of 16 receivers. For the measurement of each slab, four sources ($54\,kHz$, $100\,kHz$, $ACS1$ and $ACS234$, see **Fig. B.2** in Appendix B) are used separately in order to average the response of the sensors and improve the signal-to-noise ratio. For each measurements, the probe is reinstalled five times in a row to have 80 traces in total. The sampling rate is equal to $5\,MHz$.

The dispersion diagrams are extracted using the phase-difference processing method, with $f \in [5, 80]\,kHz$ and $v \in [1300, 2700]\,m/s$ (velocity resolution equals to $2\,m/s$). The final dispersion diagrams and the dispersion curves of

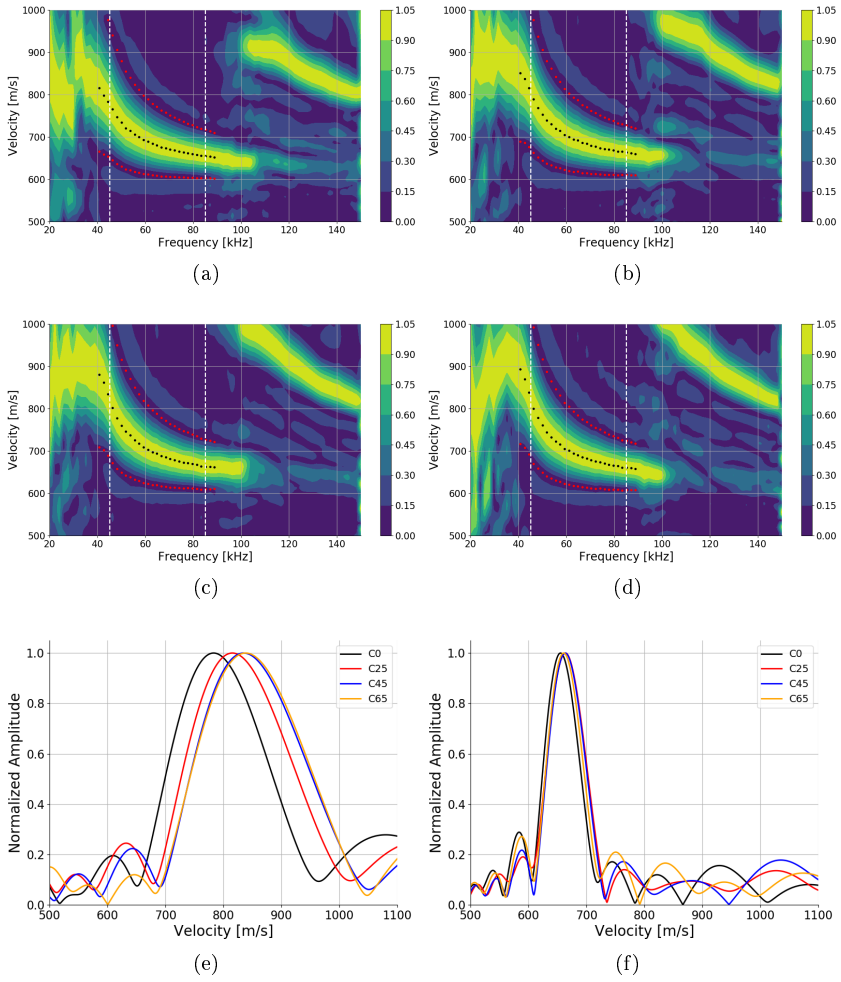


Figure 4.3: Dispersion diagrams for the epoxy-resin model (a) $C0$, (b) $C25$, (c) $C45$ and (d) $C65$. Dispersion curves (black dots) and the the limits of the principal lobe (red dots) are presented in the frequency range $[40, 90]\,kHz$ that will be used in the inversion (see section 5.2 for more details). The white lines in diagrams at $f = 45\,Hz$ and $f = 85\,Hz$ correspond respectively to the phase velocity distributions in (e) and (f).

each slab are obtained after averaging the measured diagrams using the four sources. The dispersion diagrams are picked manually at certain frequencies due to the lack of energy of the source. The dispersion curves of each slab using the four sources and the final dispersion curve after manual picking are available in **Fig. B.3** In Appendix B. The final dispersion diagrams and the dispersion curves are presented in **Fig. 4.4**.

## 4.4 Diagram Distance

The inversion methodology proposed in this article is based on two innovative aspects: firstly by using an innovative distance for calculating differences between parts of dispersion diagrams and secondly by inverting this difference itself thus carrying out a differential inversion process. Concerning the calculation of the difference between calculated or measured data, we propose to use a distance of two dispersion diagrams by assimilating the velocity lobes as histograms of velocity distribution for each frequency taken into account. The difference between these histograms, called here the phase velocity diagram distance (or diagram distance) is based on a statistical distance. Several of them, which will be tested in this study, have been presented previously (section 2). In order to further describe the principle of this approach, we summarize below the computational method used to compute the dispersion diagram and the way we extract part of the information of interest for the study, i.e. the velocity lobe corresponding to the fundamental mode. Finally, we examine the evolution of these lobe distances in the case of laboratory measurements on epoxy-resin blocks presented above.

There are several processing methods to extract the dispersion diagram from a multi-receiver seismogram, such as the $f-k$ method (Yilmaz, 1987), the $\tau-p$ transform (McMechan and Yedlin, 1981), the phase-difference method (Mokhtar et al., 1988; Park et al., 1998) and the linear Randon transformation (Luo et al., 2008). Among them, the phase-difference method extracts the dispersion diagram by, firstly, a 1D Fourier Transform to have amplitude spectrum at each offset, then, an integration of normalized amplitude as function of the offset to have a frequency-velocity spectrum. The diagrams presented in this article are extracted using this method as it provides a high spectrum resolution of the dispersion diagram with an optimized number of receivers (Park et al., 1999; Xia, 2014; Socco et al., 2010).

As previously mentioned, only an optimal comparison zone is used: the principal lobe of the diagram where surface wave energy concentrates. Thus, noise occurring in other parts of the diagram is avoided. This strategy makes the inversion more robust in case of monitoring. Moreover, note that in our study, only the fundamental mode is taken into account even if further studies will be planned to tackle information included in the lobes of higher modes.

### 4.4.1 Zone of comparison: Principal lobe calculation

When using the phase-shift method (Park et al., 1998) to extract the dispersion diagram of surface wave phase velocity, one can obtain the width of the lobes, among which, the principal lobe contains the most part of the energy. A set of receivers are used to record the particle movement and the recorded signal

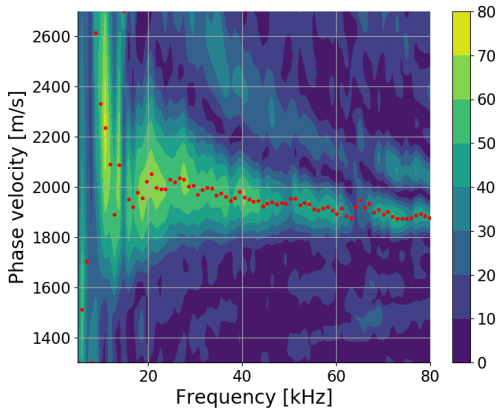


(a)

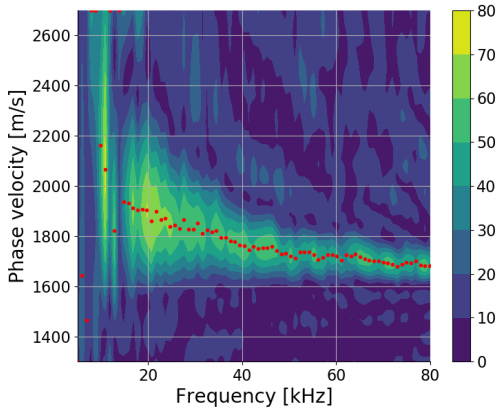


(b)

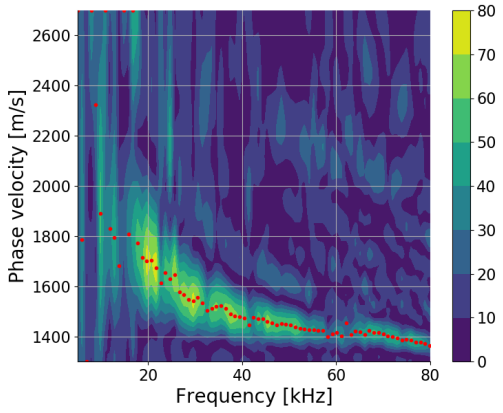


(c)

Figure 4.4: The dispersion diagrams of slab D01 (a), D06 (b) and D08(c). The red dots present the dispersion curve of each slab.

is a seismogram in time-offset domain, noted as $s(t,x)$. Applying 1D Fourier transform, one gets the spectrum in frequency-offset domain:

$$S(f,x) = \int_t s(t,x)e^{j2\pi ft}dt. \tag{4.11}$$

Supposing that the source signal at position $x = 0$ can be written as $R(f) = A(f)e^{-j\phi(f)}$ with $A(f)$ and $\phi(f)$ the corresponding amplitude and phase, as function of frequency. When the surface wave is propagating in an elastic medium, after a propagation distance $x$, the recorded signal is

$$S(f,x) = A(f)e^{-j\phi(f)}e^{-j2\pi f\frac{x}{V_{ph}}} \tag{4.12}$$

with $V_{ph}$ the surface wave velocity at frequency $f$. The phase-difference method (Park et al., 1998) calculates dispersion diagram as follows:

$$D(f,v) = \int_x \frac{S(f,x)}{|S(f,x)|}e^{j2\pi f\frac{x}{v}}dx. \tag{4.13}$$

Substituting **Eq. 4.12** in **Eq. 4.13**, one can write

$$D(f,v) = e^{-j\phi(f)}\int_x e^{j2\pi f(\frac{x}{v}-\frac{x}{V_{ph}})}dx. \tag{4.14}$$

The width of lobes of the diagram $D(f,v)$ corresponds to velocities $v$ for which $D(f,v) = 0$. Thus, values of $v$ must verify:

$$\int_x e^{j2\pi f(\frac{x}{v}-\frac{x}{V_{ph}})}dx = 0. \tag{4.15}$$

Assuming that the receivers are organized in the space vector $x \in [x_{begin}, x_{end}]$, **Eq. 4.15** implies:

$$\frac{1}{j2\pi f(\frac{1}{v}-\frac{1}{V_f})}\left[e^{j2\pi f(\frac{1}{v}-\frac{1}{V_{ph}})x}\right]_{x_{begin}}^{x_{end}} = 0, \tag{4.16}$$

$$2\pi f(\frac{1}{v}-\frac{1}{V_{ph}})(x_{end}-x_{begin}) = 2n\pi, \quad n \neq 0, \tag{4.17}$$

which can also be written as:

$$\frac{1}{v} = \frac{1}{V_{ph}} + \frac{n}{f(x_{end}-x_{begin})}, \quad n \neq 0. \tag{4.18}$$

The velocity can then be deduced using **Eq. 4.18**

$$v_n = \frac{1}{\frac{1}{V_{ph}} + \frac{n}{f(x_{end}-x_{begin})}}, \quad n \neq 0. \tag{4.19}$$

In **Eq. 4.19**, when $n \leq 0$, $v_n$ corresponds to the limits of the lateral lobes on the right hand-side of the principal lobe; when $n \geq 0$, $v_n$ is the limits of the lateral lobes on the left hand-side. The limits of the principal lobe used hereafter are obtained when $n = \pm 1$ ($v_{-1}$ and $v_{+1}$).

**Eq. 4.19** indicates that the width of the lobe is dependent on the receiver array length. A longer length leads to a smaller lobe width, i.e. a better

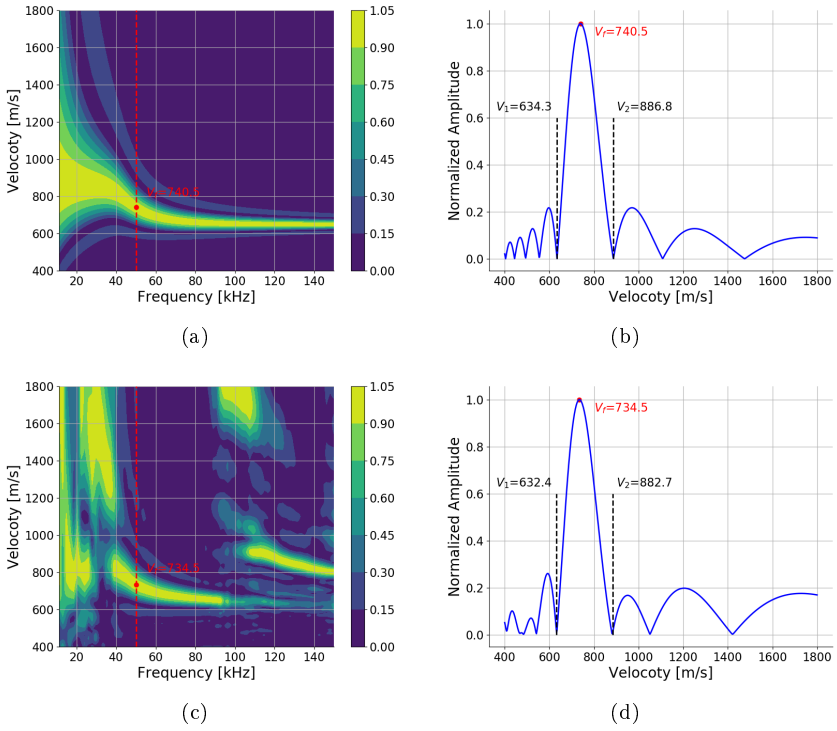


Figure 4.5: Numerical (a) and experimental (c) dispersion diagrams and the velocity distribution (b) and (d) at $f = 50Hz$. The medium parameters of the numerical dispersion diagram are presented in **Table 4.2** and the experimental dispersion diagram is that of the epoxy-resin model C0. The receiver array length ($= x_{end} - x_{begin}$) is $89\,mm$. The limits of first lobes are presented as the dotted line in (b) and (d) of which the values can be verified by **Eq. 4.19** for $n = \pm 1$.

resolution of the dispersion diagram. In fact, when $n = 0$, $v = V_f$, which corresponds to the position of the maximum value of the dispersion diagram.

The principal lobe analytical limits(i.e. $v_{-1}$ and $v_{+1}$) are calculated for illustrative tests in **Fig. 4.5**, with both numerical and experimental diagrams. The experimental diagrams come from the reduced-scale two-layer model $C0$ introduced in Section 3.1. The associated numerical model uses the medium parameters presented in **Table 4.5** and reproduces the experimental set-up of the model $C0$ in order to generate comparable numerical data. At $f = 50\,kHz$, the corresponding phase velocity of numerical and experimental models are respectively $740.5\,m/s$ and $734.5\,m/s$. Taking these values as $V_f$ and $n = \pm 1$ in **Eq. 4.19**, one can recover the limits of the principal lobes of these two diagrams which are presented in **Fig. 4.5 (b)** and **(d)**.

It should be pointed out that only the principal lobe of the diagram is used as a comparison zone because it is the most energetic part of the diagram and it eliminates the lack of energy issue at lateral lobes. However, **Eq. 4.19** is not validated when multiple modes appear at high frequencies. In this case, one could choose, instead of one part of the velocity distribution (the principal lobe),

the total velocity distribution which includes all the modes as the comparison zone. This complexity is beyond the scope of this paper.

### 4.4.2 Diagram distance of epoxy-resin model data

Considering the principal lobe of the dispersion diagram as a set of histograms of the velocity distributions (i.e. one for each frequency), we can apply the statistical distances described in section 2 for assessing the difference between two dispersion diagrams as a function of frequency:

$$DD(A, B, f) = D_{type}(D(A, f), D(B, f)). \tag{4.20}$$

$DD(A, B, f)$ is the diagram distance of two diagrams $D(A, f)$ and $D(B, f)$, with $D(A, f)$ and $D(B, f)$ being the velocity distributions of two dispersion diagrams $A$ and $B$, at frequency $f$. $D_{type}$ is the histogram distance, where the subscript "type" indicates the type of statistical distance used among those introduced in Section 2 ($D_{L1}$, $D_{L2}$, $D_{corr}$, $D_{Bha}$, $D_{KL}$, $D_{ord}$).

The diagram distances of the epoxy-resin models in Section 3.1 are therefore calculated, using the principal lobe only. Before calculating the distance of two diagrams, it should be clarified that, in order to consider the velocity distribution as an histogram and to make possible comparison between two of them, the velocity distribution, considered as an histogram, is normalized so that the total surface of each principal lobe equals to 1 (see Appendix C **Fig. C.2 (b)**).

As described in section 3, the differences between the properties of epoxy-resin models concern only the deep layer; the shallow layer remains similar in all models. This feature indicates that the differences are expected for the lower frequencies, that is, we expect a greater distance at low frequencies and a smaller distance at high frequencies. **Fig. 4.6 (a)** presents the diagram distances of the epoxy-resin models $C0$ and $C25$. Taking into account the feature expected for higher and lower frequencies, the curves shapes show that the *L1-norm* and the *L2-norm* distances do not well provide information about the expected similarity at high frequencies. The *B-distance* and the *correlation* also show slightly larger deviations for higher frequencies. The *K-L distance* shows a decay curve but the *ordinal type distance* seems a priori the best way to indicate similarity for higher frequencies compared to lower frequencies because the decay is the strongest.

In order to confirm this feature we assess the effects of the several distances on a misfit value used in the inversion process. For that, a series of synthetic diagrams (names $\widetilde{Cx}$) are then generated, based on the baseline $C0$ parameters as well as the experimental set-up, for the variation ratio $\alpha(V_{s_2}, C0, \widetilde{Cx}) \in [0, 20]\%$. The distances of the synthetic diagrams and the measured diagram of $C0$ are calculated using **Eq. 4.20** and named $DD(C0, \widetilde{Cx}, f)$. Here, we introduce a $L_2$ norm objective (or misfit) function to estimate the difference between the measured and synthetic dispersion distances:

$$misfit = \sqrt{\frac{1}{N_f} \sum_f (DD(C0, C25, f) - DD(C0, \widetilde{Cx}, f))^2} \tag{4.21}$$

with $N_f$ the number of data in the frequency domain and $DD(C0, C25, f)$ the measured diagram distance of the measured diagrams of $C0$ and $C25$. We use

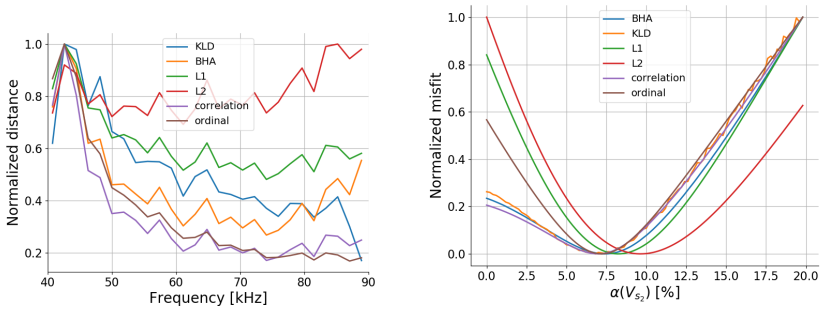


(a) (b)

Figure 4.6: (a) Diagram distances of models $C0$ and $C25$, normalized by the maximum values. (b) Normalized misfit values between the distances of measured data ($C0$ and $C25$) and a series of synthetic diagrams.

the exponential function in order to have the misfit values ranged in $[0, 1]$:

$$P = exp(-misfit). \tag{4.22}$$

The misfit values are presented in **Fig. 4.6 (b)**, as function of $\alpha(V_{s_2}, C0, \widetilde{Cx})$. The behaviors of the misfit evolution for the different distances show that the *L1-norm* and the *L2-norm* distances have biased $\alpha(V_{s_2}, C0, C25)$ values because the minimum misfit values are between 7.5% and 10% whereas the actual discrepancy between $V_{s_2}$ in $C0$ and $C25$ models is 6%. The *correlation*, the *B-distance* and the *K-L distance* can estimate the actual variation between the two models, but the *ordinal type distance* can not only estimate the variation between $C0$ and $C25$, but also has bigger misfit values when $\alpha(V_{s_2}, C0, C25) < 5\%$. This means the *ordinal type distance* better discriminates the differences between $DD(C0, \widetilde{Cx}, f)$ and $DD(C0, C25, f)$. Thus it will be able to find the best result more efficiently in an inversion process because presenting the misfit values as function of $\alpha(V_{s_2}, C0, \widetilde{Cx})$ is a simplified inversion process: the model parameter $V_{s_2}$ varies linearly in a given range and the calculated diagram distances are compared with the measured diagram distance. In the following section, the new inversion process for monitoring purpose based on this statistical distance, i.e. ordinal type distance, applied on the principal lobe will be numerically and experimentally tested, using the laboratory data presented in section 3.

## 4.5 Time-lapse surface wave inversion

The objective of time-lapse inversion is to find out the variation of the medium. Classically, one would invert the measured data, baseline and repeatline, separately, then the variation would be extracted by calculating the difference between the inversion results. The innovate point of our approach is to use the difference between baseline and repeatline as inversion input data. The workflow of the process is presented in **Fig. 4.7**. The baseline $\mathbf{b}$ is the measured data at time $t_0$. The repeatline $\mathbf{r}$ is another measurement at time $t_1$. $\mathbf{Diff}(\mathbf{b}, \mathbf{r})$ is the difference between the baseline and the repeatline, which is the inversion

input data. $\mathbf{b}'$ and $\mathbf{r}'$ are the estimated data associated to the searched models for the baseline and the repeatline.

With $\mathbf{m}$ representing the model parameters, the searched model in the inversion, $\mathbf{m}'$, is modified at each iteration. It is used to calculate the synthetic repeatline $\mathbf{r}'$. The baseline $\mathbf{b}'$ can be synthetic, calculated with parameters inverted from measurement $\mathbf{b}$, or directly the measured data, i.e. equal to $\mathbf{b}$. Since the $\mathbf{Diff}(\mathbf{b}', \mathbf{r}')$ is the inversion input data, its calculation is the most important part in the inversion process. Using a synthetic $\mathbf{b}'$ ensures that the difference between $\mathbf{b}'$ and $\mathbf{r}'$ depends only on the variation of the models. Other effects, such as the noise and the attenuation, are under control and can be eliminated. But if the synthetic baseline is not close enough to the measured baseline, i.e. if the first inversion of $\mathbf{b}$ is not accurate enough for providing parameters to calculate $\mathbf{b}'$ , it can bias the differential inversion results. To avoid the issue of biased inversion results of $\mathbf{b}$, we use the measured instead of synthetic baseline in the inversion process, i.e. $\mathbf{b}' = \mathbf{b}$.

One of inversion input data, which is tested in this study for comparison to the diagram distance, is the $V_{ph}$ difference. The $V_{ph}$ difference is the simple difference between the phase velocity of the baseline and the repeatline as

$$D_{vph}(b, r, f) = V_{ph}^{b}(f) - V_{ph}^{r}(f). \tag{4.23}$$

The differential time-lapse surface wave inversion using $D_{vph}$ as inversion input data will be abbreviated as "$V_{ph}$-DTLSWI" in the following.

The other tested inversion input data is the diagram distance with the ordinal type distance, which is introduced in section 4.2 (**Eq. 4.20**). We should note that the definition of the ordinal type distance (**Eq. 4.9**) has a reciprocal property, which can be expressed as

$$D_{ord}(A, B) = D_{ord}(B, A). \tag{4.24}$$

It is unconvenient to use directly this formulation since the increase or the decrease of the surface wave velocity at one given frequency has a major physical meaning (see Appendix C **Fig. C.1 (c)** and **(d)**). To circumvent this difficulty, we propose a slightly alternative definition of the ordinal type histogram distance, where the absolute value of the cumulative summation is removed:

$$D'_{ord}(A, B) = \sum_{i=0}^{q-1} \sum_{j=0}^{i} (H_j(A) - H_j(B)). \tag{4.25}$$

The reciprocal property of the ordinal type histogram distance has vanished. This prevents the bias of the inversion results. Indeed with **Eq. 4.25**, the sense of variation of the phase velocity between the baseline and the repeatline is correctly taken into account in the inversion process. The DTLSWI using diagram distance as inversion input data will be called as "DD-DTLSWI" in the following.

The inversion method used in this study is the Neighborhood Algorithm (NA), which makes use of Voronoi cells to compute the misfit function in the parameter space, where the pseudo-random samples are generated at each iteration and then guided and improved by the samples generated at the previous iteration (Sambridge, 1999b; Wathelet, 2008).

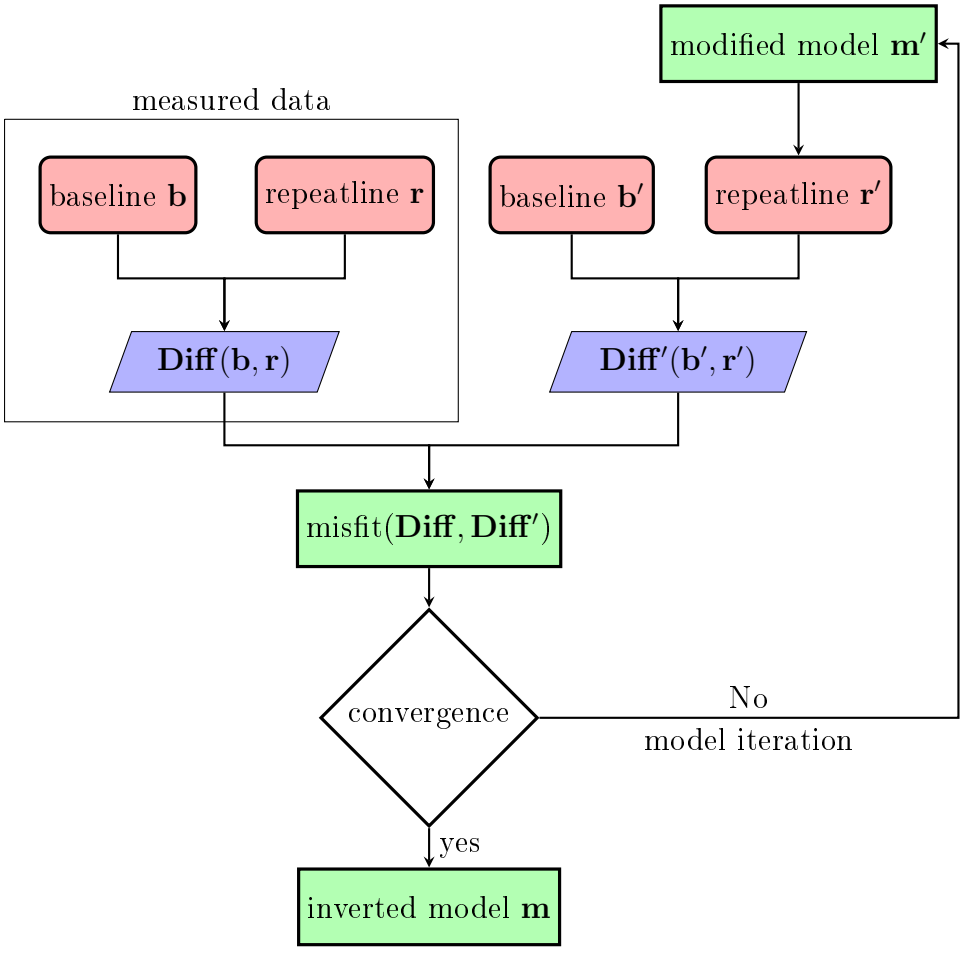


Figure 4.7: Work-flow of differential time-lapse surface wave inversion (TL-SWI). Baseline and repeatline ($\mathbf{b}$ and $\mathbf{r}$ respectively) are the measured data of a medium at different time. The $\mathbf{Diff}(\mathbf{b},\mathbf{r})$ is the difference between two data-sets which can be replaced by $D_{vph}(b,r,f)$ (**Eq. 4.23**) or $DD(b,r,f)$ (**Eq. 4.20**). $\mathbf{b}'$ and $\mathbf{r}'$ are the estimated data associated to the searched models for the baseline and the repeatline.

Table 4.4: Baseline model parameters for the numerical tests.

| layer | $V_{p_i}$ $[m/s]$ | $V_{s_i}$ $[m/s]$ | $\rho_i$ $[kg/m^3]$ | $\nu_i$ | $h_i$ $[m]$ |
|---|---|---|---|---|---|
| 1 | 1300 | 709 | 450 | 0.29 | 7.2 |
| 2 | 2048 | 938 | 1300 | 0.37 | $\infty$ |

### 4.5.1 Numerical Tests of the DTLSWI

To verify the feasibility of DTLSWI, several numerical tests are performed. The inversion results are compared with the classical surface wave phase velocity inversion (abbreviated as $V_{ph}$-SWI), as described in the introduction. The baseline is a two-layer medium, with a layer superimposed on a semi-infinite medium. The model parameters of the baseline in given in **Table 4.4**. Four repeatlines are considered: the deep layer shear-wave velocity $V_{s_2}$ increases and the variation ratios $\alpha(V_{s_2}, b, r)$ (**Eq. 4.10**) are respectively equal to 1%, 3%, 5%, 10% and 15%.

The theoretical dispersion curves are used in the $V_{ph}$-SWI and the $V_{ph}$-DTLSWI. The synthetic seismograms are calculated using the theoretical dispersion curve of the phase velocity of the medium under consideration. Here we reproduce the measurement's set-up used in laboratory MUSC for the epoxy-resin models (section 3.1). The resulting seismogram is used to extract the synthetic dispersion diagram for DD-DTLSWI. We should remind that only the fundamental mode is taken into account.

The synthetic dispersion diagrams are then calculated using the phase-shift method in the velocity range $[500, 1300]\, m/s$ with the velocity resolution equal to $1\, m/s$, and in the frequency range $[30, 150]\, Hz$. The same frequency range is used to calculate the theoretical dispersion curves which will be used in the $V_{ph}$-SWI and the $V_{ph}$-DTLSWI.

As we mentioned in the beginning of section 5, the NA is used in the inversion, for which, several tuning parameters are needed: $n_{s_0} = 50$ the number of samples randomly distributed in the parameter space as well as the Voronoi cells number at the initial iteration; $n_r = 10$ the number of best cells to consider for the next iteration; $n_s = 10$ the number of new generating samples at each selected cell; and $n_i = 10$ the total number of iteration. Finally, a total of $1050 (= n_{s_0} + n_r \times n_s \times n_i)$ models are searched in each inversion.

In these inversion tests, we fix $V_p$ and $\rho$ of each layer and invert the shear-wave velocities $V_{s_i}$ of the two layers and the thickness of the first layer $h_1$. $V_{s_1}$ is searched in the range $[500, 900]\, m/s$, $V_{s_2}$ in the range $[900, 1300]\, m/s$ and the thickness in the range $[7.0, 7.5]\, m$.

**Fig. 4.8 (a)** presents the convergence curves of $V_{ph}$ inversion, $V_{ph}$-DTLSWI inversion and DD-DTLSWI, for the model $C25$. The misfit value at each iteration is calculated using the **Eq. 4.22**. Since the misfit function is used two different data (phase velocity or histogram distance at each frequency), the original values of misfit are not directly comparable. In **Fig. 4.8 (b)**, the misfit values of each curve are normalized as follows:

$$P_n = \frac{P_o - min(P_o)}{max(P_o) - min(P_o)}. \tag{4.26}$$

$P_o$ is the original misfit value calculated for each searched model using **Eq. 4.22** (**Fig. 4.8 (a)**) and $P_n$ is the normalized misfit value (**Fig. 4.8 (b)**).

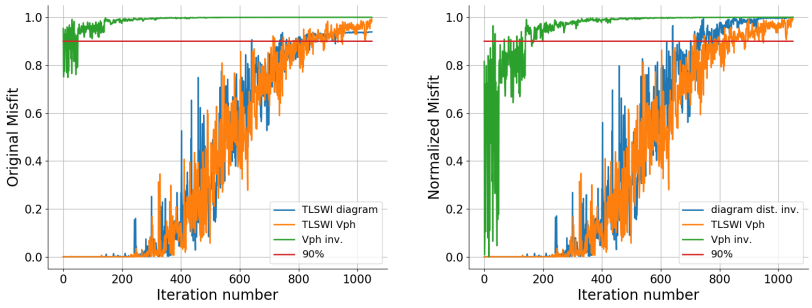


(a) (b)

Figure 4.8: Convergence curves of the DD-DTLSWI, $V_{ph}$-DTLSWI and $V_{ph}$-SWI, as function of the iteration number.

After normalization, the convergence curve of each inversion is limited between $[0, 1]$ where 0 represents the worst inverted model and 1 represents the model which is the closest to the measured one. In **Fig. 4.8 (b)**, one can see that the $V_{ph}$ inversion converges very quickly when the iteration number is around 400. And the $V_{ph}$-DTLSWI and the DD-DTLSWI need more iterations number for converging (nearly 900 iterations).

Considering a threshold of 90%, which corresponds to the red line in **Fig. 4.8**, the inverted models above this line from every inversion of repeatline are selected and presented in **Fig. 4.9**, using the DD-DTLSWI, $V_{ph}$-DTLSWI and $V_{ph}$-SWI respectively. **Fig. 4.9 (a)** and **(b)** show that the inverted results of each repeatline are highly concentrated so that each group of results can be easily separated from each other. However, the results of $V_{ph}$-SWI (**Fig. 4.9 (c)**) shows that $V_{s_2}$ cannot be distinguished for variation ratios less than 10%. The main reason is that the classical $V_{ph}$-SWI is not sensitive enough to estimate the small variations between models, especially for the variations in the deep layer (Wang et al., 2020b). As a consequence, the misfit function converges rapidly, as we can see in **Fig. 4.8**. The number of selected models for the $V_{ph}$-SWI is around 1000 (from the iteration number $\approx 200$), but the numbers of selected models for $V_{ph}$-DTLSWI and DD-DTLSWI are only 300 models (from iteration number $\approx 800$).

These inversion tests show the ability of the new time-lapse inversion approach to estimate the variation of shear-wave velocity in the deep layer, using synthetic signals based on a two-layer semi-infinite medium. However, since the dispersion diagram, instead of the theoretical dispersion curve, is calculated for each searched model in the inversion, this approach is more time consuming than the $V_{ph}$ inversion or the $V_{ph}$-DTLSWI. Nevertheless, if the number of iteration is sufficient for the convergence, the inversion results are more reliable than the $V_{ph}$ inversion.

### 4.5.2 Application on the epoxy-resin models

The dispersion curves of the four epoxy-resin models are presented in **Fig. 4.10 (a)**. As mentioned in the previous section, the variations between models are in the deep layer, which leads to the differences of phase velocity at low frequencies.

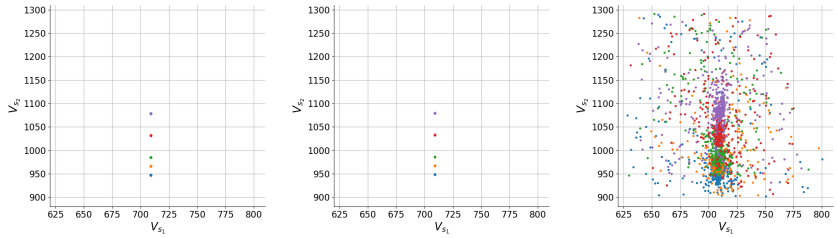

(a) (b) (c)

Figure 4.9: Inversion results using synthetic signals for models with 1% (blue), 3% (orange), 5% (green), 10% (red) and 15% (purple) variations. (a) DD-DTLSWI. (b) $V_{ph}$-DTLSWI. (c) $V_{ph}$-SWI. The models are selected by the 90% threshold.

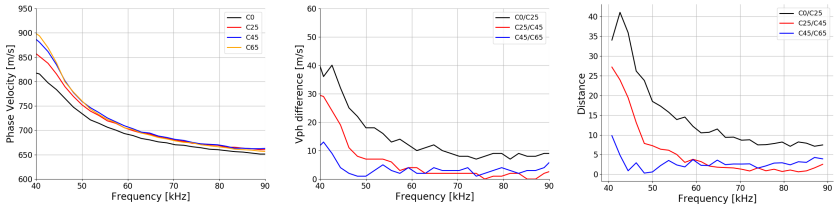


(a) (b) (c)

Figure 4.10: (a) Dispersion curves of epoxy-resin models. (b) The $V_{ph}$ difference between models (c) The ordinal type distances between models **Eq. 4.25**. The absolute values are presented for a better visualization.

The shallow layer of the models should be identical but through the measured dispersion curves, one can see that the $V_{ph}$ of $C0$ model at high frequencies are slightly smaller than other models. This difference is probably due to the manufacture of the resins. Besides, the difference between models $C0$ and $C25$ is the largest, and on the contrary, the difference between models $C45$ and $C65$ is the smallest. This can be verified by calculating the distances between measured diagrams (**Fig. 4.10 (b)**).

The DTLSWI approach is now applied on the measured diagrams of the epoxy-resin models. Three pairs of models are inverted: $C0/C25$, $C25/C45$, $C45/C65$ which follow the gradual increase of the shear-wave velocity in the deep layer. $V_p$ and $\rho$ are fixed in the inversion and the a priori information for $V_s$ and $h_1$ are: $V_{s_1} \in [500, 900]\, m/s$, $V_{s_2} \in [900, 1300]\, m/s$, $h_1 \in [7.0, 7.5]\, mm$. The deep layer are considered as semi-infinite. The frequency range of the inversion is $[40, 90]\, kHz$.

In **Fig. 4.11**, the inversion results are presented for the $V_{ph}$-SWI (red dots), $V_{ph}$-DTLSWI (purple dots) and DD-DTLSWI (blue dots). In each sub-figure, there are 1050 inverted models ($n_{s_0} = 50$, $n_s = n_r = n_i = 10$) for each color. On the top and the left images, $V_{s_1}$ and $V_{s_2}$ are presented with the misfit value, normalized using **Eq. 4.26**. The central parts of the images (bottom right) present the inverted models as function of $V_{s_1}$ and $V_{s_2}$.

**Fig. 4.11** shows that the inversion results of $V_{ph}$-DTLSWI and DD-DTLSWI

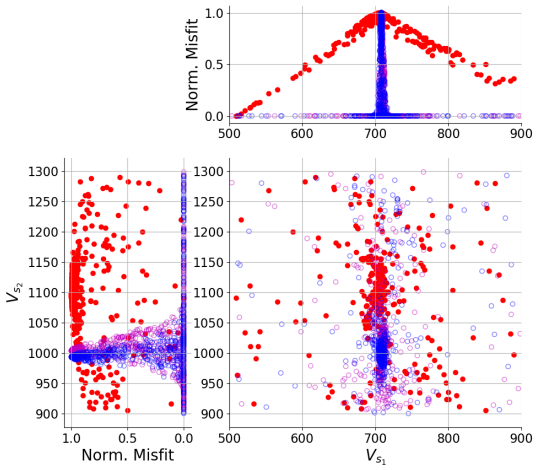


(a)

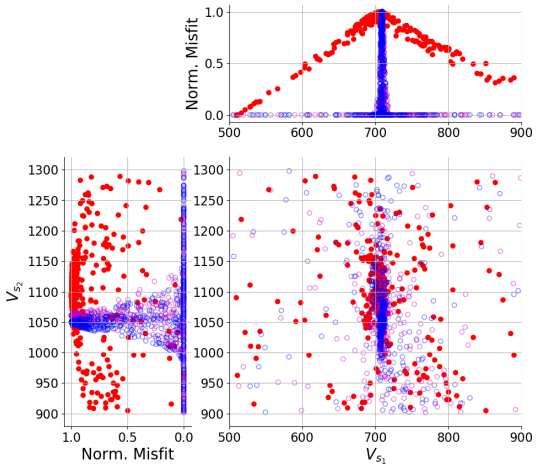


(b)

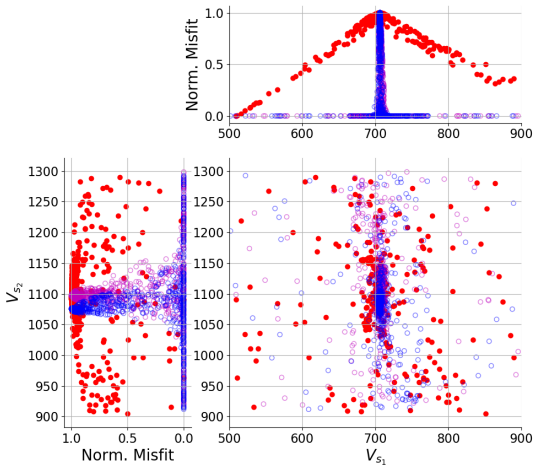


(c)

Figure 4.11: Inversion results for (a) C25; (b) C45; (c) C65. Blue: results for the DD-DTLSWI. Purple: Results for the $V_{ph}$-DTLSWI. Red: results for the $V_{ph}$-SWI.

Table 4.5: Mean values of selected models for the three epoxy-resin models inversion. Unity: $[m/s]$.

| model | true values | | $V_{ph}$-SWI | | $V_{ph}$-DTLSWI | | DD-DTLSWI | |
|---|---|---|---|---|---|---|---|---|
| | $\overline{V_{s_1}}$ | $\overline{V_{s_2}}$ | $\overline{V_{s_1}}$ | $\overline{V_{s_2}}$ | $\overline{V_{s_1}}$ | $\overline{V_{s_2}}$ | $\overline{V_{s_1}}$ | $\overline{V_{s_2}}$ |
| $C25$ | 708 | 990 | 708 | 1003 | 708 | 1003 | 708 | 993 |
| $C45$ | 708 | 1038 | 709 | 1060 | 709 | 1061 | 709 | 1050 |
| $C65$ | 708 | 1086 | 706 | 1096 | 706 | 1098 | 706 | 1076 |

are better distributed than that of $V_{ph}$-SWI. The reason is the same as mentioned in the numerical tests: classical $V_{ph}$-SWI is not efficient for discriminating the differences between models with small variations. From the family of models which have similar misfit function (the red dots in **Fig. 4.11**), it is difficult to find out which model(s) is(are) the best fitting one(s) to recover the model associated to measured data.

**Table 4.5** gives the mean values of the shear-wave velocities of the selected models for the three inversions ($V_{ph}$-SWI, $V_{ph}$-DTLSWI, DD-DTLSWI), using the 90% threshold for the normalized misfit function (**Eq. 4.26**). The inversion results for $V_{s_1}$ have negligible differences (less than $1\,m/s$ difference with the true values). Compared to the other two inversion methods, the DD-DTLSWI has the closest inversion results to the true $V_{s_2}$ values, for all three epoxy-resin models.

### 4.5.3 Application on the mortar-concrete slabs

The application of DD-DTLSWI and $V_{ph}$-DTLSWI on the laboratory data has proved the feasibility of this method. However, the epoxy-resin models that we measured are homogeneous and the measured data (phase velocity dispersion curves and diagrams) are fairly smooth and regular. In this part of study, we apply the new approach on three mortar-concrete slabs ($D01$, $D06$, $D08$), in which the materials properties are more heterogeneous resulting in imperfect measured data, i.e. phase velocity dispersion curves and diagrams (**Fig. 4.4**).

In **Fig. 4.12 (a)**, the dispersion curves of the three slabs are presented. The difference between slabs can be estimated through the dispersion curves: the changes of the mortar layers (shallow layer) correspond to the differences at high frequencies. However, differences can also be seen at low frequencies. This indicates that changes also occur in the concrete slabs (deep layer), which were meant to be identical for the three slabs. The $L1$ norm difference between $V_{ph}$ and the ordinal type diagram distances in **Fig. 4.12 (b)** agree with the variations in the dispersion curves and show that the variations are more important between the slabs D08 and D06.

The inversions are performed as shown in **Table 4.6**. The *a priori* information for each group is different but we keep the velocity range identical for the three inversions. The inversion results are presented in **Fig. 4.13**. The inverted models of time-lapse inversions (purple dots for TL $V_{ph}$ inversion and blue dots for diagram inversion) are more concentrated than the $V_{ph}$ inversion (red dots) with a slight difference at the center of each inversion.

In order to have a quantitative estimation of the inversion results, the mean value of the 200 best inverted models for each inversion is calculated, named

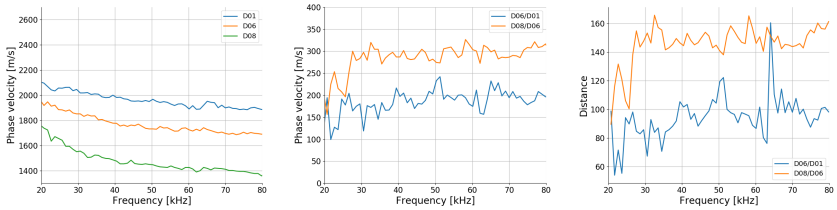


(a) (b) (c)

Figure 4.12: (a) The dispersion curves of the three slabs. (b) The $V_{ph}$ difference between slabs. (c) The ordinal type distance between slabs. Absolute values are presented for better observation.

Table 4.6: Three groups of inversions and corresponding a priori information.

| baseline | repeatline | $V_{s_1}\,[m/s]$ | $V_{s_2}\,[m/s]$ | $h_1\,[mm]$ |
|---|---|---|---|---|
| $D06$ | $D01$ | [1900, 2200] | [2100, 2600] | [20, 40] |
| $D08$ | $D06$ | [1700, 2000] | [1900, 2400] | [20, 40] |
| $D06$ | $D08$ | [1400, 1700] | [1800, 2300] | [20, 40] |

$\overline{m}^{200}$, where $m$ can be replaced by $V_{s_1}$ or $V_{s_2}$. The values are presented in the **Table 4.7**. One sees the shear-wave velocity variations in the mortar layers which corroborate to the compressional-wave velocity variations obtained from the seismic refraction method (see section 3.2). Variations are estimated in the concrete deep layer, which are expected to be identical by the manufacturer. The inversion results obtained by the three inversion approaches have slight differences in $V_{s_1}$: $\Delta V1(D01) < 3\,m/s$, $\Delta V1(D06) < 5\,m/s$, $\Delta V1(D08) < 3\,m/s$, compared to the mean value of inverted $Vs1$ for each slab. The errors of the inverted $V_{s_1}$ with respect to the mean value are less than 0.3%. The differences of inverted $V_{s_2}$ are $\Delta V2(D01) < 11\,m/s$, $\Delta V2(D06) < 12\,m/s$, $\Delta V2(D08) < 18\,m/s$, which gives a maximum error of 0.9%. The inversion results of the three inversion methods are in good agreement, which validates the use of DTLSWI in medium with higher heterogeneity than epoxy-resin models.

Then $\overline{m}^{200}$ is taken as reference value to calculate the standard deviation of each inversion, as function of iteration number:

$$std(m,n) = \sqrt{\frac{1}{N-n}\sum_{n}^{N}(m_n - \overline{m}^{200})^2}, \tag{4.27}$$

with $n$ the iteration number and $N$ the total number of iteration, $m$ the model parameter ($V_{s_1}$ or $V_{s_2}$).

The standard deviations of the inverted models are presented in **Fig. 4.14**. As shown in **Fig. 4.13**, the inverted $V_{s_1}$ are concentrated for all three inversions. Thus the differences between the $std(V_{s_1}, n)$ (**Fig. 4.14 (a)**) are not significant. However, in **Fig. 4.14 (b)**, the $V_{ph}$-DTLSWI and the DD-DTLSWI have smaller standard deviations for slabs $D06$ and $D08$. And the DD-DTLSWI has the smallest standard deviations for slab $D01$. When $n \approx 1000$, $std(V_{s_2}, n)$ of the two time-lapse inversions are greater than that of the $V_{ph}$ inversion with a small value, since the $V_{ph}$ inversion converges more rapidly than the other

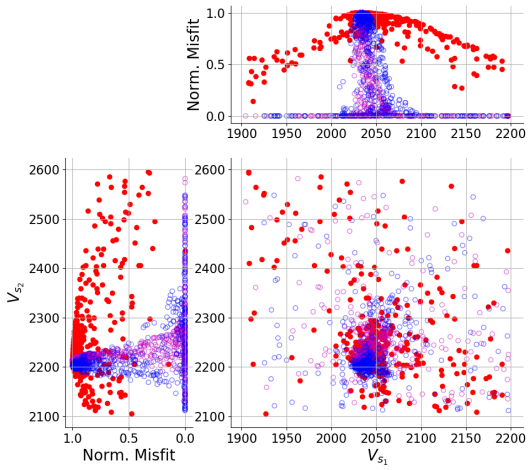


(a)

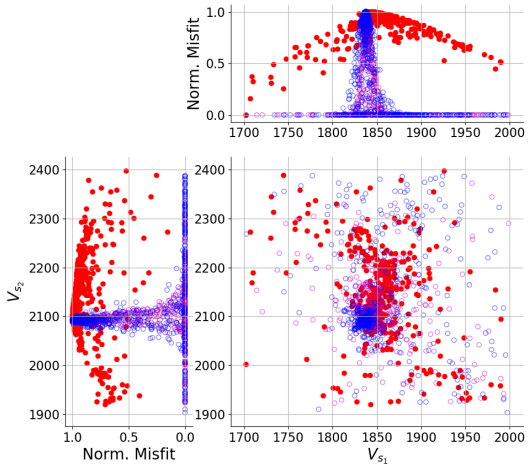


(b)

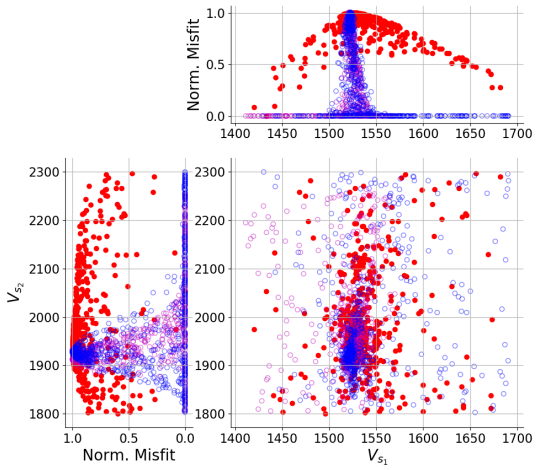


(c)

Figure 4.13: Inversion results for (a) D01; (b) D06; (c) D08. Blue: results for the diagram inversion. Red: results for the $V_{ph}$ inversion.

Table 4.7: Mean values of the inverted shear-wave velocities $\overline{V_{s_1}}^{200}$, $\overline{V_{s_2}}^{200}$ for the three slabs. Unity: $[m/s]$.

| slab | $V_{ph}$-SWI | | $V_{ph}$-DTLSWI | | DD-DTLSWI | |
|---|---|---|---|---|---|---|
| | $\overline{V_{s_1}}^{200}$ | $\overline{V_{s_2}}^{200}$ | $\overline{V_{s_1}}^{200}$ | $\overline{V_{s_2}}^{200}$ | $\overline{V_{s_1}}^{200}$ | $\overline{V_{s_2}}^{200}$ |
| $D01$ | 2030 | 2212 | 2032 | 2214 | 2035 | 2203 |
| $D06$ | 1842 | 2101 | 1837 | 2089 | 1837 | 2092 |
| $D08$ | 1524 | 1930 | 1521 | 1912 | 1523 | 1929 |

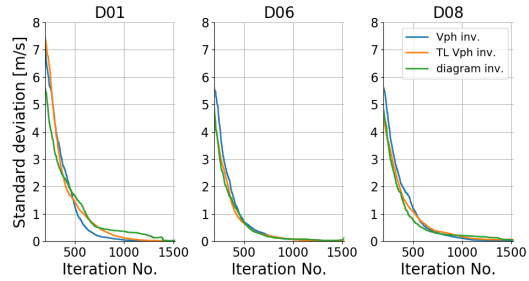


(a)

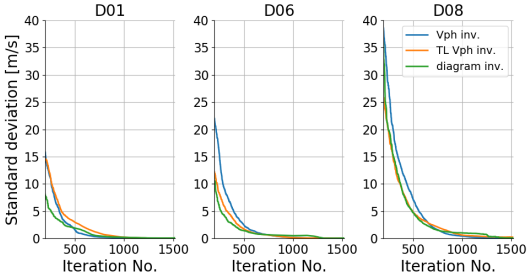


(b)

Figure 4.14: Standard deviations of each inversion: (a) $std(V_{s_1}, n)$; (b) $std(V_{s_2}, n)$.

time-lapse inversion.

## 4.6 Conclusion

In this study, we propose a differential time-lapse inversion approach for the monitoring of weak temporal variations, using the surface wave methods. Instead of applying independent inversions on the measured data, the DTLSWI uses the data difference as the inversion input data. Two DTLSWI approaches have been tested with two inversion input data: the first one is the simple difference between the phase velocities of the measured baseline and repeatline; the second one is the diagram distance of the dispersion diagrams of the baseline and repeatline. The diagram distance, based on the histogram distance, measures the distance between two dispersion diagrams, by regarding the dispersion diagram amplitude at one frequency as a distribution of velocity. Using

synthetic data to test different histogram distances, the ordinal type distance is shown to have the best behavior thanks to its ability to measure the similarity and the difference between two histograms at the same time.

The $V_{ph}$-DTLSWI and DD-DTLSWI have been tested on the numerical data and compared with the classical surface wave phase velocity inversion. Both DTLSWI can better estimate the variation of shear-wave velocity in the deep layer than $V_{ph}$-SWI. Then the laboratory data are used to verify the feasibility of the DTLSWI. The first laboratory data are recorded on four epoxy-resin two-layer models, with weak variations in the deep layer. Although $V_{ph}$-SWI converges faster than DTLSWI, the inversion results of the DTLSWI are more concentrated than the $V_{ph}$-SWI for both layers, which makes it easier to estimate the model variations. All three inversions have a good estimation of the shear-wave velocity of the shallow layer, but for the deep layer, DD-DTLSWI has the best inversion results compared to that of $V_{ph}$-SWI and $V_{ph}$-DTLSWI. The second laboratory experiments are made on three mortar-concrete slabs, where the mortar layer (top layer) of each slab has different water-to-cement ratio. A good agreement between the results of the three inversion methods validates the use of DTLSWI in a medium with higher heterogeneity. However, the DD-DTLSWI is the most time-consuming because the synthetic dispersion diagram is calculated at each iteration.

In this study, only the fundamental mode is considered for $V_{ph}$-SWI and $V_{ph}$-DTLSWI, and the principal lobe of the fundamental mode is used as the comparison zone for DD-DTLSWI. For further works tackling on multi-modal inversion, we can note that, the mode identification is unavoidable for $V_{ph}$-SWI and $V_{ph}$-DTLSWI, but not necessary for DD-DTLSWI. The dispersion diagram can be partially or completely taken into account for the diagram distance calculation, without the need of mode separation. This characteristic gives a real advantage of using the DD-DTLSWI. The synthetic data are constructed in the time domain by Inverse Fourier Transform, which considers only the Rayleigh wave phase velocity propagation and demands a high computational cost. Other numerical methods, e.g. Spectral Element Method, could be used for generating more realistic seismic data thus generalizing the DD-DTLSWI approach for more complicated cases.

## Acknowledgments

We would like to thank M. Le Feuvre, researcher at GERS-GeoEND Lab, Univ. Gustave Eiffel, for sharing the inversion program which is used in this article. Our thanks are also extended to M. Bader Eddin, for the experimental measurements and data management of the mortar-concrete slabs during his internship, with the assistant of F. Blaineau and A. Brosseau from Univ. Gustave Eiffel, COSYS-SII Lab, O. Durand, T. Devie, G. Gugole and F. Gallais from GERS-GeoEND Lab, Univ. Gustave Eiffel, and C. Boy from GINGER company. Finally, we would like to thank M. Wathelet, the co-developer of the Geopsy software. This work was co-funded by University Gustave Eiffel and the Région Pays de la Loire.

# Chapter 5

# Time-lapse inversion for surface waves: a differential approach using a linear approximation of the Rayleigh wave phase velocity

This chapter propose a second "differential inversion" methodology, using the linear assumption approximation of the Rayleigh wave phase velocity. It is named Analytical Differential Time-Lapse Surface Wave Inversion (ADTLSWI). The sensitivity kernel of Rayleigh wave phase velocity relates the model parameter variations with the phase velocity variation, which is used in the inversion process. The limits of the linear assumption are studied by error estimation of the theoretical and calculated (using the linear approximation) dispersion curves and inversion tests of numerical dispersion data. Finally, the ADTLSWI is applied on the measured data of reduced-scale models.

This chapter is also intended to be published in a scientific journal as the third article associated this thesis work. Thus the chapter presentation follows an article structure, with possible repetitions with the previous in the introduction, as already mentioned.

## 5.1 Introduction

Surface wave (SW) methods are widely used in near-surface applications, because they allow to quantitatively assess parameters of mechanical properties without difficulties thanks to the use of lightweight sources. Indeed, while body waves are highly attenuated in altered and unconsolidated underground, surface waves remain very energetic and easy to record. By inverting surface wave dispersion data, usually the phase or group velocity, the 1D medium's properties are recovered as function of depth. SW methods are for instance used for the monitoring of subsurface media, which are sensitive to environmental changes.

For example, we can cite the monitoring of the water table level in shallow aquifers (Pasquet et al., 2015a), the inner erosion in dams (Planès et al., 2016) or the water penetration in dikes (Joubert et al., 2018), the climate effects on railway embankments (Bergamo et al., 2016), etc.

The time-lapse monitoring aims to monitor temporal variations, through a series of measurements at different times. By comparing the measured data, such as the surface wave velocity attenuation or time delay, the variations in the medium can be estimated. For example, the temporal variations of surface wave velocity and attenuation during a tidal cycle can be extracted from a passive surface wave method (Joubert et al., 2018). However, if the quantitative estimations of the medium's parameter variations is needed, e.g. the temporal variations of S-wave velocity as a function of depth, an inversion process is essential.

Some recent studies have applied time-lapse inversion on measured data, to recover a quantitative estimation of the medium's paramater variations. In order to estimate the climate effects on railway embankment, Bergamo et al. (2016) measured and inverted the Rayleigh wave phase velocity and attenuation curves to construct the time-lapse model of S-wave velocity (depth profile of S-wave velocity as function of time). In this study, a velocity variation of 10% is estimated quantitatively for the Rayleigh wave and the inverted S-wave. Ikeda et al. (2017) inverted surface wave phase velocity dispersion data to monitor the environmental influences on shallow seismic velocity above the so called Aquistore $CO_2$ storage site. Higher phase velocities are observed in winter due to the increase of S-wave velocity with higher degree of frozen saturated rock. More recently, Wang et al. (2020b) have studied the sensitivity of the Rayleigh wave phase and group velocities with respect to the S-wave velocity. The authors show that these two types of dispersion data are not sensitive enough to small variations in the deep medium for a high accuracy of inversion results, and then propose to use the frequency derivative of the Rayleigh phase velocity as an innovate inversion input data to improve the recovery of the deep medium's small variations.

This lack of precision in inversion results is due to several key points in the entire inversion methodology, including the sensitivity of the input data to the inverted medium parameter but also the measurement uncertainty. This uncertainty should be taken care of during signal processing as it impacts the estimation of the variations in the medium for time-lapse monitoring. In case of surface wave approaches, the probability of the measurement error is generally considered as a Gaussian distribution (Tarantola, 2005; Menke, 2018). More precisely, O'Neill (2004) pointed out that a Lorentzian distribution is more appropriate than a Gaussian distribution for low frequencies, and proposed to use a realistic dispersion error for data uncertainty estimation. More recently, Dangeard et al. (2018) proposed a processing workflow to estimate the picking errors during the manual picking for extracting the surface wave phase velocity dispersion curve.

In deeper contexts of seismic monitoring tackled with Full Waveform Inversion, a recent proposition consists in taking into account differential information between two sets of consecutive measurement to overcome a major part of incertitude laying in the data (principally uncorrelated noise). This approach is called Double Difference Full Waveform Inversion (DDFWI) (Watanabe et al., 2004; Denli and Huang, 2009) and is based on the following principle: instead of

two independent inversions on the data measured at two different times (named baseline and repeatline respectively) and extraction of the model variations from two inversion results, the DDFWI (1) uses the inversion result of the measured baseline to calculate a synthetic baseline; (2) uses the subtraction of the measured baseline and the repeatline to reconstruct a synthetic repeatline by adding the measured difference to the synthetic baseline; (3) inverts the synthetic repeatline using the inversion result of the measured baseline as the initial model; (4) subtracts the inversion results of the measured baseline and the repeatline to recover the model parameter variations. The main advantage of this method is that the coherent noise between the measured baseline and repeatline can be removed by the subtraction, thus the differences in the two data-sets are mainly due to the model parameter variations (Asnaashari et al., 2012; Yang et al., 2015). Note that the incoherent noise is supposed to be canceled in the FWI method by stacking and the multi-receiver principle.

The differential inversion has been recently introduced for the SW methods by Wang et al. (2020a), where the difference of measured data is used as the inversion input data, through a diagram distance of two measured surface wave dispersion diagrams (abbreviated as DD-DTLSWI), and compared to the simple distance of two measured surface wave phase velocities (abbreviated as $V_{ph}$-DTLSWI). This differential inversion approach has been tested with numerical data and experimental laboratory data. The results show that the DD-DTLSWI can better estimate the variations than the $V_{ph}$-DTLSWI and the classical surface wave phase velocity inversion, in the case of two-layer media (first made of epoxy-resin and then mortar-concrete based).

In view of these promising results of differential inversion and with the aim of exploring different approaches to this principle, we propose in this article an alternative differential inversion technique that uses a linear approximation of the Rayleigh wave phase velocity. As described in the first section bellow, the analytical formulation of the Rayleigh phase velocity sensitivity kernel associates the model parameter variations with the phase velocity variations, making it possible to use the phase velocity difference in the differential inversion process. Since the analytical formulation of sensitivity kernel is used, we abbreviate this approach as ADTLSWI (Analytical Differential Time-Lapse Surface Wave Inversion). The behavior of the ADTLSWI is studied numerically in the third part, using theoretical phase velocity dispersion curves in order to analyze the limits of the linear assumption. Then, in the fourth part, the ADTLSWI is applied to laboratory data measured on reduced-scale epoxy-resin models.

## 5.2 Linear Approximation of Rayleigh wave phase velocity

With a given integer $q \geq 1$, and knowing that function $f(x)$ is $q$-times differentiable at the point $a$, the function $f(x)$ can be expanded according to Taylor's theorem to formulate the linear approximation of the function $f(x)$ at a point a with a precision of order $q$. When the function $f(x)$ is replaced by the Rayleigh wave phase velocity $V_{ph}(\mathbf{m})$ as function of model parameters $\mathbf{m}$ (including S-wave velocity $V_s$, P-wave velocity $V_p$, density $\rho$ and the layer thickness $h$), and $\mathbf{m_b}$ represents the baseline model parameters, the linear approximation of

Rayleigh wave phase velocity can be written:

$$V_{ph}(\mathbf{m}) = V_{ph}(\mathbf{m_b}) + \left[\frac{dV_{ph}}{d\mathbf{m}}\right]_{\mathbf{m_b}} (\mathbf{m} - \mathbf{m_b}) + o[(\mathbf{m} - \mathbf{m_b})], \tag{5.1}$$

with $\lim_{\mathbf{m}\to\mathbf{m_b}} o[(\mathbf{m} - \mathbf{m_b})] = 0$. $\left[\frac{dV_{ph}}{d\mathbf{m}}\right]_{\mathbf{m_b}}$ is the sensitivity kernel of the Rayleigh phase velocity, i.e. the phase velocity derivative with respect to the model parameter.

Neglecting the term $o[(\mathbf{m} - \mathbf{m_b})]$, which is here a second-order approximation, and writing the derivative of $V_{ph}$ in **Eq. 5.1** as the sum of partial derivatives for each model parameter in $\mathbf{m}$, it comes :

$$V_{ph}(\mathbf{m}) \approx V_{ph}(\mathbf{m_b}) + \sum_{m_i} \left[\frac{\partial V_{ph}}{\partial m_i}\right]_{m_{i_b}} (m_i - m_{i_b}), \tag{5.2}$$

with $i \in [1, 4]$ and $m_i = (V_s, V_p, \rho, h)$.

### 5.2.1 Sensitivity Kernels

Aki and Richards (2002) deduced the sensitivity kernel for Love waves, i.e. the Love wave phase velocity derivative with respect to the model parameters. One can apply this approach to Rayleigh waves to establish the Rayleigh wave sensitivity kernel (Takeuchi et al., 1972; Lai and Rix, 1998). The sensitivity curves of Rayleigh phase velocity with respect to the model parameters ($V_p$, $V_s$ and $\rho$) are

$$\left[\frac{\partial V_{ph}}{\partial V_p}\right]_{V_s,\rho,\omega} = \frac{V_p\rho}{2V_gIk^2}(kr_1 + \frac{dr_2}{dz})^2, \tag{5.3}$$

$$\left[\frac{\partial V_{ph}}{\partial V_s}\right]_{V_p,\rho,\omega} = \frac{V_s\rho}{2V_gIk^2}[(kr_2 - \frac{dr_1}{dz})^2 - 4kr_1\frac{dr_2}{dz}], \tag{5.4}$$

$$\left[\frac{\partial V_{ph}}{\partial \rho}\right]_{V_p,V_s,\omega} = \frac{V_p}{2\rho}\left[\frac{\partial V_{ph}}{\partial V_p}\right]_{V_s,\rho,\omega} + \frac{V_s}{2\rho}\left[\frac{\partial V_{ph}}{\partial V_s}\right]_{V_p,\rho,\omega} - \frac{1}{4V_gIk^2}\omega^2(r_1^2 + r_2^2). \tag{5.5}$$

$r_1(k, \omega, z)$ and $r_2(k, \omega, z)$ are the Rayleigh displacement vectors in the horizontal and vertical directions, respectively, which are two functions of the wavenumber $k$, the angular frequency $\omega$ (with the relation $\omega = 2\pi f$ and $f$ being the frequency), and the depth $z$. $V_g$ is the Rayleigh wave group velocity and $I = \frac{1}{2}\int_0^\infty \rho(r_1^2 + r_2^2)dz$ is the energy integral. **Eq. 5.3**, **Eq. 5.4** and **Eq. 5.5** can be used to calculate the sensitivity curves of Rayleigh wave phase velocity for the fundamental mode and higher ones. However, in our study, only the fundamental mode is considered in order to circumscribe the problem. Further studies should be conducted for higher modes.

The model parameters are piecewise functions with respect to depth. For a

Table 5.1: Parameters of a two-layer reference model. $V_p$: compressional-wave velocity; $V_s$: shear-wave velocity; $\rho$: density; $\nu$: Poisson's ratio; and $h$: layer thickness.

| layer ($i$) | $V_{p_i}^{ref}$ $[m/s]$ | $V_{s_i}^{ref}$ $[m/s]$ | $\rho_i^{ref}$ $[kg/m^3]$ | $\nu_i^{ref}$ | $h_i^{ref}$ $[m]$ |
|---|---|---|---|---|---|
| 1 | 1000 | 600 | 1500 | 0.22 | 8.0 |
| 2 | 2000 | 1100 | 2200 | 0.28 | $\infty$ |

1D model made of n layers, the model parameters are noted

$$\mathbf{m} = \begin{cases} (V_{s_1}, V_{p_1}, \rho_1), & z \in [0, h_1] \\ (V_{s_2}, V_{p_2}, \rho_2), & z \in [h_1, h_2] \\ \qquad\vdots & \\ (V_{s_n}, V_{p_n}, \rho_n), & z \in [h_{n-1}, \infty] \end{cases} \tag{5.6}$$

with $h_j$ being the depth and $\mathbf{m}_j$ being the model parameters of the $j$th layer ($h_0 = 0$).

Equations **Eq. 5.3**, **Eq. 5.4** and **Eq. 5.5** are also depth-dependent equations. **Fig. 5.1** shows the sensitivity curves of Rayleigh phase velocity, with respect to the model parameter $V_s$, $V_p$ and $\rho$, as a function of depth. A two-layer model (parameters available in **Table 5.1**) is used to calculate the sensitivity curves at four wavelengths (frequencies): $\lambda = \frac{h_1}{2}$, $\lambda = 2h_1$, $\lambda = 4h_1$ and $\lambda = 10h_1$. According to **Fig. 5.1**, the Rayleigh wave phase velocity is more sensitive to the variation of the S-wave velocity than to variations of P-waves velocity and density, especially at depth (i.e. below the first layer thickness $h_1$), since the values of the sensitivity with respect to $V_p$ and $\rho$ are nearly zero below this depth.

The sensitivity kernel of the phase velocity, with respect to the model parameters of each layer, is the integral of **Eq. 5.4**, **Eq. 5.3** and **Eq. 5.5**, in the corresponding depth range:

$$\left[\frac{\partial V_{ph}}{\partial V_{p_j}}\right]_{V_s,\rho,\omega} = \frac{1}{h_j - h_{j-1}} \int_{h_{j-1}}^{h_j} \left[\frac{\partial V_{ph}}{\partial V_p}\right]_{V_s,\rho,\omega} (z)dz, \tag{5.7}$$

$$\left[\frac{\partial V_{ph}}{\partial V_{s_j}}\right]_{V_p,\rho,\omega} = \frac{1}{h_j - h_{j-1}} \int_{h_{j-1}}^{h_j} \left[\frac{\partial V_{ph}}{\partial V_s}\right]_{V_p,\rho,\omega} (z)dz, \tag{5.8}$$

$$\left[\frac{\partial V_{ph}}{\partial \rho_j}\right]_{V_p,V_s,\omega} = \frac{1}{h_j - h_{j-1}} \int_{h_{j-1}}^{h_j} \left[\frac{\partial V_{ph}}{\partial \rho}\right]_{V_p,V_s,\omega} (z)dz. \tag{5.9}$$

$V_{p_j}$, $V_{s_j}$ and $\rho_j$ are model parameters at $j$th layer.

The phase velocity sensitivity kernel is calculated numerically using the model parameters in **Table 5.1** and presented in **Fig. 5.2**. The maximum depth for the integration calculation is $80\,m$ which equals to $10h_1$. **Fig. 5.2** shows that $V_s$ has more effects on the Rayleigh wave phase velocity, especially for greater depths. Indeed the maximum ratio of the sensitivity kernels of $V_s$ to $V_p$ or $\rho$ is higher for the deep layer. Considering this behavior, the following study will be carried out under the assumption that only $V_s$ changes, whereas $V_p$ and $\rho$ remain with the same values.

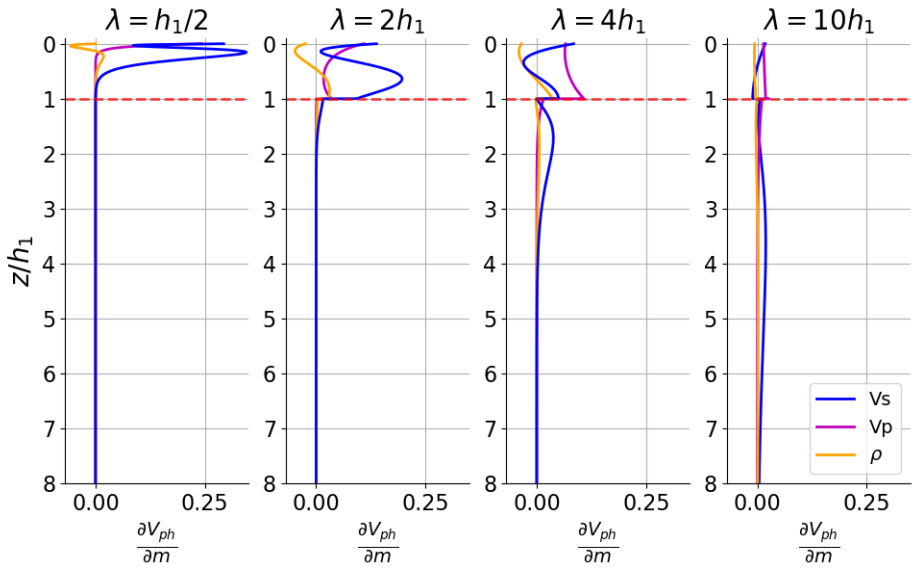


Figure 5.1: Sensitivity curves of the Rayleigh wave phase velocity of a two-layer model (parameters available in **Table 5.1**), presented as function of normalized depth. $h_1$ is the first layer thickness.

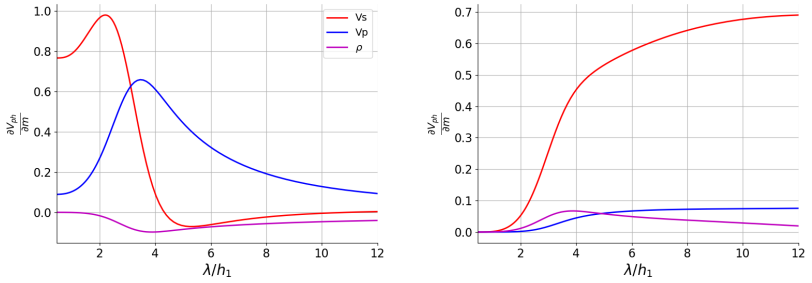


(a) (b)

Figure 5.2: Rayleigh wave phase velocity sensitivity kernel with respect to the model parameters $V_p$, $V_s$ and $\rho$ of (a) the shallow layer (layer 1 of **Table 5.1**) and (b) deep layer (layer 2 of **Table 5.1**), as a function of the wavelength divided by the thickness of the shallow layer $h_1$.

### 5.2.2 Error estimation

A two-layer model, named baseline $\mathbf{m_b}$, is used as the reference model. Its sensitivity kernel is calculated with respect to $V_s$. The model parameters of the baseline are in described **Table 5.1**. A series of models, named repeatline $\mathbf{m_r}$, are similar to the baseline parameters except S-wave velocities which is modified for each $\mathbf{m_r}$ model.

**Eq. 5.1** can be used to estimate the phase velocity of a repeatline model $\mathbf{m_r}$ from the knowledge of the phase velocity of a baseline model $\mathbf{m_b}$, under the condition that the models $\mathbf{m_b}$ and $\mathbf{m}$ are close enough so that the variations between $V_{ph}(\mathbf{m})$ and $V_{ph}(\mathbf{m_b})$ can be considered linear. In order to analyze the limits of **Eq. 5.1**, the estimated phase velocity using **Eq. 5.1** will be compared with its theoretical value. The S-wave velocity variation ratio is defined as

$$\alpha(V_{s_j}, b, r) = \frac{V_{s_j}^r - V_{s_j}^b}{V_{s_j}^b} \tag{5.10}$$

with $V_{s_j}^b$ and $V_{s_j}^r$ the S-wave velocity of $j$th layer, for the baseline $\mathbf{m_b}$ and the repeatline $\mathbf{m_r}$ respectively. In the following study, the S-wave velocity variation ratio of the repeatline for both layers are limited to the range: $\alpha(V_{s_1}) \in [-15, +15]\%$, $\alpha(V_{s_2}) \in [-15, +15]\%$.

The dispersion curves of the baseline and the repeatline (calculated using the Geopsy software (Wathelet, 2004)) are named $V_{ph}(\mathbf{m_b})$ (abbreviated as $V_{ph}^b$) and $V_{ph}(\mathbf{m_r})$ (abbreviated as $V_{ph}^r$) respectively. Using **Eq. 5.2**, the phase velocity of the repeatline can be estimated:

$$V_{ph}^{est}(\mathbf{m_r}) = V_{ph}(\mathbf{m_b}) + \sum_{m_i^r} \left[\frac{\partial V_{ph}}{\partial m_i}\right]_{m_i^b} (m_i^r - m_i^b). \tag{5.11}$$

The error between estimated and theoretical phase velocities (also called phase velocity error) of repeatline is defined using the $L2$ norm:

$$err(V_{ph}(\mathbf{m_r}), V_{ph}^{est}(\mathbf{m_r})) = \sqrt{\frac{1}{N_f} \sum_{N_f} \left(\frac{V_{ph}(\mathbf{m_r}) - V_{ph}^{est}(\mathbf{m_r})}{V_{ph}(\mathbf{m_r})}\right)^2} \times 100\% \tag{5.12}$$

with $N_f$ the number of frequencies sampled for the phase velocity dispersion curve.

**Fig. 5.3** shows the errors between the estimated and calculated dispersion curves of the repeatline, with the S-wave velocity variation ratio less than 15%. The phase velocity errors are more important for $V_{s_1}$ than for $V_{s_2}$. Actually, the Rayleigh wave phase velocity is more sensitive to the shallow medium's variations (see section 2.1: Sensitivity Kernels). Thus, when the variation occurs in the shallow layer, it is more difficult to estimate the correct phase velocity using **Eq. 5.1**. In other words, in the case of the shallow layer, we quickly move away from the hypothesis of linearity when the variation in S wave velocity increases.

In this section, the sensitivity kernel of the Rayleigh phase velocity has been calculated semi-analytically and then used to estimate the phase velocity of models with S-wave velocity variations. In the next section, the ADTLSWI

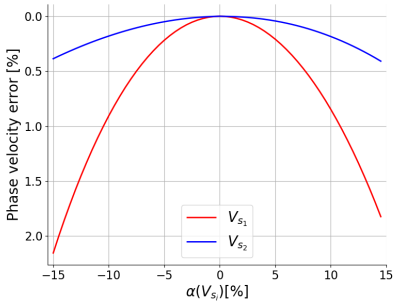


Figure 5.3: Phase velocity errors between the estimated and theoretical phase velocities of the repeatline. The variation ratios of both S-wave velocities are less than 15%.

approach will be proposed, using the linear approximation of the Rayleigh wave phase velocity to invert the phase velocity difference instead of the phase velocity itself.

## 5.3 Time-lapse inversion with linear approximation

Based on the linear approximation of the Rayleigh wave phase velocity (**Eq. 5.1**), we propose a new time-lapse inversion, using the difference of the phase velocity as the inversion input data. **Fig. 5.4** shows the work-flow of this time-lapse inversion.

$\mathbf{V_{ph}^b}$ and $\mathbf{V_{ph}^r}$ are two measured phase velocities in a time-varying medium at different times, so called *baseline* and *repeatline*. Assuming the initial state of the medium (the baseline model $\mathbf{m_b}$) is known, the inversion process searches the new state of the medium (the repeatline model $\mathbf{m_r}$) after some unknown variations has occurred in the medium.

$\mathbf{\Delta V_{ph}}$ calculates the simple difference between the two measured phase velocities $\mathbf{V_{ph}^b}$ and $\mathbf{V_{ph}^r}$: $\mathbf{\Delta V_{ph}} = \mathbf{V_{ph}^r} - \mathbf{V_{ph}^b}$. Based on the baseline model parameter $\mathbf{m_b}$, the sensitivity kernel of the baseline $\left[\frac{\partial \mathbf{V_{ph}}}{\partial \mathbf{m}}\right]_{\mathbf{m_b}}$ can be calculated (**Eq. 5.3**, **Eq. 5.4**, **Eq. 5.5**).

The model parameter of the repeatline $\mathbf{m_r}$ is the unknown in the inversion process, i.e. the inverted parameter. For each searched $\mathbf{m_r}$, the model difference $\mathbf{\Delta m}$ is calculated through the simple difference: $\mathbf{\Delta m} = \mathbf{m_r} - \mathbf{m_b}$. Using the linear approximation of the Rayleigh wave phase velocity (**Eq. 5.1**), the phase velocity difference $\mathbf{\Delta V'_{ph}}$ can be calculated:

$$\mathbf{\Delta V'_{ph}} = \left[\frac{\partial V_{ph}}{\partial m}\right]_{m_b} \mathbf{\Delta m}. \tag{5.13}$$

For numerically testing the ADTLSWI (Analytical Differential Time-Lapse Surface Wave Inversion) in the next section, a global optimization algorithm, the Neighborhood Algorithm (NA), is used. Proposed by Sambridge (1999a,b) and the improved by Wathelet (2008), the NA uses Voronoi cells to sample the

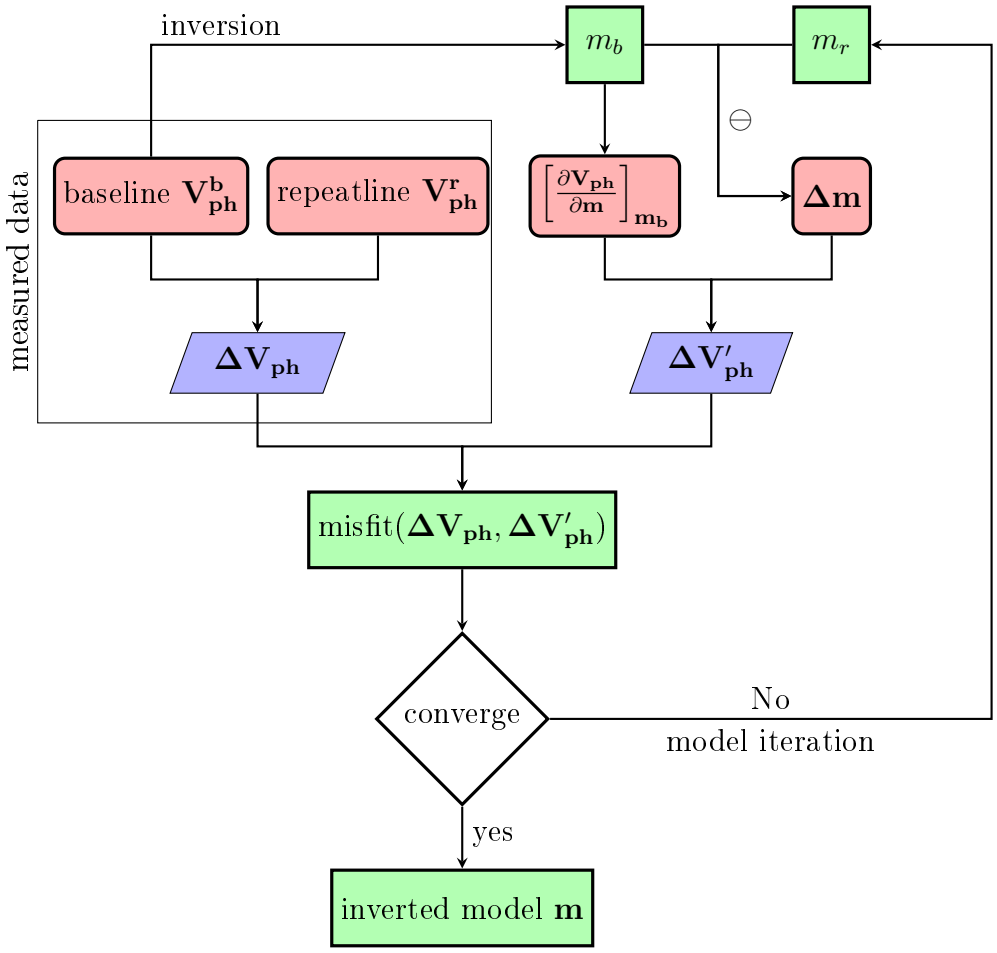


Figure 5.4: Work-flow of ADTLSWI. $\mathbf{m_b}$ is recovered by a previous inversion of the baseline measurement **b**; **r** is new model tested, as defined by the NA depending on the misfit values of the previous iteration.

parameter space and to generate models in a pseudo-random way. In the NA inversion, the objective function calculates the $L2$ norm between the two phase velocity differences (Wathelet, 2004)

$$misfit(\mathbf{\Delta V_{ph}}, \mathbf{\Delta V'_{ph}}) = \sqrt{\frac{1}{N_f}\sum_{N_f}(\Delta V_{ph} - \Delta V'_{ph})^2}. \tag{5.14}$$

In order to have the objective function in the range $[0, 1]$, the exponential of the misfit value is used by calculating the indicator $P$:

$$P = exp(-misfit) \tag{5.15}$$

We should note that instead of using the phase velocity, the time-lapse inversion uses the difference of the phase velocity as inversion input data, under the linear assumption of the Rayleigh wave phase velocity. However, when the variation is too important, the linear assumption is no longer applicable. In the next part, we test this method thanks to numerical dispersion data, to find out the feasibility and the limits of this method.

## 5.4 Numerical Tests

In section 2.2, the phase velocity errors have been analyzed to estimate the limits of the linear approximation of the Rayleigh wave phase velocity, using a baseline model and a series of repeatline models with variable S-wave velocities. Here, the limits of the linear approximation will be tested against the ADTLSWI.

### 5.4.1 ADTLSWI with large S-wave velocity variations

The baseline model is the same as in section 2.2 presented in **Table 5.1** and the variation ratio of the repeatline models, described by **Eq. 5.10**, is such as $\alpha(V_{s_i}) \in [-16, +16]\%$ (the variation ratio $\alpha(V_{s_i}, b, r)$ is simplified as $\alpha(V_{s_i})$ in this section). Three inversion tests are performed: (1) $\alpha(V_{s_1}) \in [-16, 16]\%$, $\alpha(V_{s_2}) = 0$; (2) $\alpha(V_{s_1}) = 0$, $\alpha(V_{s_2}) \in [-16, 16]\%$; (c) $\alpha(V_{s_1}) = \alpha(V_{s_2}) \in [-16, 16]\%$. Each test has 33 repeatline models. Each repeatline model will be paired with the baseline model for the time-lapse inversion, thus 33*3 inversion results are analyzed.

For each inversion process, the phase velocity of the baseline and the repeatline ($V^b_{ph}$, $V^r_{ph}$) are calculated theoretically using the Geopsy software, in the frequency range $[10, 150]\,Hz$ with a step of $0.5\,Hz$. It should be pointed out that since the difference of the phase velocity is the inversion input data, the a priori information is the variation range between the baseline and the repeatline model parameters. Here in each inversion, the repeatline S-wave velocities $V_{s_i}$ will be searched in the range $V_{s_i} \in [-20, +20]\% \times \Delta V_{s_i}$ ($\Delta V_{s_i} = V^r_{s_i} - V^b_{s_i}$). Other parameters ($V_p$, $\rho$ and $h_1$) are fixed: their values are given in **Table 5.1**.

Among a total number of 1020 searched models for each inversion case, only those models whose objective function (definied in **Eq. 5.15**) has a value greater than 99% of the value associated with the best model will be selected: $P_i \geq 99\% \times max(P_i)$ with $i \in [1, 1020]$. The inversion results of the three inversion tests are presented in **Fig. 5.5**. Each group of colored dots corresponds to

the results of one ADTLSWI with a pair of baseline-repeatline models. Each group of colored dots corresponds to the selected models in this inversion: $\alpha(V_{s_i})$ decreases from blue to red. This choice aims to visually differentiate the different zones of alpha values in the results. The black dot is the center of this group of inversion models. The gray triangle is the position of $\alpha(V_{s_i})$ for each repeatline.

In **Fig. 5.5 (a)**, the inversion results are presented as a function of the variation ratio $\alpha(V_{s_1}) \in [-16, 16]\%$ in the x-axis. In the y-axis, the inversion results are presented as the quotient of the difference between $V_{s_2}$ and $V_{s_2}^b$ with respect to $V_{s_2}^b$ (noted as $\Delta V_{s_2}/V_{s_2}^b$). Since $\alpha(V_{s_2}) = 0$ in these inversions, the centers of the inversion results should form a line at $\Delta V_{s_2}/V_{s_2}^b = 0$. However, in **Fig. 5.5 (a)**, the centers of the inversion results (black dots) has a parabolic shape: the inverted $V_{s_2}$ is biased. Besides, the distances between the black dots and the grey dots become significant when $\alpha(V_{s_1}) > 5\%$. The result shows that when large variations occur in $V_{s_1}$, the phase velocity cannot be correctly estimated due to the limits of linear approximation (see section 2.2). The inversion results are thus biased not only for $V_{s_1}$ but also for $V_{s_2}$.

In **Fig. 5.5 (b)**, the inversion results are presented as a function of the variation ratio $\alpha(V_{s_2}) \in [-16, 16]\%$ in the x-axis, and as a function of $\Delta V_{s_1}/V_{s_1}^b$ in the y-axis. The inversion results of $V_{s_1}$ are less biased compared to the inverted $V_{s_2}$ in **Fig. 5.5 (a)**. This corresponds to the error estimation in section 2.2: the high sensitivity of Rayleigh wave phase velocity with respect to $V_{s_1}$ makes it more difficult to estimate the phase velocity of the repeatline using **Eq. 5.1**. As a consequence, the inversion results are more biased when variations occur at shallow depth.

In **Fig. 5.5 (c)**, the variation ratios are equal for both layers, $\alpha(V_{s_1}) = \alpha(V_{s_2})$, so that the centers of the inversion results should line up (the grey dots). This is the case when $\alpha(V_{s_i}) \leq 5\%$. When $\alpha(V_{s_i}) = 5\%$, the inverted results of $V_s$ are $\alpha(V_{s_1}) = 4.79\%$, $\alpha(V_{s_2}) = 4.56\%$ instead of 5%; when $\alpha(V_{s_i}) = -5\%$, the inverted results of $V_s$ are $\alpha(V_{s_1}) = -5.17\%$, $\alpha(V_{s_2}) = -5.46\%$ instead of $-5\%$. This means that when the same proportion of variation occurs in $V_{s_1}$ and $V_{s_2}$, it is more difficult to estimate the deep layer variation using the ADTLSWI, which corresponds to the low sensitivity of Rayleigh wave phase velocity with respect to $V_{s_2}$ (see section 2.1).

These tests show the limit of the linear approximation for differential inversion in the context of this kind of two-layer media. According to these results, the ADTLSWI should be limited to cases where the model variations are lower than 5%, for both layers, above which the linear assumption is no longer relevant. Indeed if the variation is less than 5%, the mean of the results family extracted for misfit values greater than 99% compared to the maximum misfit value, reaches the correct expected value of the repeatline. In the next section, the ADTLSWI will be compared with other surface wave inversion methods, in the case of model parameter variations smaller than 5%.

### 5.4.2 ADTLSWI with weak S-wave velocity variations

For the two-layer model in **Table 5.1**, it has been shown that the ADTLSWI is applicable if the S-wave velocity variation is less than 5%. Respecting this limit, the ADTLSWI will be applied on the same baseline and repeatline models as before, using the theoretical phase velocities, and the inversion results will be compared to other surface wave inversion methods: the Rayleigh wave phase

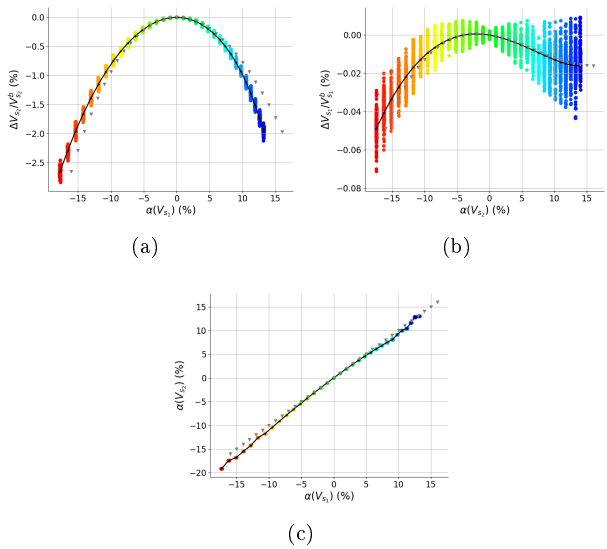

Figure 5.5: Inversion results using the ADTLSWI. Each group of colored dots corresponds to the selected models in this inversion: $\alpha(V_{s_i})$ decreases from blue to red. This choice aims to visually differentiate the different zones of alpha values in the results. Black dots: the center of each inversion models. Grey triangle: the expected results of $\alpha(V_{s_i})$. (a) $\alpha(V_{s_1}) \in [-16, 16]\%$, $\alpha(V_{s_2}) = 0$. (b) $\alpha(V_{s_1}) = 0$, $\alpha(V_{s_2}) \in [-16, 16]\%$. (c) $\alpha(V_{s_1}) = \alpha(V_{s_2}) \in [-16, 16]\%$.

velocity inversion (abbreviated as $V_{ph}$-SWI) and the frequency derivative of Rayleigh wave phase velocity inversion (abbreviated as PVD-SWI) (Wang et al., 2020b).

The $V_{ph}$-SWI uses the theoretical phase velocity dispersion curve as the inversion input data. The PVD-SWI uses the combined data of the phase velocity at high frequencies and the frequency derivative of the phase velocity at low frequencies. The study of Wang et al. (2020b) shows that the phase velocity derivative has a higher sensitivity to the medium variation than the phase velocity for the deep layer, so that the combined data leads to a robust inversion.

The three inversion input data are calculated theoretically in the frequency range $[10, 150]\,Hz$ with a step of $0.5\,Hz$. The combined data consists in the phase velocity derivative when $f \leq 60\,Hz$ and the phase velocity derivative when $f > 60\,Hz$. Since the variations between the baseline and the repeatline models are small ($\alpha(V_{s_i}) \leq 5\%$), the model parameters are searched in the same range for all inversions: $V_{s_1} \in [560, 640]\,m/s$, $V_{s_2} \in [1040, 1160]\,m/s$, i.e. $\Delta V_{s_1} \in [-40, 40]\,m/s$, $\Delta V_{s_2} \in [-60, 60]\,m/s$. All the other model parameters are fixed and their values available in **Table 5.1**.

A total number of 1020 models are searched for each inversion and only those models whose objective function (**Eq. 5.15**) has a value greater than 99% of the value associated with the best model are selected: $P_i \geq 99\% \times max(P_i)$ with $i \in [1, 1020]$. In **Fig. 5.6** and **Fig. 5.7**, the inversion results are presented as function of $V_{s_i}$, normalized by the corresponding values of the baseline model (**Table 5.1**).

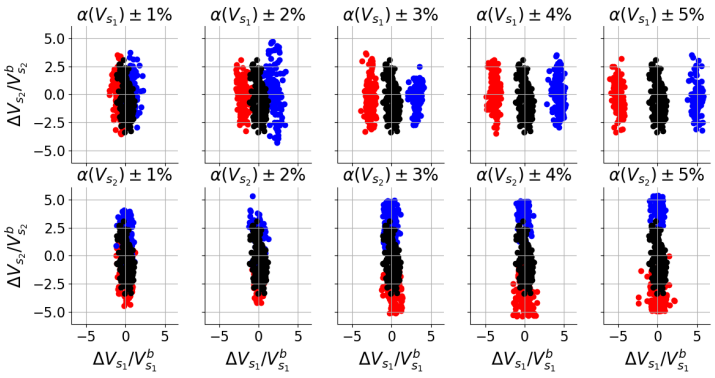


Figure 5.6: The inversion results of $V_{ph}$-SWI. Each dot corresponds to one inverted model with the colors representing the variation ratio of the medium. Red: $\alpha(V_{s_i}) < 0$; black: $\alpha(V_{s_i}) = 0$; blue: $\alpha(V_{s_i}) > 0$.

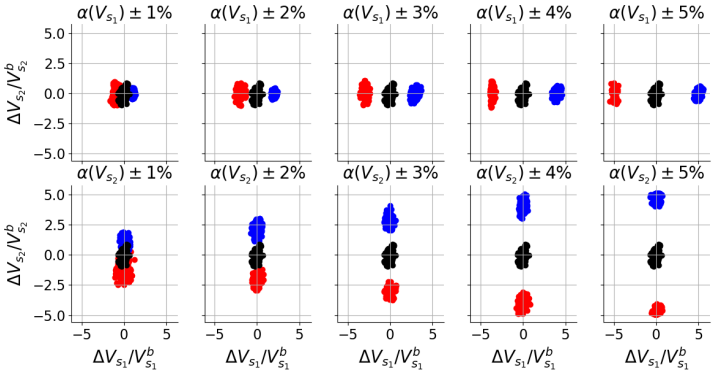


Figure 5.7: The inversion results of PVD-SWI. Each dot corresponds to one inverted model with the colors representing the variation ratio of the medium. Red: $\alpha(V_{s_i}) < 0$; black: $\alpha(V_{s_i}) = 0$; blue: $\alpha(V_{s_i}) > 0$.

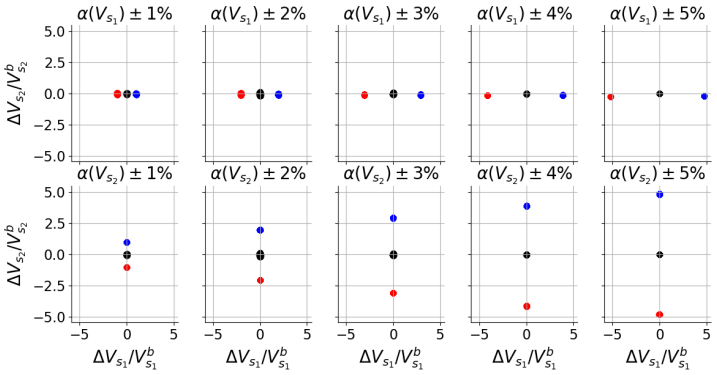


Figure 5.8: The inversion results of ADTLSWI. Each dot corresponds to one inverted model with the colors representing the variation ratio of the medium. Red: $\alpha(V_{s_i}) < 0$; black: $\alpha(V_{s_i}) = 0$; blue: $\alpha(V_{s_i}) > 0$.

As predicted in Wang et al. (2020b), $V_{ph}$-SWI is not capable to estimate weak variations of the medium, especially for the deep layer (**Fig. 5.6**). When $\alpha(V_{s_1}) \leq 2\%$ and $\alpha(V_{s_2}) \leq 5\%$, the inversion results are superimposed. The inversion results of the PVD-SWI can be separated when the variation is larger than 2%, for both layers (**Fig. 5.7**). Therefore, the PVD-SWI method can better estimate weak variations of the medium than $V_{ph}$-SWI approach, thanks to its higher sensitivity to the medium variation.

The inversion results of the ADTLSWI in **Fig. 5.8**, which takes advantage of time-lapse measurements through the workflow presented in **Fig. 5.4**, show the best behavior. Indeed, the inversion results of each group are centered and there is no overlapping of the inversion results even for the smallest variation ($\alpha(V_{s_i}) = 1\%$). However, a small bias for the centers of inversion results can be observed when $\alpha(V_{s_1}) = 5\%$, which corresponds to the limits of the linear approximation of the Rayleigh phase velocity depicted in the previous section.

Another advantage of the ADTLSWI is its low computing time due to the fact that the forward problem is calculated only once for the sensitivity kernel of the baseline $\left[\frac{\partial \mathbf{V_{ph}}}{\partial \mathbf{m}}\right]_{\mathbf{m_b}}$ (**Fig. 5.4**). In other surface wave inversion methods, such as the $V_{ph}$-SWI, the forward problem is calculated for each searched model, which is the most computing time-consuming part to the algorithm.

Theoretical Rayleigh wave phase velocities have been used to analyze the ability of the ADTLSWI for the estimation of weak medium's variations. The use of the ADTLSWI is valid when the variation of the medium is lower than 5%. The comparison of the ADTLSWI with the $V_{ph}$-SWI and the PVD-SWI shows that ADTLSWI has the best behavior. In the next section, the ADTLSWI will be applied on laboratory experimental data, in order to confirm this result and test the robustness of the ADTLSWI approach.

Table 5.2: $C25$ model parameters and dimensions. $h_i$: layer thickness; $l$ and $w$: length and width of model. Scale ratio between the numerical and the experimental model dimensions is 1000 (Pageot et al., 2017).

| layer | $V_{p_i}$ $[m/s]$ | $V_{s_i}$ $[m/s]$ | $\rho_i$ $[kg/m^3]$ | $\nu_i$ | $h_i$ $[mm]$ | l $[mm]$ | w $[mm]$ |
|---|---|---|---|---|---|---|---|
| 1 | 1300 | 708 | 450 | 0.29 | 7.2 | 265 | 235 |
| 2 | 2048 | 990 | 1300 | 0.37 | 203 | 265 | 235 |

## 5.5 Laboratory tests on reduced-scale models

### 5.5.1 Description of the experimental set-up

Three reduced-scale epoxy-resin models, named $C25$, $C45$ and $C65$ respectively, are designed in order to simulate small variations in the medium to mimic time-varying models at three different times. The model parameters and the dimensions of the $C25$ model are presented in **Table 5.2**. **Fig. 5.9 (a)** presents the $C25$ model and the experimental set-up: the edges of all the models are rounded according to arcs of circles in order to minimize and delay the boundary effects (Pageot et al., 2015) as it is visible for the $C25$ model in **Fig. 5.9**. The radius of the rounded edges have to be larger than or equal to the central wavelength, which is $12\,mm$ for all three epoxy-resin models used in this study. $C45$ and $C65$ have the same shape as $C25$, but have different S-wave velocities in their deep layer: $1038\,m/s$ for $C45$ and $1086\,m/s$ for $C65$ instead of $990\,m/s$ for $C25$. The variations of S-wave velocity in the deep layer are $\alpha(V_{s_2}, C25, C45) = 4.8\%$ and $\alpha(V_{s_2}, C45, C65) = 4.6\%$, calculated using **Eq. 5.10**, with $\Delta V_{s_2} = 48\,m/s$ for both groups.

The measurements of the three epoxy-resin models are carried out at MUSC (Mesure Ultrasonore Sans-Contact, or Non-Contact Ultrasonic Measurement in English) laboratory (Bretaudeau et al., 2011; Valensi et al., 2015; Pageot et al., 2017). This device makes possible to reproduce the same configuration as in field measurement but in a controlled environment on reduced-scale models. For that, a scale ratio in time and distances is assumed (1000 in this work) and ultrasonic sensors used. A piezo-electric transducer is used as an active source to generate a Ricker wavelet with a center frequency of $100\,kHz$. A moving laser interferometer measures the particle displacement, with a sampling rate equal to $10\,MHz$. **Fig. 5.9 (b)** gives information about the positions of the source and receivers. The distance between the source and the first receiver is $12\,mm$ and receivers are lined up for a total length equal to $90\,mm$ with a receiver spacing equal to $1\,mm$.

In **Fig. 5.10**, the measured seismograms are superimposed in order to see the differences between the three data-sets. **Fig. 5.11** presents the measured Rayleigh wave dispersion diagrams of the epoxy-resin models using the phase-difference processing method (Mokhtar et al., 1988; Park et al., 1998) with the phase velocity dispersion curves in black dots. Only the fundamental mode of the Rayleigh wave phase velocity is considered in the inversion.

### 5.5.2 Inversion results obtained with ADTLSWI

Two groups of ADTLSWI are tested in this section to recover material property variations thanks to couples of measured seismograms. First, $C25$ model will be

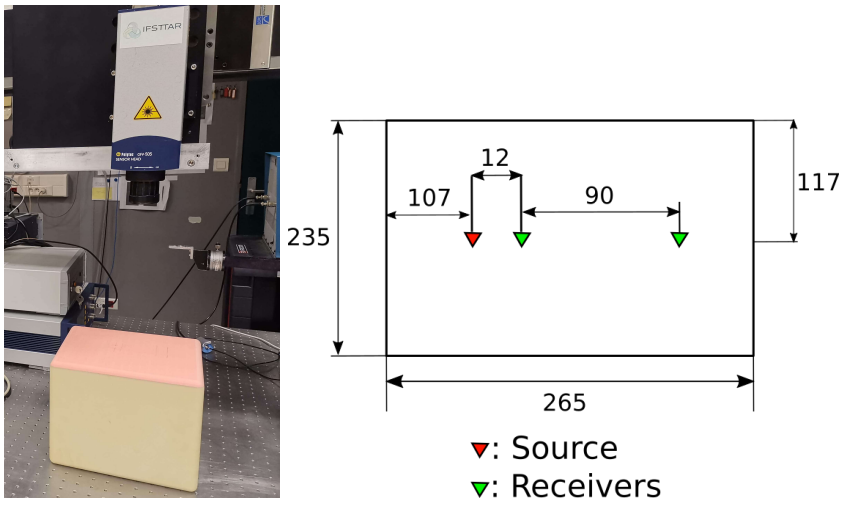


(a) (b)

Figure 5.9: (a) Experimental set-up and the two-layer resin model. (b) Position of source and the receiver vector for the epoxy-resin model measurement.

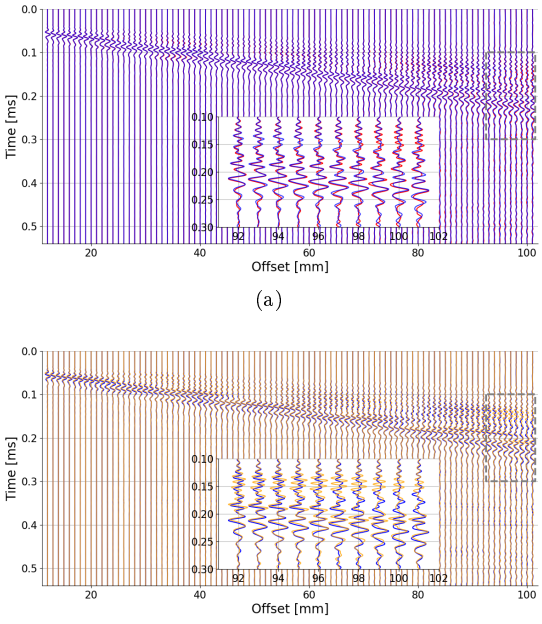


(a)

(b)

Figure 5.10: Measured seismograms for resin models. Red: $C25$; blue: $C45$; orange: $C65$. Signals in the grey rectangles ($t \in [0.1, 0.3]\,ms$, $x \in [92, 101]\,mm$) are zoomed for a better visualization.

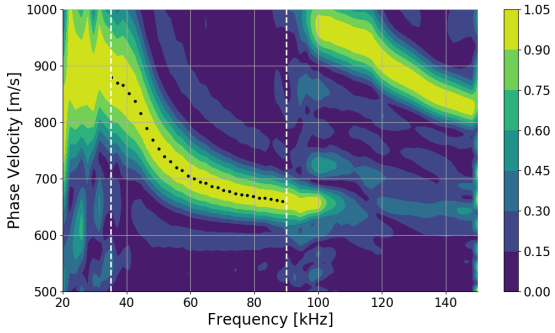


(a)

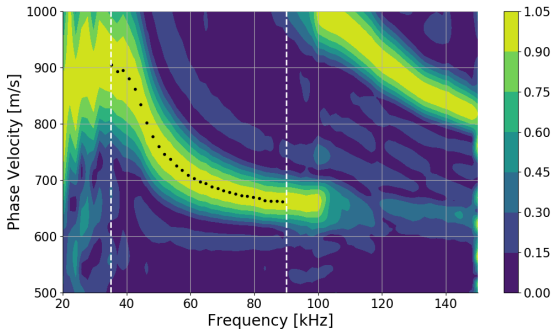


(b)

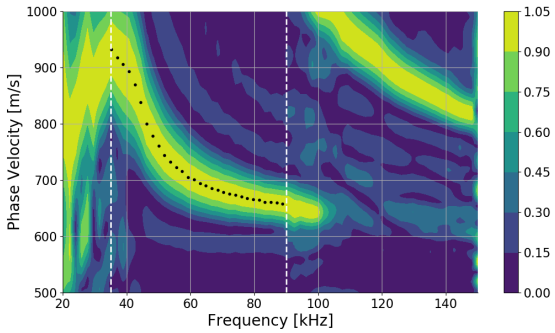


(c)

Figure 5.11: Measured dispersion diagrams of epoxy-resin models (a) $C25$, (b) $C45$ and (c) $C65$. Black dots: the Rayleigh wave phase velocity. White dashed line: the frequency range used in the inversion process.

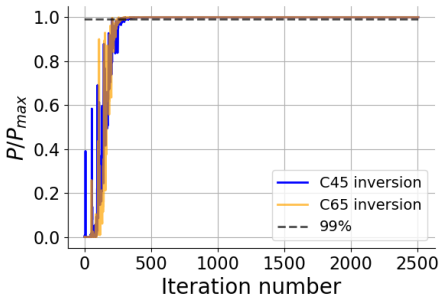


Figure 5.12: Convergence curves for ADTLSWI, using $C45$ and $C65$ as repeatline respectively.

Table 5.3: Comparison between the actual S-wave variations of the models and the inversion results. $V_{s_i}^{inv} = \Delta V_{s_i}^{inv} + V_{s_i}^{real}$ with $V_{s_i}^{real}$ the actual S-wave velocities of the epoxy-resin models (see section 5.1). Unity: $[m/s]$.

| baseline/repeatline | | $\Delta V_{s_i}^{real}$ | $\Delta V_{s_i}^{inv}$ | $V_{s_i}^{real}$ | $V_{s_i}^{inv}$ |
|---|---|---|---|---|---|
| $C25/C45$ | $V_{s_1}$ | 0 | +1.4 | 708 | 709.4 |
| | $V_{s_2}$ | 48 | 43.9 | 1038 | 1033.9 |
| $C45/C65$ | $V_{s_1}$ | 0 | -4.2 | 708 | 703.8 |
| | $V_{s_2}$ | 48 | 33.1 | 1086 | 1071.1 |

used as the baseline and $C45$ as the repeatline. Then $C45$ and $C65$ models are used as the baseline and the repeatline. Both groups will share the following settings:

- $V_p$, $\rho$ and $h_1$ are fixed (values available in **Table 5.2**);
- $\Delta V_{s_1} \in [-30, +30]\, m/s$, $\Delta V_{s_2} \in [-10, 110]\, m/s$;
- frequency range: $f \in [35, 90]\, kHz$.

$\Delta V_{s_1}$ is searched in the limited parameter space which corresponds to 3% variation of the $V_{s_1}$ since actually no variation occurs in shallow layers. The $V_{s_2}$ variation ratios are $\alpha(V_{s_2}, C25, C45) = 4.8\%$ and $\alpha(V_{s_2}, C45, C65) = 4.6\%$, respectively. Thus we search $\Delta V_{s_2}$ in the range $[-10, 110]\, m/s$ which corresponds to a variation range around $[-1, 11]\%$. Frequency limits are $35\, kHz$ at low frequencies, because of a low signal-to-noise ratio, and $90\, kHz$ at high frequencies in order to extract only the fundamental model and to avoid higher mode perturbations for all three models.

A total number of 2501 models are searched. The convergence curves ($P$ **Eq. 5.15**) as a function of the iteration number are presented in **Fig. 5.12**. One can see that both inversion processes converge fast since both curves reaches to the maximum ($P/P_{max} = 1$) when the iteration number is around 300. The inverted models exceeding the black dashed line ($P \geq 99\% \times P_{max}$) are selected. More than 2200 models are selected for both inversions.

**Fig. 5.13 (a)** presents the measured phase velocities of the three epoxy-resin models and **Fig. 5.13 (b)** shows the variations of the measured phase

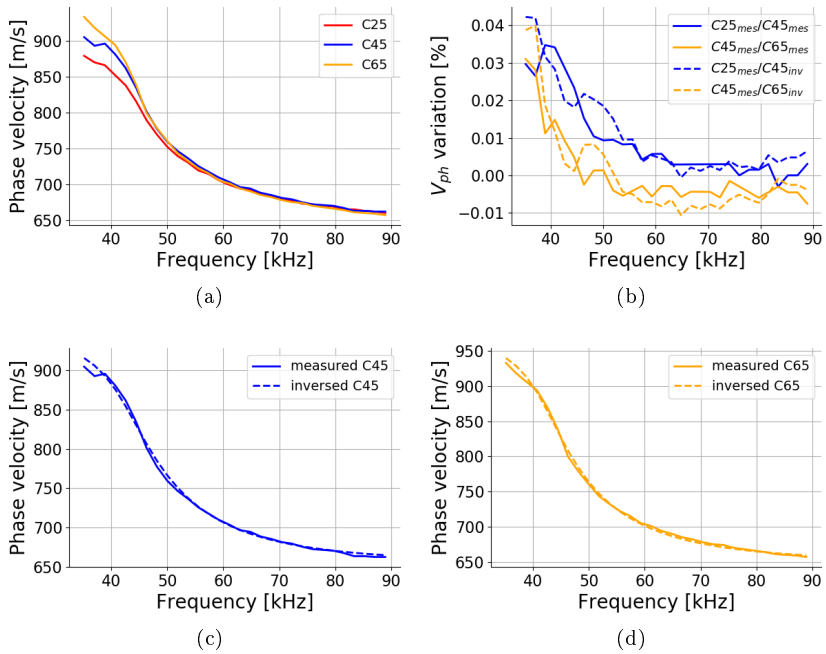


Figure 5.13: (a) Measured phase velocity dispersion curves of epoxy-resin models. (b) Relative variations for the measured phase velocities and the inverted phase velocities. "mes" stands for "measured" and "inv" stands for "inverted". (c) Measured and inverted phase velocities for $C45$ model. (d) Measured and inverted phase velocities for $C65$ model.

velocities (solid lines) by subtracting that of the repeatline to that of the baseline. The $V_{ph}$ variation is the simple difference between the baseline and the repeatline phase velocities, normalized by the baseline phase velocity for a clearer visualization ($\Delta V_{ph}/V_{ph}^{b}$).

A summary of the comparative results is presented in **Table 5.3**. It indicates the actual S-wave variations between models compared to the inversion results, calculated through the average values of the selected models. The inverted S-wave velocity of the repeatline $V_{s_i}^{inv}$ is calculated as the sum of the inverted S-wave velocity variation $\Delta V_{s_i}^{inv}$ and the real S-wave velocity of the baseline $V_{s_i}^{real}$ (available in section 5.1). The errors of the inversion results of $C25/C45$ are 0.2% for $V_{s_1}$ and 0.4% for $V_{s_2}$. The errors of $C45/C65$ inversion are 0.6% for $V_{s_1}$ and 1.4% for $V_{s_2}$, which are three time more than that of $C25/C45$ inversion.

We can notice large variations at low frequencies for the inverting groups $C25/C45$ and $C45/C65$ in **Fig. 5.13 (a)** and **(b)**. This is due to the shear-wave velocity variations actually expected in the deep layer. In parallel, at high frequencies ($f \geq 60\,kHz$), small variations (negative values) are observed on the $V_{ph}$ variation (**Fig. 5.13 (b)**) for $C45/C65$ (yellow solid line), which means the shallow layers of $C45$ and $C65$ are not perfectly identical. This explains why $\Delta V^{inv}$ equals to $-4.2\,m/s$ instead of 0 after the ADTLSWI for $C45/C65$.

Using the inverted S-wave velocities in **Table 5.3**, inverted phase velocity

dispersion curves are calculated and compared with the measured phase velocities (**Fig. 5.13 (c)** and **(d)**). A good fitting between the measured and inverted phase velocities is observed for both models. The $V_{ph}$ variations between the inverted phase velocity of repeatline ($C45^{inv}$ or $C65^{inv}$) and the measured phase velocity of baseline ($C25^{mes}$ or $C45^{mes}$) are presented in **Fig. 5.13 (b)** (dashed lines).

### 5.5.3 Discussion

The presented tests conducted on laboratory data make possible to experimentally validate the applicability of ADTLSWI but also determine its limitations in the context defined of the two-layer model chosen. Actually the analysis on the experimental data shows the feasibility of the ADTLSWI process and its performance in case of weak velocities variations, i.e. lower than 5%, for which the linear approximation of the Rayleigh wave phase velocity can be efficiently considered.

A prominent numerical advantage of the ADTLSWI is its low calculation time as the sensitivity kernel is calculated only once based on the baseline model parameters. However, this differential approach needs an accurate assessment of the baseline model, i.e. a previous fine inversion of the baseline data to provide a robust reference model without which the results on the repeatline can be biased by error propagation.

Note that the study presented here is based on a two-layer model for which using only the fundamental mode is suitable as it is dominant. However, in case of models including a large parameter contrasts between layers, a multiple mode study would be of interest. In this case, the sensitivity kernel should be updated to contain the information of multiple modes.

The small scale models used here for the applicability of the method make use of ultrasonic techniques in a laboratory environment, which means that the experiments are under control with a fixed position of the source and a shared generated source signal, controlled receiver positions with high accuracy, epoxy-resin parameters well known. However, in case of field measurements, it should be important to consider uncertainty issues, since several parameters are not controlled and difficult to assess. This aspect is not addressed in this paper and should be tackled in further research works. It is expected that this methodology could be successfully used in monitoring applications where the sensors are permanently embedded.

## 5.6 Conclusion

An Analytical Differential Time-Lapse Surface Wave Inversion (ADTLSWI) is proposed in this study for the purpose of monitoring small variations of the medium. It uses the simple difference of two successive measured phase velocity dispersion curves ($\Delta V_{ph}$) as inversion input data. The latter is inverted through the ADTLSW by using a linear assumption of the Rayleigh wave phase velocity and sensitivity kernels (which describes the partial derivative of the Rayleigh wave phase velocity with respect to the model parameters) in order to mathematically link $\Delta V_{ph}$ with variation of model parameters $\mathbf{\Delta m}$.

ADTLSWI approach has been firstly tested on numerical data. Two-layer models are used to simulate variations occurring in the shallow and deep layers. The analysis of the process results has shown that the linear approximation of the Rayleigh wave phase velocity cannot be used when the variations are larger than 5%. Besides, the ADTLSWI method provides greater bias in the results of variations in the shallow layer than in the deep layer. This behavior is due to the higher sensitivity of the Rayleigh wave phase sensitivity to S-waves variations in the shallow layer than in the deep layer. Compared to the $V_{ph}$-SWI and PVD-SWI, the ADTLSWI is more efficient for estimating the weak variations to the medium (variations less than 5%) furthermore at a lower computational cost.

The ADTLSWI methodology was finally applied on laboratory data for experimental validation in the two-layer context. Theses data have been carried out on three small-scale epoxy-resin two-layer models. The inversion results are in good agreement with the measured data and the known model parameters. However, the limitation of the ADTLSWI is also pointed out. The baseline model should be well known before the use of ADTLSWI since the sensitivity kernel calculation is based on the baseline model parameters. This could be difficult for the application on the field experiments.

Actually, the test with the laboratory data is an intermediate step between numerical test and field experiment. Further studies with field data and thus uncontrolled factors are the next steps. However, medium's variations may be unknown in the field measurements, or known as being weak variations but cannot be sure to be lower than 5%. In this case, another differential time-lapse surface wave inversion approach, using the diagram distance to measure the difference between measured data, should be more appropriate (Wang et al., 2020a). Moreover, the PVD-SWI process can be implemented as an alternative method to estimate the baseline model with more precision. In a global blind monitoring approach, we recommend firstly to use the PVD-SWI method for determining the baseline model, then to proceed to the differential inversion with the DD-DTLSWI and, if the results sounds close or lower to 5%, to refine the results by applying the ADTLSWI approach. We can note the complementary of the latter to the other recent innovative propositions dedicated to accurate inversion of surface waves for monitoring issues.

At last, only the fundamental mode of the Rayleigh wave is used in this study, whereas in some cases multiple mode study would be efficient. Further studies should be conducted in this direction.

# Chapter 6

# Conclusion

The thesis work presented in this manuscript tackles surface wave inversion challenges linked to the monitoring of weak variations of mechanical properties in the subsurface media particularly impacted by the climate change. Face to the limitations of the results accuracy when using the classical MASW (Multichannel Analysis of Surface Waves) approach based on the inversion of phase velocity dispersion of Rayleigh Waves, we propose and analyze three alternative strategies. These new approaches innovate in terms of inversion input data. The first one proposes to use the frequency derivative of Rayleigh wave phase velocity as input data in the inversion process. The second and the third propositions are based on a "differential inversion" (abbreviated as DTLSWI), where the data differences are inversion input data instead of independent measured data-sets. All the three proposed strategies are tested numerically and experimentally, using laboratory-measured data.

They show behaviors improving the efficiency of the surface waves inversion for recovering weak variations of the S-waves velocities in subsurface media. These characteristics are different depending of the proposed strategies as summarized bellow and their interests can be complementary to answer monitoring needs.

## 6.1 Surface wave inversion using frequency derivative of Rayleigh wave phase velocity

In the first approach, the use of frequency derivative of the phase velocity as the input data for inversion instead of the phase velocity or group velocity dispersion as classically done. A sensitivity study is carried out in order to analyze the ability of these different dispersion data to estimate small variations in two-layer models. The three types of dispersion curves mentioned above, i.e. the Rayleigh wave phase and group velocities ($V_{ph}$ and $V_g$), and the frequency derivative of the Rayleigh wave phase velocity (abbreviated as PVD, Phase Velocity Derivative), are compared. According to the sensitivity study, the PVD is more sensitive to the deep layer's variations than the phase and group velocities, since it contains the information of both layers at wavelengths around 3.4 times the thickness of first layer.

A combined data, consisting of PVD at low frequencies and phase velocity

at high frequencies in order to contain both the high sensitivity of PVD and the robustness of phase velocity at the same time, is proposed and tested numerically, using the theoretical dispersion curves of a series of two-layer models. The inversion results of the combined data are compared with that of $V_{ph}$ and $V_g$. It is shown that $V_{ph}$ and $V_g$ can estimate the two-layer medium's variations when (1) the shear-wave velocity variations in the shallow layer ($V_{s_1}$) are greater than 3% or (2) the shear-wave velocity variations in the deep layer ($V_{s_2}$) are greater than 5%. Compared to $V_{ph}$ and $V_g$, the inversion results of the combined data show a quasi-equivalent estimation for $V_{s_1}$, but a better estimation for $V_{s_2}$: variations in both layers can be estimated when they are greater than 3%.

The feasibility of PVD is then verified experimentally using two small-scale epoxy-resin models measured in the laboratory. The two epoxy-resin models have a 17% variation in the shear-wave velocity of their deep layer ($V_{s_2}$). The variation is estimated by two inversion approaches, using $V_{ph}$ and combined data respectively. The $V_{ph}$ inversion estimates a $16.4 \pm 1.1\%$ variation of $V_{s_2}$ and the combined data inversion estimates a $17 \pm 0.3\%$ variation of $V_{s_2}$. Regarding the expected velocity values of the deep layer, the combined method gives more precise results with a smaller error.

## 6.2 Differential time-lapse surface wave inversion

The notion of "differential inversion" is introduced for surface wave methods through two strategies: in the first one, the diagram distance (DD-DTLSWI) is defined as a distance of two dispersion diagrams by assimilating the lobes of the fundamental mode in the dispersion diagram as a series of histograms of velocity distributions, i.e. one histogram for each frequency; the second one uses a linear approximation of the Rayleigh wave phase velocity (ADTLSWI) to associate the phase velocity variations with the model variations.

### 6.2.1 Diagram distance

The diagram distance calculates the difference between two dispersion diagrams, based on a statistical distance which measures the difference and the similarity between two histograms. We propose to use the diagram distance as the input data in the surface wave inversion process, taking the principal lobe of the fundamental mode in each of the two dispersion diagrams as comparison zones.

Another DTLSWI is also proposed as an intermediate step between the DD-DTLSWI and surface wave phase velocity inversion ($V_{ph}$-SWI), using the simple difference between the Rayleigh phase velocities as inversion input data ($V_{ph}$-DTLSWI). Numerical tests on the three inversion input data show that the two DTLSWI can better estimate small variations in two-layer media, when variations occur in the deep layer.

The first experimental test is based on the measurements of four epoxy-resin two-layer models with gradual shear-wave velocity variations in the deep layer. The inversion results of the three inversion approaches ($V_{ph}$-SWI, $V_{ph}$-DTLSWI and DD-DTLSWI) have less than $1\,m/s$ difference with the true value of $V_{s_1}$ for all three pairs of baseline/repeatline models. But compared to the other

two inversion methods, the DD-DTLSWI has the closest inversion results to the true $V_{s_2}$ value.

Three mortar-concrete slabs are used as a second experimental application of the DD-DTLSWI, where the heterogeneity of the material is more important than in the epoxy-resin models. Compared the inversion results of each inversion process to the mean value of the three inversions, errors of the inverted shear-wave velocities are less than 0.3% for $V_{s_1}$ and 0.9% for $V_{s_2}$. The good agreement between the three inversion approaches validates the feasibility of the DD-DTLSWI in a heterogeneous medium, which shows a great potential for applications in the field. Standard deviations of inverted models are calculated as a function of iteration number for the three inversions. It proves that the $V_{ph}$-SWI converges more rapidly (i.e. for less iterations number) than $V_{ph}$-DTLSWI and DD-DTLSWI, but the two differential inversions have more concentrated inversion results.

### 6.2.2 Linear approximation of Rayleigh wave phase velocity

A linear approximation of the Rayleigh wave phase velocity is used to associate the phase velocity variations with the model variations, by using the sensitivity kernel (i.e. partial derivative of the Rayleigh wave phase velocity with respect to the model parameters). A sensitivity study shows that the Rayleigh wave phase velocity is more sensitive to shear-wave velocity, compared to compressional-wave velocity and density. Then the errors between the theoretical phase velocity and the one calculated by multiplying the sensitivity kernel and the simple difference of model parameters, are estimated, based on a series of two-layer models. It shows that when the variations occur in the shallow layer ($V_{s_1}$), more difficulties appear for correctly estimating the phase velocity using the linear approximation than the variations in the deep layer ($V_{s_2}$), because of a high sensitivity of Rayleigh wave phase velocity with respect to $V_{s_1}$.

Numerical tests on the ADTLSWI are performed with a series of two-layer models where the variations between them are ranged in $[-16, +16]$%. The theoretical analysis as well as the numerical test results show that the ADTLSWI is efficiently applicable when the medium's variations are less than 5%. Comparisons have also been made with $V_{ph}$-SWI and PVD-SWI for estimating weak variations (less than 5%). The results analysis show behaviors that indicate the following order in term of efficiency of the methods ADTLSWI > PVD-SWI > $V_{ph}$-SWI from good to bad.

Laboratory tests are based on three two-layer epoxy-resin models, where the shear-wave variations between them are respectively 4.8% and 4.6%. Applying the ADTLSWI, the inverted $V_{s_1}$ have respectively 0.2% and 0.6% errors for the two repeatline models, and the inverted $V_{s_2}$ have respectively 0.4% and 1.4% errors. This accuracy approves the ability of ADTLSWI to estimate weak variations in a two-layer medium.

## 6.3 Discussion and Prospect

Concerning the strategies proposed for the monitoring by surfaces waves inversion, the three studies have been respectively conducted for defining their poten-

tial. Each one is based on simple two-layer models, taking only the fundamental mode into account. This choice was motivated to (1) clarify the analysis since only few model parameters are concerned; (2) limit the computing cost. From realistic considerations, further studies should be focused on the expansion and the generalization of these inversion approaches on multiple-layer media with multi-modal studies.

In a global blind monitoring approach, we recommend firstly to use the PVD-SWI method for determining the baseline model, then to proceed to the differential inversion with the DD-DTLSWI and, if the results sounds close or lower to 5%, to refine the results by applying the ADTLSWI approach. We can note the complementary of the latter to the other recent innovative propositions dedicated to accurate inversion of surface waves for monitoring issues.

Application tests have been carried out with laboratory-measured data of reduced scale models for the three approaches. However, field tests are also essential as more uncontrolled factors appears so that the feasibility and the robustness can be verified in realistic conditions.

In the numerical tests, synthetic seismograms are calculated using Inverse Fourier Transform and tackled at each receiver position. Two problems should be taken care for the improvement of the calculation code. (1) Loops are required on both frequency and the receiver position which slows down the calculation time. (2) Only the Rayleigh wave is taken into account which do not simulate realistic data. Numerical approaches, such as the Spectral Element Method, could be implemented in the Python code in order to generate more realistic data.

In summary, further works should be carried out to test the robustness of the improvements highlighted in this thesis, by conducting additional studies both on more complex numerical simulation data, field experiments as well as methodological approaches involving the information provided by the higher modes.

# Bibliography


Aarts, E. and Korst, J. (1988). Simulated annealing and boltzmann machines.

Abo-Zena, A. (1979). Dispersion function computations for unlimited frequency values. *Geophysical Journal International*, 58(1):91–105.

Aki, K. and Richards, P. (2002). *Quantitative Seismology, 2nd Ed.* University Science Books.

Arts, R., Eiken, O., Chadwick, A., Zweigel, P., Van der Meer, L., and Zinszner, B. (2003). Monitoring of co2 injected at sleipner using time lapse seismic data. In *Greenhouse Gas Control Technologies-6th International Conference*, pages 347–352. Elsevier.

Arts, R., Elsayed, R., Van Der Meer, L., Eiken, O., Ostmo, S., Chadwick, A., Kirby, G., and Zinszner, B. (2002). Estimation of the mass of injected co2 at sleipner using time-lapse seismic data. In *64th EAGE conference & exhibition*, pages cp–5. European Association of Geoscientists & Engineers.

Asnaashari, A., Brossier, R., Garambois, S., Audebert, F., Thore, P., and Virieux, J. (2012). Time-lapse imaging using regularized fwi: a robustness study. In *SEG Technical Program Expanded Abstracts 2012*, pages 1–5. Society of Exploration Geophysicists.

Auger, F. and Flandrin, P. (1995). Representations by the Reassignment Method. *IEEE Transctions on Signal Processing*, 43(5):1068–1089.

Bergamo, P., Dashwood, B., Uhlemann, S., Swift, R., Chambers, J. E., Gunn, D. A., and Donohue, S. (2016). Time-lapse monitoring of climate effects on earthworks using surface waves. *Geophysics*, 81(2):EN1–EN15.

Bhattacharya, S. N. (2015). Sensitivities of surface wave velocities to the medium parameters in a radially anisotropic spherical Earth and inversion strategies. *Annals of Geophysics*, 58(5).

Bishop, T., Bube, K., Cutler, R., Langan, R., Love, P., Resnick, J., Shuey, R., Spindler, D., and Wyld, H. (1985). Tomographic determination of velocity and depth in laterally varying media. *Geophysics*, 50(6):903–923.

Bodet, L., Abraham, O., and Clorennec, D. (2009). Near-offset effects on rayleigh-wave dispersion measurements: Physical modeling. *Journal of Applied Geophysics*, 68(1):95–103.

Boore, D. M. (1972). Finite difference methods for seismic wave propagation in heterogeneous materials. *Methods in computational physics*, 11:1–37.

Bretaudeau, F., Brossier, R., Leparoux, D., Abraham, O., and Virieux, J. (2013). 2d elastic full-waveform imaging of the near-surface: application to synthetic and physical modelling data sets. *Near Surface Geophysics*, 11(3):307–316.

Bretaudeau, F., Leparoux, D., Durand, O., and Abraham, O. (2011). Small-scale modeling of onshore seismic experiment: A tool to validate numerical modeling and seismic imaging methods. *Geophysics*, 76(5):T101–T112.

Buddensiek, M. L., Krawczyk, C. M., Kukowski, N., and Oncken, O. (2009). Performance of piezoelectric transducers in terms of amplitude and waveform. *Geophysics*, 74(2):T33–T45.

Calderón-Macías, C. and Luke, B. (2007). Improved parameterization to invert rayleigh-wave data for shallow profiles containing stiff inclusionsimproved parameterization in inversion. *Geophysics*, 72(1):U1–U10.

Cha, S.-H. and Srihari, S. N. (2002). On measuring the distance between histograms. *Pattern Recognition*, 35(6):1355–1370.

Chen, X. (1993). A systematic and efficient method of computing normal modes for multilayered half-space. *Geophysical Journal International*, 115(2):391–409.

Constable, S. C., Parker, R. L., and Constable, C. G. (1987). Occam's inversion: A practical algorithm for generating smooth models from electromagnetic sounding data. *Geophysics*, 52(3):289–300.

Cotton, J., Chauris, H., Forgues, E., and Hardouin, P. (2018). Time-lapse velocity analysis—application to onshore continuous reservoir monitoring. *Geophysics*, 83(3):B105–B117.

Dangeard, M., Bodet, L., Pasquet, S., Thiesson, J., Guérin, R., Jougnot, D., and Longuevergne, L. (2018). Estimating picking errors in near-surface seismic data to enable their time-lapse interpretation of hydrosystems. *Near Surface Geophysics*, 16(6):613–625.

Denli, H. and Huang, L. (2009). Double-difference elastic waveform tomography in the time domain. In *SEG Technical Program Expanded Abstracts 2009*, pages 2302–2306. Society of Exploration Geophysicists.

Dettmer, J., Molnar, S., Steininger, G., Dosso, S. E., and Cassidy, J. F. (2012). Trans-dimensional inversion of microtremor array dispersion data with hierarchical autoregressive error models. *Geophysical Journal International*, 188(2):719–734.

Duda, R. O., Hart, P. E., et al. (1973). *Pattern classification and scene analysis*, volume 3. Wiley New York.

Dunkin, J. W. (1965). Computation of modal solutions in layered, elastic media at high frequencies. *Bulletin of the Seismological Society of America*, 55(2):335–358.

Dziewonski, A., Bloch, S., and Landisman, M. (1969). A technique for the analysis of transient seismic signals. *Bulletin of the Seismological Society of America*, 59(1):427.

Endrun, B., Meier, T., Lebedev, S., Bohnhoff, M., Stavrakakis, G., and Harjes, H.-P. (2008). S velocity structure and radial anisotropy in the aegean region from surface wave dispersion. *Geophysical Journal International*, 174(2):593–616.

Engquist, B. and Froese, B. D. (2013). Application of the wasserstein metric to seismic signals. *arXiv preprint arXiv:1311.4581*.

Faccioli, E., Maggio, F., Quarteroni, A., and Taghan, A. (1996). Spectral-domain decomposition methods for the solution of acoustic and elastic wave equations. *Geophysics*, 61(4):1160–1174.

Filippi, C., Leparoux, D., Grandjean, G., Bitri, A., and Côte, P. (2019). New robust observables on Rayleigh waves affected by an underground cavity: from numerical to experimental modelling. *Geophysical Journal International*, 218(3):1903–1918.

Foti, S., Hollender, F., Garofalo, F., Albarello, D., Asten, M., Bard, P. Y., Comina, C., Cornou, C., Cox, B., Di Giulio, G., Forbriger, T., Hayashi, K., Lunedei, E., Martin, A., Mercerat, D., Ohrnberger, M., Poggi, V., Renalier, F., Sicilia, D., and Socco, V. (2017). Guidelines for the good practice of surface wave analysis: a product of the InterPACIFIC project. pages 1–54.

Foti, S., Lai, C., Rix, G., and Strobbia, C. (2014). *Surface Wave Methods for Near-Surface Site Characterization*.

Foti, S., Lancellotta, R., Sambuelli, L., and Socco, L. V. (2000). Notes on fk analysis of surface waves. *Annals of Geophysics*, 43.

French, W. S. (1974). Two-dimensional and three-dimensional migration of model-experiment reflection profiles. *Geophysics*, 39(3):265–277.

Fukushima, Y., Nishizawa, O., and Sato, H. (2009). A performance study of a laser doppler vibrometer for measuring waveforms from piezoelectric transducers. *IEEE transactions on ultrasonics, ferroelectrics, and frequency control*, 56(7):1442–1450.

Gabriels, P., Snieder, R., and Nolet, G. (1987). In situ measurements of shear-wave velocity in sediments with higher-mode Rayleigh waves. *Geophysical Prospecting*, 35(2):187–196.

Gallagher, K. and Sambridge, M. (1994). Genetic algorithms: a powerful tool for large-scale nonlinear optimization problems. *Computers & Geosciences*, 20(7-8):1229–1236.

Geman, S. and Geman, D. (1984). Stochastic relaxation, gibbs distributions, and the bayesian restoration of images. *IEEE Transactions on pattern analysis and machine intelligence*, (6):721–741.

Gilbert, F. and Backus, G. E. (1966). Propagator matrices in elastic wave and vibration problems. *Geophysics*, 31(2):326–332.

Haeni, F. (1986). Application of seismic refraction methods in groundwater modeling studies in new england. *Geophysics*, 51(2):236–249.

Haskell, N. A. (1953). The dispersion of surface waves on multilayered media. *Bulletin of the seismological Society of America*, 43(1):17–34.

Hastings, W. K. (1970). Monte carlo sampling methods using markov chains and their applications.

Hilterman, F. J. (1970). Three-dimensional seismic modeling. *Geophysics*, 35(6):1020–1037.

Hisada, Y. (1994). An efficient method for computing green's functions for a layered half-space with sources and receivers at close depths. *Bulletin of the Seismological Society of America*, 84(5):1456–1472.

Hisada, Y. (1995). An efficient method for computing green's functions for a layered half-space with sources and receivers at close depths (part 2). *Bulletin of the Seismological Society of America*, 85(4):1080–1093.

Hobiger, M., Cornou, C., Wathelet, M., Giulio, G. D., Knapmeyer-Endrun, B., Renalier, F., Bard, P.-Y., Savvaidis, A., Hailemikael, S., Le, B. N., et al. (2013). Ground structure imaging by inversions of rayleigh wave ellipticity: sensitivity analysis and application to european strong-motion sites. *Geophysical Journal International*, 192(1):207–229.

Ikeda, T., Tsuji, T., Takanashi, M., Kurosawa, I., Nakatsukasa, M., Kato, A., Worth, K., White, D., and Roberts, B. (2017). Temporal variation of the shallow subsurface at the aquistore co2 storage site associated with environmental influences using a continuous and controlled seismic source. *Journal of Geophysical Research: Solid Earth*, 122(4):2859–2872.

Jain, A. K., Duin, R. P. W., and Mao, J. (2000). Statistical pattern recognition: A review. *IEEE Transactions on pattern analysis and machine intelligence*, 22(1):4–37.

Joubert, A., Le Feuvre, M., and Côte, P. (2018). Passive monitoring of a sea dike during a tidal cycle using sea waves as a seismic noise source. *Geophysical Journal International*, 214(2):1364–1378.

Kailath, T. (1967). The divergence and bhattacharyya distance measures in signal selection. *IEEE transactions on communication technology*, 15(1):52–60.

Kaslilar, A. (2007). Inverse scattering of surface waves: imaging of near-surface heterogeneities. *Geophysical Journal International*, 171(1):352–367.

Kausel, E. (1981). *An explicit solution for the Green functions for dynamic loads in layered media*. Department of Civil Engineering, School of Engineering, Massachusetts ....

Kausel, E. and Roësset, J. M. (1981). Stiffness matrices for layered soils. *Bulletin of the seismological Society of America*, 71(6):1743–1761.

Keilis-Borok, V. I. and Yanovskaja, T. B. (1967). Inverse Problems of Seismology (Structural Review). *Geophysical Journal International*, 13(1-3):223–234.

Kennett, B. (1974). Reflections, rays, and reverberations. *Bulletin of the Seismological Society of America*, 64(6):1685–1696.

Kennett, B. (1983). *Seismic wave propagation in stratified media*. Cambridge U Press, New York.

Kennett, B. and Kerry, N. (1979). Seismic waves in a stratified half space. *Geophysical Journal International*, 57(3):557–583.

Kirkpatrick, S., Gelatt, C. D., and Vecchi, M. P. (1983). Optimization by simulated annealing. *science*, 220(4598):671–680.

Knopoff, L. (1964). A matrix method for elastic wave problems. *Bulletin of the Seismological Society of America*, 54(1):431–438.

Kodera, K., De Villedary, C., and Gendrin, R. (1976). A new method for the numerical analysis of non-stationary signals. *Physics of the Earth and Planetary Interiors*, 12(2-3):142–150.

Kullback, S. and Leibler, R. A. (1951). On information and sufficiency. *The annals of mathematical statistics*, 22(1):79–86.

Lai, C. G., Foti, S., and Rix, G. J. (2005). Propagation of data uncertainty in surface wave inversion. *Journal of Environmental & Engineering Geophysics*, 10(2):219–228.

Lai, C. G. and Rix, G. J. (1998). Simultaneous inversion of rayleigh phase velocity and attenuation for near-surface site characterization.

Le Feuvre, M., Joubert, A., Leparoux, D., and CÔte, P. (2015). Passive multichannel analysis of surface waves with cross-correlations and beamforming. Application to a sea dike. *Journal of Applied Geophysics*, 114:36–51.

Lecocq, T., Longuevergne, L., Pedersen, H. A., Brenguier, F., and Stammler, K. (2017). Monitoring ground water storage at mesoscale using seismic noise: 30 years of continuous observation and thermo-elastic and hydrological modeling. *Scientific reports*, 7(1):1–16.

Leparoux, D., Côte, P., and Gélis, C. (2012). Edz characterization with surface wave analysis: an experimental and numerical study for defining feasibility in the context of the tournemire platform (france). *Near Surface Geophysics*, 10(5):401–411.

Lo, T.-w., Toksöz, M. N., Xu, S.-h., and Wu, R.-S. (1988). Ultrasonic laboratory tests of geophysical tomographic reconstruction. *Geophysics*, 53(7):947–956.

Luco, J. E. and Apsel, R. J. (1983). On the green's functions for a layered halfspace. part i. *Bulletin of the Seismological Society of America*, 73(4):909–929.

Luo, Y., Xia, J., Miller, R. D., Xu, Y., Liu, J., and Liu, Q. (2008). Rayleigh-wave dispersive energy imaging using a high-resolution linear radon transform. *Pure and Applied Geophysics*, 165(5):903–922.

Lysmer, J. and Drake, L. A. (1972). A finite element method for seismology. *Methods in computational physics*, 11:181–216.

Lysmer, J. and Waas, G. (1972). Shear waves in plane infinite structures. *Journal of Engineering Mechanics*.

MacLeod, M., Hanson, R., Bell, C., and McHugo, S. (1999). The alba field ocean bottom cable seismic survey: Impact on development. *The Leading Edge*, 18(11):1306–1312.

Manolis, G. D. and Beskos, D. E. (1988). *Boundary element methods in elastodynamics*. Taylor & Francis.

Maranò, S., Reller, C., Loeliger, H.-A., and Fäh, D. (2012). Seismic waves estimation and wavefield decomposition: application to ambient vibrations. *Geophysical Journal International*, 191(1):175–188.

Maraschini, M., Ernst, F., Foti, S., and Socco, L. V. (2010). A new misfit function for multimodal inversion of surface waves. *Geophysics*, 75(4):G31–G43.

McMechan, G. A. and Yedlin, M. J. (1981). Analysis of Dispersive Waves by Wave-field Transformation. *Geophysics*, 46(6):869–874.

Menke, W. (2018). *Geophysical data analysis: Discrete inverse theory*. Academic press.

Métais, V. (2016). *Auscultation avec les ondes de surface de matériaux très hétérogènes*. PhD thesis, The French Institute of Science and Technology for Transport, Development and Networks.

Métais, V., Chekroun, M., Le Marrec, L., Le Duff, A., Plantier, G., and Abraham, O. (2016). Influence of multiple scattering in heterogeneous concrete on results of the surface wave inverse problem. *NDT & E International*, 79:53–62.

Métivier, L., Brossier, R., Mérigot, Q., Oudet, E., and Virieux, J. (2016). Measuring the misfit between seismograms using an optimal transport distance: Application to full waveform inversion. *Geophysical Supplements to the Monthly Notices of the Royal Astronomical Society*, 205(1):345–377.

Mitchell, B. J. (1995). Anelastic structure and evolution of the continental crust and upper mantle from seismic surface wave attenuation. *Reviews of Geophysics*, 33(4):441–462.

Mokhtar, T. A., Herrmann, R., and Russell, D. (1988). Seismic velocity and q model for the shallow structure of the arabian shield from short-period rayleigh waves. *Geophysics*, 53(11):1379–1387.

Nazarian, S., Stokoe, I., Kenneth, H., and Hudson, W. (1983). *Use of spectral analysis of surface waves method for determination of moduli and thicknesses of pavement systems*. Number 930.

Oliver, J., Press, F., and Ewing, M. (1954). Two-dimensional model seismology. *Geophysics*, 19(2):202–219.

O'Neill, A. (2004). Shear velocity model appraisal in shallow surface wave inversion. In *Symposium on the Application of Geophysics to Engineering and Environmental Problems 2004*, pages 1544–1555. Society of Exploration Geophysicists.

Pageot, D., Leparoux, D., Durand, O., Le Feuvre, M., Côte, P., and Capdeville, Y. (2015). Refined experimental studies for improving the reduced-scale physical modeling of seismic subsurface measurement. In *Near Surface Geoscience 2015-21st European Meeting of Environmental and Engineering Geophysics*.

Pageot, D., Leparoux, D., Le Feuvre, M., Durand, O., Côte, P., and Capdeville, Y. (2017). Improving the seismic small-scale modelling by comparison with numerical methods. *Geophysical Journal International*, 211(1):637–649.

Palmer, D. (1981). An introduction to the generalized reciprocal method of seismic refraction interpretation. *Geophysics*, 46(11):1508–1518.

Park, C. B., Miller, R. D., and Xia, J. (1998). Imaging dispersion curves of surface waves on multi-channel record. In *SEG Technical Program Expanded Abstracts 1998*, pages 1377–1380. Society of Exploration Geophysicists.

Park, C. B., Miller, R. D., and Xia, J. (1999). Multimodal analysis of high frequency surface waves. In *Symposium on the Application of Geophysics to Engineering and Environmental Problems 1999*, pages 115–121. Society of Exploration Geophysicists.

Pasquet, S., Bodet, L., Bergamo, P., Guérin, R., Martin, R., Mourgues, R., and Tournat, V. (2016). Small-scale seismic monitoring of varying water levels in granular media. *Vadose zone journal*, 15(7).

Pasquet, S., Bodet, L., Dhemaied, A., Mouhri, A., Vitale, Q., Rejiba, F., Flipo, N., and Guérin, R. (2015a). Detecting different water table levels in a shallow aquifer with combined p-, surface and sh-wave surveys: Insights from vp/vs or poisson's ratios. *Journal of Applied Geophysics*, 113:38–50.

Pasquet, S., Bodet, L., Longuevergne, L., Dhemaied, A., Camerlynck, C., Rejiba, F., and Guérin, R. (2015b). 2d characterization of near-surface vp/vs: surface-wave dispersion inversion versus refraction tomography. *Near Surface Geophysics*, 13(4):315–332.

Pasquet, S., Sauvin, G., Andriamboavonjy, M., Bodet, L., Lecomte, I., and Guérin, R. (2014). Surface-wave dispersion inversion versus sh-wave refraction tomography in saturated and poorly dispersive quick clays. In *Near Surface Geoscience 2014-20th European Meeting of Environmental and Engineering Geophysics*, volume 2014, pages 1–5. European Association of Geoscientists & Engineers.

Pass, G., Zabih, R., and Miller, J. (1997). Comparing images using color coherence vectors. In *Proceedings of the fourth ACM international conference on Multimedia*, pages 65–73.

Pedersen, H. A., Mars, J. I., and Amblard, P. (2003). Improving surface-wave group velocity measurements by energy reassignement. *Geophysics*, 68(2):677–684.

Pei, D., Louie, J. N., and Pullammanappallil, S. K. (2008). Improvements on computation of phase velocities of rayleigh waves based on the generalized r/t coefficient method. *Bulletin of the Seismological Society of America*, 98(1):280–287.

Pestel, E. and Leckie, F. A. (1963). *Matrix methods in elastomechanics*. McGraw-Hill.

Planès, T., Mooney, M. A., Rittgers, J. B. R., Parekh, M. L., Behm, M., and Snieder, R. (2016). Time-lapse monitoring of internal erosion in earthen dams and levees using ambient seismic noise. *Géotechnique*, 66(4):301–312.

Planès, T., Rittgers, J. B., Mooney, M. A., Kanning, W., and Draganov, D. (2017). Monitoring the tidal response of a sea levee with ambient seismic noise. *Journal of Applied Geophysics*, 138:255–263.

Poggi, V., Fäh, D., Burjanek, J., and Giardini, D. (2012). The use of rayleigh-wave ellipticity for site-specific hazard assessment and microzonation: application to the city of lucerne, switzerland. *Geophysical Journal International*, 188(3):1154–1172.

Pratt, R. G. (1999). Seismic waveform inversion in the frequency domain; part 1, theory and verification in a physical scale model. *Geophysics*, 64(3):888–901.

Press, F., Oliver, J., and Ewing, M. (1954). Seismic model study of refractions from a layer of finite thickness. *Geophysics*, 19(3):388–401.

Qixian, L. and Bungey, J. (1996). Using compression wave ultrasonic transducers to measure the velocity of surface waves and hence determine dynamic modulus of elasticity for concrete. *Construction and building materials*, 10(4):237–242.

Renalier, F., Jongmans, D., Campillo, M., and Bard, P.-Y. (2010). Shear wave velocity imaging of the avignonet landslide (france) using ambient noise cross correlation. *Journal of Geophysical Research: Earth Surface*, 115(F3).

Riahi, N., Bokelmann, G., Sala, P., and Saenger, E. H. (2013). Time-lapse analysis of ambient surface wave anisotropy: A three-component array study above an underground gas storage. *Journal of Geophysical Research: Solid Earth*, 118(10):5339–5351.

Rieber, F. (1936). Visual presentation of elastic wave patterns under various structural conditions. *Geophysics*, 1(2):196–218.

Ryden, N. and Park, C. B. (2006). Fast simulated annealing inversion of surface waves on pavement using phase-velocity spectra. *Geophysics*, 71(4):R49–R58.

Safani, J., O'Neill, A., Matsuoka, T., and Sanada, Y. (2005). Applications of love wave dispersion for improved shear-wave velocity imaging. *Environmental and Engineering Geophysics*, 10(2):135–150.

Sambridge, M. (1999a). Geophysical inversion with a neighbourhood algorithm—i. searching a parameter space. *Geophysical journal international*, 138(2):479–494.

Sambridge, M. (1999b). Geophysical inversion with a neighbourhood algorithm—ii. appraising the ensemble. *Geophysical Journal International*, 138(3):727–746.

Sambridge, M., Bodin, T., Gallagher, K., and Tkalčić, H. (2013). Transdimensional inference in the geosciences. *Philosophical Transactions of the Royal Society A: Mathematical, Physical and Engineering Sciences*, 371(1984):20110547.

Sambridge, M. and Drijkoningen, G. (1992). Genetic algorithms in seismic waveform inversion. *Geophysical Journal International*, 109(2):323–342.

Sambridge, M. and Mosegaard, K. (2002). Monte carlo methods in geophysical inverse problems. *Reviews of Geophysics*, 40(3):3–1.

Saygin, E. and Kennett, B. (2012). Crustal structure of australia from ambient seismic noise tomography. *Journal of Geophysical Research: Solid Earth*, 117(B1).

Schwab, F. (1970). Surface-wave dispersion computations: Knopoff's method. *Bulletin of the Seismological Society of America*, 60(5):1491–1520.

Schwab, F. and Knopoff, L. (1970). Surface-wave dispersion computations. *Bulletin of the Seismological Society of America*, 60(2):321–344.

Schwab, F. and Knopoff, L. (1972). Fast surface wave and free mode computations. In *Methods in Computational Physics: Advances in Research and Applications*, volume 11, pages 87–180. Elsevier.

Sears, T. J., Barton, P. J., and Singh, S. C. (2010). Elastic full waveform inversion of multicomponent ocean-bottom cable seismic data: Application to alba field, uk north sea. *Geophysics*, 75(6):R109–R119.

Shapiro, N. M., Campillo, M., Stehly, L., and Ritzwoller, M. H. (2005). High-resolution surface-wave tomography from ambient seismic noise. *Science*, 307(5715):1615–1618.

Shore, J. E. and Gray, R. M. (1982). Minimum cross-entropy pattern classification and cluster analysis. *IEEE Transactions on Pattern Analysis and Machine Intelligence*, (1):11–17.

Snoke, J. A. and Sambridge, M. (2002). Constraints on the s wave velocity structure in a continental shield from surface wave data: Comparing linearized least squares inversion and the direct search neighbourhood algorithm. *Journal of Geophysical Research: Solid Earth*, 107(B5):ESE–4.

Socco, L. and Strobbia, C. (2004). Surface-wave method for near-surface characterization: a tutorial. *Near Surface Geophysics*, pages 165–185.

Socco, L. V., Boiero, D., Foti, S., and Wisén, R. (2009). Laterally constrained inversion of ground roll from seismic reflection records. *Geophysics*, 74(6):G35–G45.

Socco, L. V., Foti, S., and Boiero, D. (2010). Surface-wave analysis for building near-surface velocity models—established approaches and new perspectives. *Geophysics*, 75(5):75A83–75A102.

Stoffa, P. L. and Sen, M. K. (1991). Nonlinear multiparameter optimization using genetic algorithms: Inversion of plane-wave seismograms. *Geophysics*, 56(11):1794–1810.

Stokoe, K. H., Wright, S., Bay, J., and Roesset, J. (1994). Characterization of geotechical sites by sasw method. *Unknown Journal*, pages 15–25.

Strobbia, C. and Foti, S. (2006). Multi-offset phase analysis of surface wave data (mopa). *Journal of Applied Geophysics*, 59(4):300–313.

Takeuchi, H., Saito, M., and Bolt, B. (1972). Seismic surface waves. *Methods in computational physics*, 11:217–295.

Tarantola, A. (1984). Inversion of seismic reflection data in the acoustic approximation. *Geophysics*, 49(8):1259–1266.

Tarantola, A. (2005). *Inverse problem theory and methods for model parameter estimation*, volume 89. siam.

Thomson, W. T. (1950). Transmission of elastic waves through a stratified solid medium. *Journal of applied Physics*, 21(2):89–93.

Tokimatsu, K., Tamura, S., and Kojima, H. (1992). Effects of multiple modes on rayleigh wave dispersion characteristics. *Journal of geotechnical engineering*, 118(10):1529–1543.

Valensi, R., Leparoux, D., Durand, O., Bretaudeau, F., and Côte, P. (2015). Multicomponent reduced scale seismic modelling: upgrade of the musc laboratory with application to polarization observations. *Geophysical Journal International*, 202(3):1993–2024.

Viktorov, I. (1967). *Rayleigh and Lamb waves: physical theory and applications*. Plenumn Press, New York.

Virieux, J. and Operto, S. (2009). An overview of full-waveform inversion in exploration geophysics. *Geophysics*, 74(6):WCC1–WCC26.

Wallace, D. (1970). Some limitations of seismic refraction methods in geohydrological surveys of deep alluvial basins a. *Groundwater*, 8(6):8–13.

Wang, A., Le Feuvre, M., Leparoux, D., and Abraham, O. (2018). Impact of small shear wave velocity variations on surface wave phase velocity inversion. In *24th European Meeting of Environmental and Engineering Geophysics*.

Wang, A., Leparoux, D., and Abraham, O. (2020a). Differential inversion of surface wave methods: Proposition of diagram distance as inversion data. In *26th European Meeting of Environmental and Engineering Geophysics*.

Wang, A., Leparoux, D., Abraham, O., and Le Feuvre, M. (2019). Evaluation of dispersion diagrams distances based on usual histogram analysis for the surface wave difference inversion. In *1st Conference on Geophysics for Infrastructure Planning, Monitoring and BIM*.

Wang, A., Leparoux, D., Abraham, O., and Le Feuvre, M. (2020b). Frequency derivative of rayleigh wave phase velocity for fundamental mode dispersion inversion: parametric study and experimental application. *Geophysical Journal International*.

Watanabe, T., Shimizu, S., Asakawa, E., and Matsuoka, T. (2004). Differential waveform tomography for time-lapse crosswell seismic data with application to gas hydrate production monitoring. In *SEG Technical Program Expanded Abstracts 2004*, pages 2323–2326. Society of Exploration Geophysicists.

Wathelet (2004). Surface-wave inversion using a direct search algorithm and its application to ambient vibration measurements. *Near Surface Geophysics*, pages 211–221.

Wathelet, M. (2008). An improved neighborhood algorithm: parameter conditions and dynamic scaling. *Geophysical Research Letters*, 35(9).

Watson, T. (1970). A note on fast computation of rayleigh wave dispersion in the multilayered elastic half-space. *Bulletin of the Seismological Society of America*, 60(1):161–166.

Xia, J. (2014). Estimation of near-surface shear-wave velocities and quality factors using multichannel analysis of surface-wave methods. *Journal of applied geophysics*, 103:140–151.

Xia, J., Miller, R. D., and Park, C. B. (1999). Estimation of near-surface shear-wave velocity by inversion of rayleigh waves. *Geophysics*, 64(3):691–700.

Yang, D., Fehler, M., Malcolm, A., Liu, F., and Morton, S. (2013). Double-difference waveform inversion of 4d ocean bottom cable data: Application to valhall, north sea. In *SEG Technical Program Expanded Abstracts 2013*, pages 4966–4970. Society of Exploration Geophysicists.

Yang, D., Meadows, M., Inderwiesen, P., Landa, J., Malcolm, A., and Fehler, M. (2015). Double-difference waveform inversion: Feasibility and robustness study with pressure data. *Geophysics*, 80(6):M129–M141.

Yilmaz, O. (1987). Seismic data processing. *Investigations in geophysics*.

Yuan, H. and Bodin, T. (2018). A probabilistic shear wave velocity model of the crust in the central west australian craton constrained by transdimensional inversion of ambient noise dispersion. *Tectonics*, 37(7):1994–2012.

Zhang, F., Juhlin, C., Niemi, A., Huang, F., and Bensabat, J. (2016). A feasibility and efficiency study of seismic waveform inversion for time-lapse monitoring of onshore co2 geological storage sites using reflection seismic acquisition geometries. *International Journal of Greenhouse Gas Control*, 48:134–141.

Zhang, S. X. and Chan, L. S. (2003). Possible effects of misidentified mode number on rayleigh wave inversion. *Journal of Applied Geophysics*, 53(1):17–29.

Zhang, Z. and Huang, L. (2013). Double-difference elastic-waveform inversion with prior information for time-lapse monitoring. *Geophysics*, 78(6):R259–R273.

Zheng, Y., Barton, P., Singh, S., et al. (2011). Strategies for elastic full waveform inversion of time-lapse ocean bottom cable (obc) seismic data. In *2011 SEG Annual Meeting*. Society of Exploration Geophysicists.

# Appendices

# Appendix A

# Experimental set-up and measured data of epoxy-resin models

Four reduced-scale models made of epoxy-resin were designed and named $C0$, $C25$, $C45$ and $C65$ respectively (see **Fig. A.1 (a)** for $C0$ and $C65$). They are measured in the MUSC laboratory and the measured data are used for the tests of different approaches proposed in this thesis work.

The experimental set-up consists of a piezo-electric transducer (**Fig. A.1 (b)**) as a point source and a laser interferometer to measure the wave propagation (**Fig. A.1 (c)**). For the experimental tests, the piezo-electric source is fixed on the horizontal harm visible in **Fig. A.1 (c)** below the laser interferometer. **Fig. A.1 (d)** provides information on the positions of the source and the receivers, with the dimensions of the resin models.

The four models ($C0$, $C25$, $C45$ and $C65$) are similar in shape with shear-wave velocity of the deep layer increasing successively. The model parameters of the $C0$ model are available in **Table A.1**. The models consist of two superimposed plates. The pink upper part is machined in a layer of industrial epoxy resin (polyurethane). The lower part is molded underneath this plate from an epoxy resin mixture (casting polyurethane) with an additional filler (hydrated alumina) which gives it specific Vs velocity properties. The choice of the amount of filler included in the polymerized mixture was decided on the basis of information provided in previous experimental studies (Filippi et al., 2019; Pageot et al., 2015; Métais, 2016). The filled resins finally used in this study were also tested by independent measurements.

Table A.1: $C0$ model parameters and dimensions. $h_i$: layer thickness; $l$ and $w$: length and width of model. Scale ratio between the numerical and the experimental model dimensions is 1000.

| layer | $V_{p_i}$ $[m/s]$ | $V_{s_i}$ $[m/s]$ | $\rho_i$ $[kg/m^3]$ | $\nu_i$ | $h_i$ $[mm]$ | l $[mm]$ | w $[mm]$ |
|---|---|---|---|---|---|---|---|
| 1 | 1300 | 703 | 450 | 0.29 | 8.0 | 265 | 235 |
| 2 | 2048 | 933 | 1300 | 0.37 | 203 | 265 | 235 |

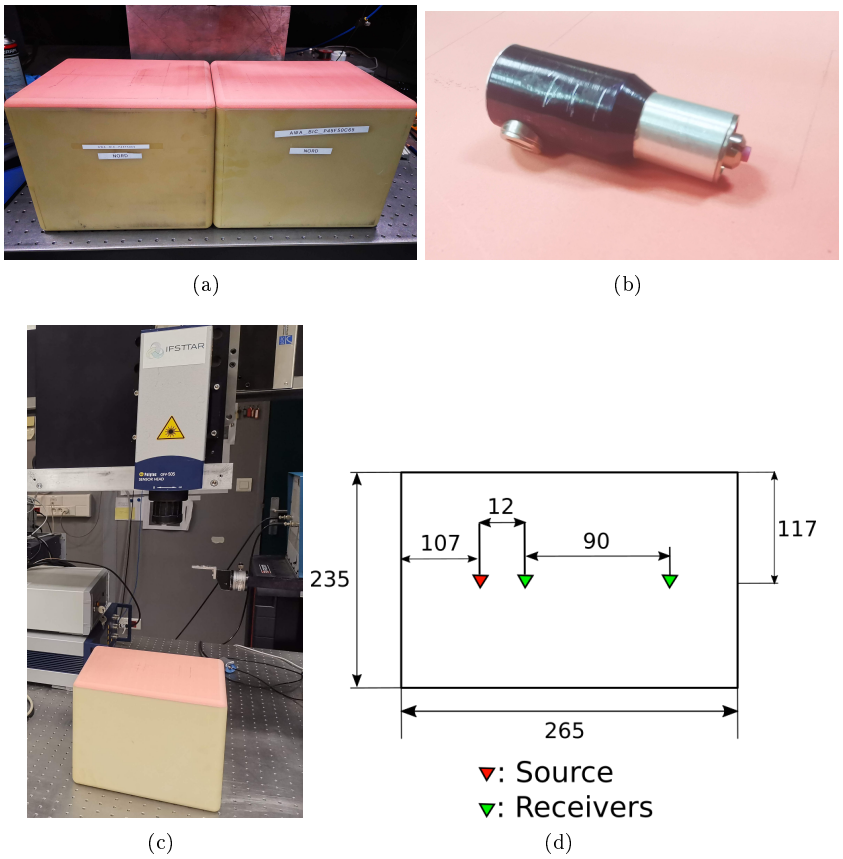


Figure A.1: (a) The baseline (left) and repeatline (right) models. (b) The piezoelectric source Acsys®. (c) Experimental set-up and the two-layer resin model. (d) Position of source and the receiver vector.

The shear-wave velocities of $C25$, $C45$ and $C65$ are respectively $990\,m/s$, $1038\,m/s$ and $1086\,m/s$. **Fig. A.2** presents the measured seismograms of the epoxy-resin models. They are superimposed to make comparisons between models. **Fig. A.3** gives the Rayleigh wave phase velocity dispersion diagrams of the four epoxy-resin models. Dispersion curves are presented together in **Fig. A.4** where the differences are observed in low frequencies, which corresponds to the shear-wave velocity variations in the deep layer.

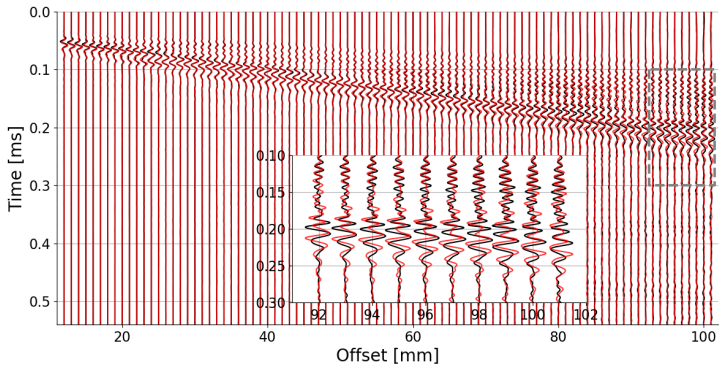


(a)

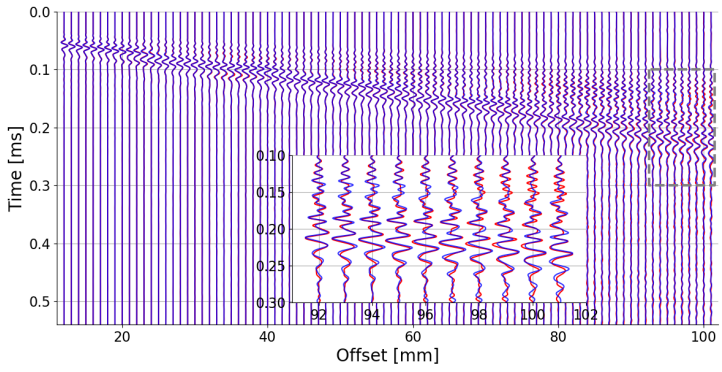


(b)

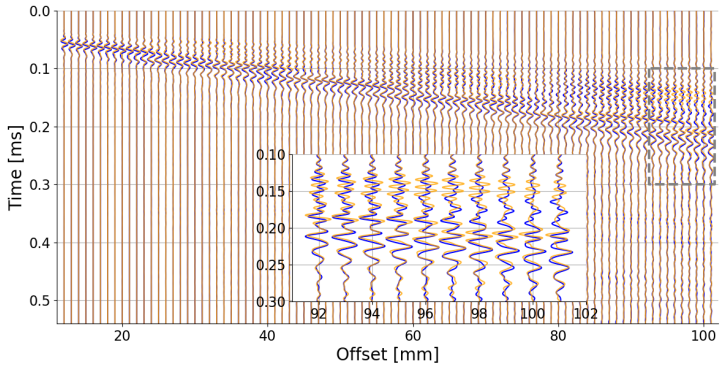


(c)

Figure A.2: Measured seismograms for the epoxy-resin models. Black: $C0$; red: $C25$; blue: $C45$; orange: $C65$. Signals in the grey rectangles are zoomed for a better visualization.

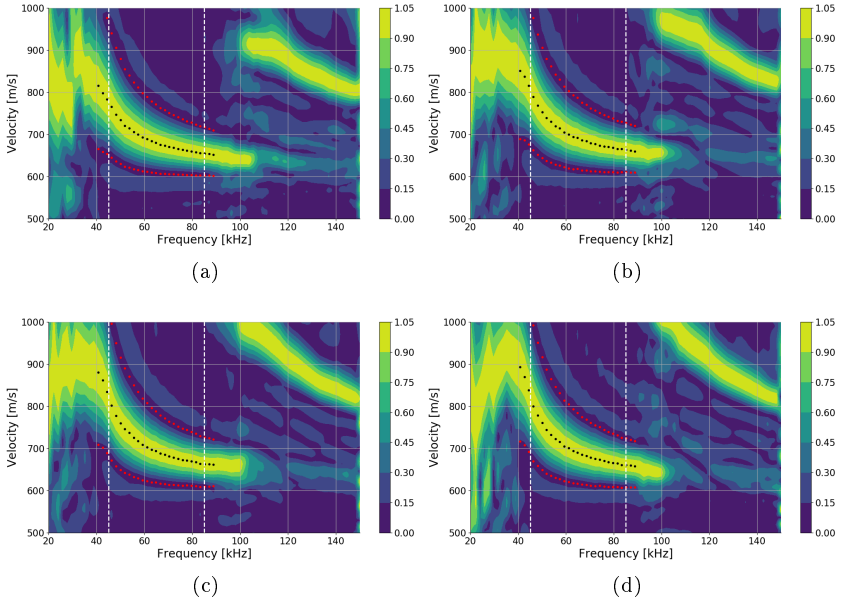


Figure A.3: Dispersion diagrams for the epoxy-resin model (a) $C0$, (b) $C25$, (c) $C45$ and (d) $C65$. Black dots: phase velocity dispersion curves.

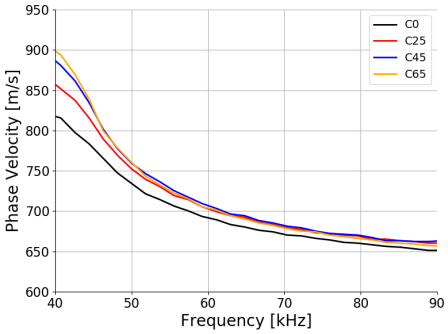


Figure A.4: Dispersion curves of epoxy-resin models.

# Appendix B

# Experimental set-up and measured dispersion curves of mortar-concrete slabs

Three mortar-concrete slabs ($D01$, $D06$ and $D08$), made by a layer of mortar superimposed on the surface of a concrete slab, are measured in laboratory (**Fig. B.1**). The measured data of mortar-concrete slabs are used in Chapter 4 for the validation of Differential Time-Lapse Surface Wave Inversion in heterogeneous medium.

The mortar layers of the three slabs have different water-to-cement ratio (w/c) which changes the mechanical properties of each slab. The parameters and the dimensions of slabs are given in **Table B.1**.

The experimental set-up is made by an ultrasonic source and a receiver probe of 16 receivers. For the measurement of each slab, four sources (54 kHz, 100 kHz, ACS1 and ACS234 in **Fig. B.2**) are used separately in order to average the response of the sensors and improve the signal-to-noise ratio. The sampling rate is equal to $5\,MHz$. For each measurements, the probe is reinstalled five times in a row to have 80 traces in total.

For each slab, four dispersion diagrams are obtained corresponding to four sources used in the measurement. **Fig. B.3** shows the measured dispersion curves of slabs. The final dispersion diagram and the dispersion curve of each slab are obtained after averaging the measured diagrams using the four sources. The dispersion diagrams are picked manually at certain frequencies due to the lack of energy of the source. The final dispersion diagrams and dispersion curves are presented in **Fig. B.4**.

Table B.1: The parameters and dimensions of mortar-concrete slabs $D01$, $D06$ and $D08$. w/c is the water-to-cement ratio of the mortar layer. $h$, $l$, and $w$ are the thickness, the length and the width of the layers and slabs.

The parameters and dimensions of the slab $D01$.

| layer | w/c | $V_p$ $[m/s]$ | $\rho$ $[kg/m^3]$ | $h$ $[m]$ | $l$ $[m]$ | $w$ $[m]$ |
|---|---|---|---|---|---|---|
| mortar | 0.40 | 3660 | 2100 | 0.03 | 1.2 | 0.8 |
| concrete | - | 4300 | 2400 | 0.2 | 1.2 | 0.8 |

The parameters and dimensions of the slab $D06$.

| layer | w/c | $V_p$ $[m/s]$ | $\rho$ $[kg/m^3]$ | $h$ $[m]$ | $l$ $[m]$ | $w$ $[m]$ |
|---|---|---|---|---|---|---|
| mortar | 0.55 | 3150 | 2000 | 0.03 | 1.2 | 0.8 |
| concrete | - | 4300 | 2400 | 0.2 | 1.2 | 0.8 |

The parameters and dimensions of the slab $D08$.

| layer | w/c | $V_p$ $[m/s]$ | $\rho$ $[kg/m^3]$ | $h$ $[m]$ | $l$ $[m]$ | $w$ $[m]$ |
|---|---|---|---|---|---|---|
| mortar | 0.70 | 2642 | 1870 | 0.03 | 1.2 | 0.8 |
| concrete | - | 4300 | 2400 | 0.2 | 1.2 | 0.8 |

(a) (b) (c)

Figure B.1: (a) The measurement set-up. (b) The surface of the concrete slab. (c) The surface of the mortar layer.


(a) (b) (c)

Figure B.2: (a) Source $54\,kHz$. (b) Source $100\,kHz$. (c) Sources $ASC1$ and $ASC234$.

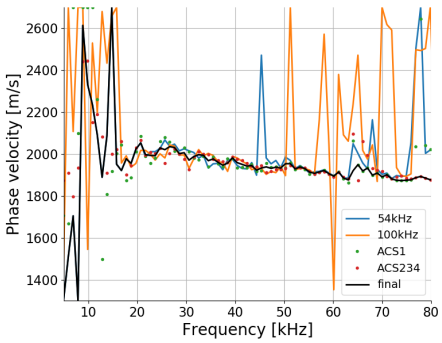


(a)

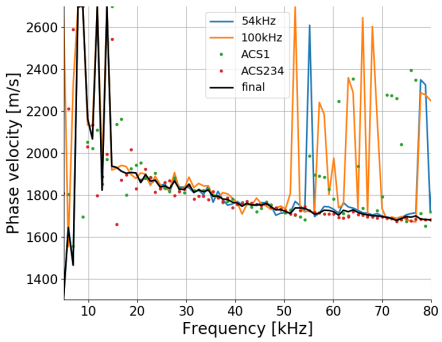


(b)

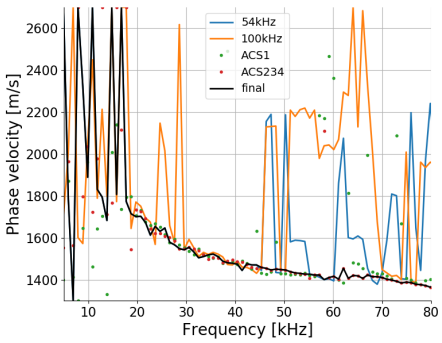


(c)

Figure B.3: Measured dispersion curves of slab (a) $D01$ , (b) $D06$ and (c) $D08$, using the four sources. The black lines are the final dispersion curves after manual picking.

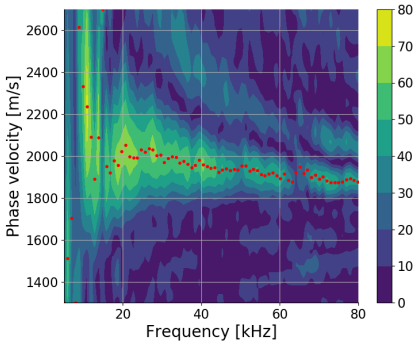


(a)

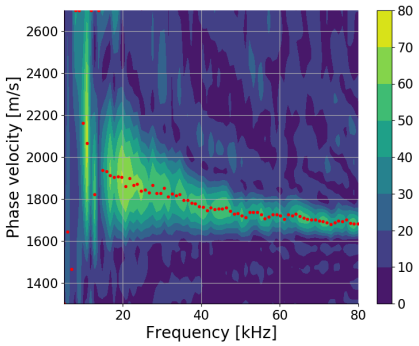


(b)

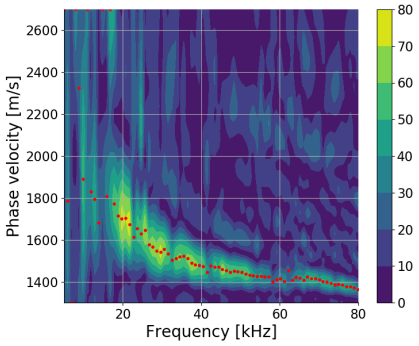


(c)

Figure B.4: The dispersion diagrams of slab D01 (a), D06 (b) and D08(c). The red dots present the dispersion curve of each slab.

# Appendix C

# Ordinal type diagram distance

This part of appendix is a supplement to Chapter 4, in order to describe in detail the use of ordinal type histogram distance for the measure of the dispersion diagram distance in Differential Time-Lapse Surface Wave Inversion. The reason of removing the absolute value of the cumulative summation in the original ordinal type histogram distance definition has also been illustrated.

Three models (a, B and B') are used to generate synthetic data. The parameters of model A are given in **Table C.1**. The models B and B' are similar to the model A of which the shear-wave velocities are different: $V_{s_2}(B) = 1052\,m/s$, $V_{s_2}(B') = 925\,m/s$. The phase velocities of the three models are presented in **Fig. C.1**.

The signals are generated using the experimental set-up of the epoxy-resin models in Appendix A. After signal processing, the velocity distribution of the three models at $f = 40\,kHz$ are presented in **Fig. C.2 (a)**. Since we use the principal lobe as the comparison zone to calculate the diagram distance, only the principal lobes are presented in **Fig. C.2 (a)** and the lateral lobes are reinitialized to zero:

$$Amp(v) = \begin{cases} Amp(v) & if\ v \in [v_{+1}, v_{-1}]\,, \\ 0 & otherwise. \end{cases} \tag{C.1}$$

$Amp(v)$ is the amplitude of the dispersion diagram at one given frequency, as function of velocity; $v_{min}$ and $v_{max}$ are the limits of the principal lobes calculated by **Eq. 4.19**. In **Fig. C.2 (a)**, the difference between the three lobes is the position and the shape of the lobes seems identical.

Since we introduce the histogram distance into the diagram distance calculation, the velocity distribution should be used instead of the amplitude. **Fig.**

Table C.1: Parameters of the model A.

| layer | $V_{p_i}$ $[m/s]$ | $V_{s_i}$ $[m/s]$ | $\rho_i$ $[kg/m^3]$ | $\nu_i$ | $h_i$ $[mm]$ |
|---|---|---|---|---|---|
| 1 | 1300 | 703 | 450 | 0.29 | 7.2 |
| 2 | 2048 | 989 | 1300 | 0.37 | $\infty$ |

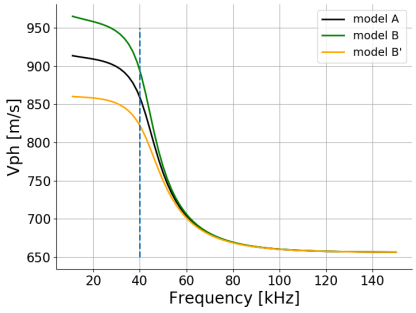


Figure C.1: Phase velocities of model A, B and B'.

**C.2 (b)** gives the velocity distributions of the three models, which is the amplitude in the **Fig. C.2 (a)** normalized by the surface of the principal lobe:

$$P(v) = \frac{Amp(v)}{\sum_v (Amp(v))}. \tag{C.2}$$

In **Fig. C.2 (b)**, the surface of each lobe equals to 1. Compared to **Fig. C.2 (a)**, the differences between lobes are amplified. The shapes of the lobes are different after the normalization since the lobes' widths are $B > A > B'$, according to **Eq. 4.19**.

According to **Eq.4.9** and **Eq. 4.25**, we define two equations which calculate the cumulative summation of the difference between two velocity distributions:

$$Diff_1(v)^{A,B} = \mid \sum_{j=0}^{i} (P(v_j)_A - P(v_j)_B) \mid, \tag{C.3}$$

$$Diff_2(v)^{A,B} = \sum_{j=0}^{i} (P(v_j)_A - P(v_j)_B). \tag{C.4}$$

The cumulative summations with and without the absolute value are presented in **Fig. C.2 (c)** and **Fig. C.2 (d)**. One can see that the sign of the cumulative summation in **Fig. C.2 (d)** indicates the relative position between two velocity distributions: when $Diff_2(v)^{A,B} > 0$ (green curve), $P(v)_B$ is on the right of the $P(v)_A$; when $Diff_2(v)^{A,B'} > 0$ (orange curve), $P(v)_{B'}$ is on the left of the $P(v)_A$. However, this property cannot be observed in **Fig. C.2 (c)**.

Besides, using **Eq. 4.9** and **Eq. 4.25** to calculate the histogram distance of $P(v)_A$ and $P(v)_B$, $P(v)_A$ and $P(v)'_B$, one gets $D_{ord}(A, B) = 36.2$, $D_{ord}(A, B') = 37.9$ and $D'_{ord}(A, B) = 36.2$, $D'_{ord}(A, B') = -37.9$. The sign is also significant when calculating the diagram distance which can avoid the trap of the local minimum, e.g. inversion finds the model B' instead of the true model B.

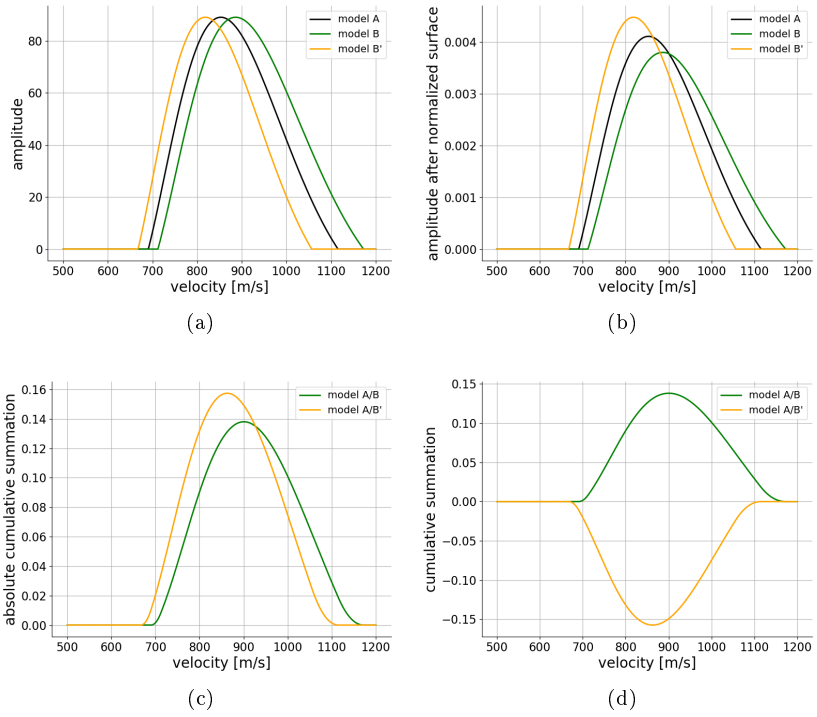


Figure C.2: (a) $Amp(v)_A$, $Amp(v)_B$, $Amp(v)_{B'}$: Amplitude of the dispersion diagram at frequency $f = 40\,kHz$. Only the principal lobe is presented. (b) $P(v)_A$, $P(v)_B$, $P(v)_{B'}$: Velocity distribution (amplitude normalized by the principal lobe surface) of the three lobes. (c) $Diff_1(v)^{A,B}$, $Diff_1(v)^{A,B'}$: Absolute cumulative summation of the difference between model A/B and model A/B'. (d) $Diff_2(v)^{A,B}$, $Diff_2(v)^{A,B'}$: Cumulative summation of the difference between model A/B and model A/B'.

# Appendix D

# Rayleigh Wave Displacement and Cumulative Energy

Rayleigh wave displacement vectors for horizontal and vertical components have been presented in Chapter 2.1.2. Here we use the same equations to calculate the displacement vector of Rayleigh wave, based on a two-layer model (**Table D.1**), for an supplementary illustration of the frequency derivative of Rayleigh wave phase velocity presented in Chapter 3.3.1.

**Fig D.1 (a)** presents the total displacement vector $d(\lambda, z)$ (square root of the horizontal and vertical displacements), as a function of the normalized wavelength ($\lambda/h_1$) and depth ($z/h_1$). **Fig D.1 (b)** presents the cumulative amplitude $D(\lambda, z)$, with its definition

$$D(\lambda, z) = \int_0^z d(\lambda, z)dz. \tag{D.1}$$

Table D.1: Parameters of a two-layer reference model. $V_p$: compressional-wave velocity; $V_s$: shear-wave velocity; $\rho$: density; $\nu$: Poisson's ratio; and $h$: layer thickness.

| layer ($i$) | $V_{p_i}^{ref}$ $[m/s]$ | $V_{s_i}^{ref}$ $[m/s]$ | $\rho_i^{ref}$ $[kg/m^3]$ | $\nu_i^{ref}$ | $h_i^{ref}$ $[m]$ |
|---|---|---|---|---|---|
| 1 | 1000 | 600 | 1500 | 0.22 | 8 |
| 2 | 2000 | 1100 | 2200 | 0.28 | $\infty$ |

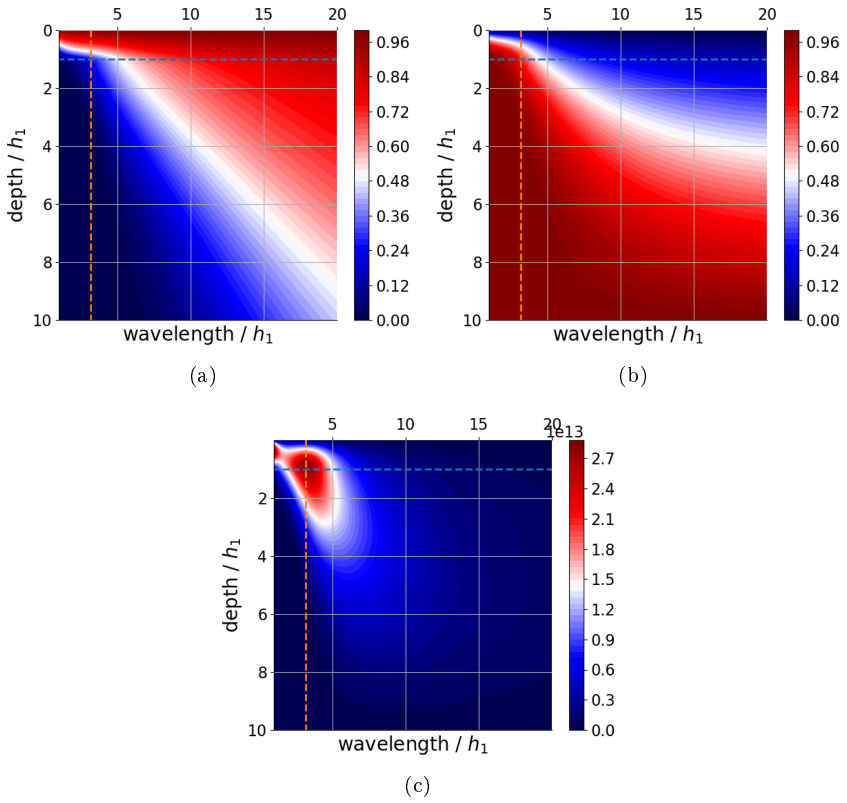


Figure D.1: (a) Rayleigh wave displacement vectors as a function of the normalized depth and wavelength. (b) Cumulative amplitude of the Rayleigh wave displacement in the vertical direction (i.e. depth), normalized by the maximum value at each wavelength. (c) Cumulative amplitude derivative with respect to wavelength. The blue line indicates the interface where $depth/h_1 = 1$. The orange dashed line corresponds to the wavelength $\lambda = 3.2h_1$.

DOCTORAT ECOLOGIE
BRETAGNE GEOSCIENCES
LOIRE AGRONOMIE ALIMENTATION

UNIVERSITÉ DE NANTES

**Titre :** Imagerie différentielle en ondes sismiques de surface et ultrasonores pour le monitoring de structures anthropiques et du proche sous-sol environnant

**Mots clés :** Ondes sismiques de surface, Problème inverse, Optimisation globale, Inversion différentielle, Expérimentation de laboratoire

**Résumé :** Les 1ers mètres du sous-sol, la Zone Critique, concentrent de nombreuses activités humaines. La ZC est aussi le siège de perturbations en raison du changement climatique à travers des variations du niveau des nappes, de modifications hydriques et mécaniques qui augmentent l'érosion et les risques de dommages voire d'effondrements. Aussi, la surveillance de la subsurface et de ses structures anthropiques est actuellement un enjeu majeur.
De ce fait, les méthodes géophysiques, notamment sismiques permettant d'évaluer les paramètres mécaniques du milieu sont intéressantes. Parmi elles, la technique MASW basée sur les Ondes Sismiques de Surface estime un profil 1D de vitesses d'ondes S. La donnée inversée correspond à la dispersion de la vitesse de phase ($V_{ph}$) ou de groupe. Cependant, la précision des solutions inverses par MASW ne discrimine pas les variations de $V_s$ de quelques pourcents. Ces limites sont dues au niveau d'incertitude des mesures mais aussi à la sensibilité de la donnée aux paramètres du milieu.
Pour lever ce verrou, nous proposons 3 alternatives méthodologiques. La première propose d'inverser la dérivée fréquentielle de $V_{ph}$. Les 2 autres reposent sur l'inversion de données différentielles. Dans la première, il s'agit de la distance statistique entre les lobes principaux des diagrammes de dispersion assimilés à des histogrammes. Dans la deuxième, il s'agit de formulation analytique par approximation linéaire de $V_{ph}$. Ces propositions sont appliquées à des modèles bicouches, tant sur des données synthétiques que sur des mesures de laboratoire sur du béton et par interférométrie laser sur des modèles en résines.

**Title :** Seismic and ultrasonic surface wave differential imaging for monitoring anthropogenic structures and the surrounding subsurface

**Keywords :** Seismic surface waves, Global inversion and optimization, Differential inversion, Experiment in laboratory

**Abstract :** The 1st meters of the underground media, the Critical Zone, involve many human activities. It is also the site of disturbances due to climate change through variations in the level of the water table, hydric and mechanical modifications that increase erosion and the risks of damage or even collapse. Therefore, monitoring of the subsurface and its anthropogenic structures is currently a major challenge.
Therefore, geophysical methods, especially seismic methods, which allow to evaluate the mechanical parameters of the environment, are interesting. Among them, the MASW technique based on Surface Seismic Waves estimates a 1D-profile of S wave velocities. The inverted data corresponds to the dispersion of the phase velocity ($V_{ph}$) or group velocity. However, the accuracy of the MASW inverse solutions does not discriminate Vs variations lower than a few percent. These limits are due to the current level of measurements uncertainty but also to the sensitivity of the data to the medium parameters.
To overcome this key issue, we propose 3 methodological alternatives. The first proposes to invert the frequency derivative of $V_{ph}$. The 2 others are based on the inversion of differential data. In the first one, it is the statistical distance between the main lobes of dispersion diagrams assimilated to histograms. In the second, it is an analytical formulation by linear approximation of $V_{ph}$. These proposals show a contribution of the resolution for typical two-layer models of the subsurface, based on synthetic data and laboratory measurements by laser interferometry on resin and concrete models.